Development of perovskite-type electrode materials for solid oxide fuel cells

XIAOKAITI PAIRUZHA

Graduate School of Science and Technology

Hirosaki University

2020

ABSTRACT

A solid oxide fuel cell (SOFC) is a promising energy device that can produce electricity by converting of chemical energy directly with high efficiency. However, its high operating temperature (usually>1000 ^{o}C) is the main barrier in this technology since high temperature will lead to a slow start-up/shut-down procedure, poor thermal stability, poor fuel cell durability, as well as high material cost. Decreasing the operating temperature down to the temperature range of 900- 750 ^{o}C is an effectively solution to these problems, but it makes the oxygen reduction kinetics in the electrolyte and electrodes weaken. Therefore, maintaining the oxygen reduction kinetics at lower temperatures is one of the main challenges in this field. Meanwhile, the hydrocarbon fuels are easily cracked on the anode, resulting in carbon deposition, which will decrease the activity, and finally reducing the cell performance. Thus, development of coking-resistance electrode materials with high electroactivity is also important for the SOFCs. In this dissertation, Fe-Co-based perovskite oxides with high activity as well as stability were developed as the electrodes for the SOFCs. The effects of various doping elements at different position on the ABO_3 unit perovskite on the performance of oxygen reduction reaction (ORR) were investigated. Moreover, in order to solve the possible coke formation and/or sulfur poisoning on the surface of the anode, these perovskite oxides

were used as the symmetrical electrode materials to fabricate symmetrical SOFCs (SSOFCs), in which the same material is used as both anode and cathode so that the deactivated anode can be regenerated by sequentially using the anode as a cathode. It includes 6 Chapters.

Firstly, by doping larger-radius element of niobium (Nb) at B-site, perovskite materials of $Pr_{0.4}Sr_{0.6}(Co_{0.3}Fe_{0.6})_{1-x}Nb_xO_{3-\delta}$ ($PSCFN_x$, x=0, 0.05, 0.1 and 0.2) were firstly synthesized as the cathode materials for solid oxide fuel cells (SOFCs) using a solid state reaction method. The effect of Nb doping amount on the lattice structure, oxygen desorption and electrochemical properties of PSCFNx at different calcination temperatures were investigated. It is found that this material family had a perfectly cubic structure based on the Pm-3m space group whose lattice size increased with x, and found that the materials were thermally stable after calcination and showed desirable chemical compatibility with the $La_{0.8}Sr_{0.2}Ga_{0.8}Mg_{0.2}O_{3-\delta}$ electrolyte in the condition of calcination at 1250 °C for 8 h under an air atmosphere. The optimum x value of 0.1 was found for the PSCFNx cathode materials, which had the minimum polarization resistance value of 0.018 Ωcm^2 at 900 °C. As a result, the single cell with the $PSCFN_{0.1}$ cathode delivered a power density of 0.731 Wcm^{-2} at 900°C with the humidified H_2 (~3% H_2O) as the fuel and ambient air as the oxidant, which indicates that $PSCFN_{0.1}$ should be a promising

cathode material for the SOFCs.

Secondly, $Sr_{0.9}Co_{0.3}Fe_{0.7}O_{3+\delta}$ was doped by cerium via the solid state reaction method to enhance the electrochemical activity. The obtained novel cathode materials $(Ce_{0.1}Sr_{0.9})_xCo_{0.3}Fe_{0.7}O_{3-\delta}$ ($(CS)_xCF$) were confirmed to have a Pm-3m cubic perovskite structure when x was in the range of 0.90-1.10 based on X-ray diffraction (XRD) analysis. A-site deficiency was generated as $x<1.0$ but A-site excess($x>1.0$) resulted in impurity phases. The generation of A-site deficiency was confirmed based on X-ray photoelectron (XPS) and O_2-TPD measurements. As a result, the SOFCs with $(CS)_{0.9}CF$ cathode showed the maximum power density of 0.571 Wcm^{-2} at 800 ^oC and the maximum conductivity of 109.6 Scm^{-1} at 500 ^oC.

Thirdly, $Pr_{0.4}Sr_{0.6}Co_{0.9-x}Fe_xNb_{0.1}O_{3-\delta}$ ($PSCF_xN$) (x=0, 0.2, 0.4, 0.6 and 0.9) oxides were evaluated as the symmetric electrode materials for SOFCs. Effects of stoichiometric amounts of iron (Fe) and cobalt (Co) on electrical conductivity, thermal expansion and electrochemical properties were investigated. Both the thermal expansion coefficient (TEC) and conductivity decreased with the increase in Fe amount. With higher Fe content, more Fe^{4+} species were reduced to Fe^{3+}, generating more oxygen vacancies. This effectively promoted the oxygen incorporation kinetics, and lowered the polarization resistance (Rp). As a result, the $PSCF_{0.6}N$ exhibited the lowest polarization resistance of

0.028 Ω cm^2 at 900 ºC and the highest electrical conductivity of 258.90 Scm^{-1} at 650 ºC among all the prepared $PSCF_xN$ materials. Meanwhile, with the doping of Fe, the TEC decreased near to the electrolyte`s TEC value, and the TECs of PSCN, $PSCF_{0.6}N$ and LSGM (electrolyte) were 17.39, 11.79 and 10.01 $\times 10^{-6}$, respectively, in air. As such, the peak power densities of the electrolyte supported symmetric SOFCs with different electrolyte thicknesses of 500, 400 and 300 μm were 0.642, 0.713 and 0.891 Wcm^{-2}, respectively, indicating that the $PSCF_{0.6}N$ material should be a promising electrode material for the symmetric SOFCs.

ACKNOWLEDGMENTS

First of all, I would like to express my sincere gratitude and appreciation to my supervisor, Professor Dr. Abuliti Abudula for giving me an opportunity to work towards Ph.D in his laboratory and for his helpful suggestions academically, professionally, and personally to go forward during my Ph.D program.

I would like to thanks Professor Dr. Guoqing Guan, Laboratory of Energy Conversion Engineering, Institute of Regional Innovation (IRI), Hirosaki University, for his kind advices, good suggestions and supports of my study.

I would like to thank Associate Professor Dr. Akihiro Yoshida in our group for his kind suggestions and helpful discussion on my research.

I would like to thank Dr. Xiaogang Hao, Department of Chemical Engineering, Tianyuan University of Technology, China, for his helps regarding to the fundamental and application of X-ray photoelectron spectroscopy.

I would like to thank all members in our group for their helps and supports to my research.

I would like to thank my dear family for all their support. My father and mother have supported me in every step along my journey, and I would not be where I am today without them. Words cannot express my gratitude. At the same time, thank my younger brother, who accompanies my parents in the days when I am away.

Finally, I would like to acknowledge the scholarship from Kyoritsu International Foundation.

Thank you all.

XIAOKAITI PAIRUZHA

TABLE OF CONTENTS

LIST OF TABLES

LIST OF FIGURES

Chapter 1 Introduction

1.1 General Introduction

The increasing greenhouse gas effect and environmental pollution derived from excessive fossil fuels utilization and the threat of a gradual decline in fossil fuels resources have promoted us to develop find new energy resources and develop novel energy materials and technologies to build a sustainable infrastructure. Among them, fuel cells (FCs) should be one of the best choices. FC is a devices which can directly convert chemical energy of a fuel into electricity via electrochemical reaction. It has two electrodes, i.e., the anode and cathode. The reactions taken place at the electrodes produce electricity. The other important part of the FC is the electrolyte, which carries electrically charged species from one electrode to the other one, and accelerates the reactions at the electrodes.

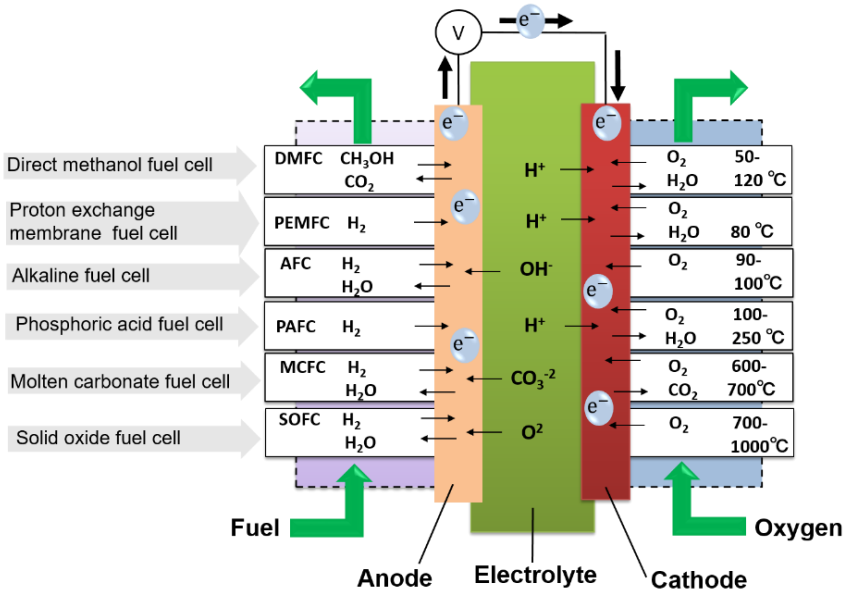

Figure 1.1 Various types of fuel cells

Table 1.1 Technical characteristics of six different types of fuel cells

Fuel cells	Common electrolyte	Fuel	Applications	Advantages	Disadvantage	Efficiency	Anode reaction	Cathode reaction
DMFC	Polymer electrolyte	methanol	vehicles	Lower operating temperatures, does not need a large, heavy heat shield.	carbon dioxide as a by-product will be released into the atmosphere	10%	$CH_3OH + H_2O \rightarrow CO_2 + 6H^+ + 6e^-$	$\frac{3}{2}O_2 + 6H^+ + 6e^- \rightarrow 3H_2O$
PEMFC	Polymer proton exchange membrane	Less pure hydrogen from hydrocarbons or methanol	Backup power, Portable power, Transportation, Specialty vehicles	Solid electrolyte reduces corrosion and electrolyte management problems; Low temperature; quick start-up.	Expansive catalysis; sensitive to fuel impurities; low temperature waste heat.	35-60%	$H_2 \rightarrow 2H^+ + 2e^-$	$O_2 + 4H^+ + 4e^- \rightarrow 2H_2O$
AFC	Potassium hydroxide	Pure hydrogen, hydrazine	military	Cathode reaction faster in alkaline electrolyte; leads to high performance, low cost components	Sensitive to CO2 in fuel and air; electrolyte management	60%	$H_2 + 2OH^- \rightarrow 2H_2O + 2e^-$	$O_2 + 2H_2O + 4e^- \rightarrow 4OH^-$
PAFC	Phosphoric acid	Hydrogen from hydrocarbons and alcohol	distributed generation	Higher temperature enables CHP; increased tolerance to fuel impurities	Pt catalyst; long start up time; low current and power.	40%	$H_2 \rightarrow 2H^+ + 2e^-$	$O_2 + 4H^+ + 4e^- \rightarrow 2H_2O$
MCFC	Molten salt	Hydrogen, carbon monoxide	Electric utility, distributed generation	High efficiency; fuel flexibility; can use a variety of catalysts; suitable for CHP	High temperature corrosion and breakdown of cell components; long start up time; low power density	45-50%	$H_2 + CO_3^{2-} \rightarrow H_2O + CO_2 + 2e^-$ $CO + CO_3^{2-} \rightarrow 2CO_2 + 2e^-$	$O_2 + 2CO_2 + 4e^- \rightarrow 2CO_3^{2-}$
SOFC	Yttria stabilized zirconia	Natural gas or propane	Auxiliary power, electric utility, distributed generation	High efficiency; fuel flexibility; can use a variety of catalysts; solid electrolyte; suitable for CHP and CHHP; hybrid/GT cycle	High temperature corrosion and breakdown of cell components; High temperature operation requires long start up time and limits.	60%	$H_2 + O^{2-} \rightarrow H_2O + 2e^-$ $CO+O^{2-} \rightarrow CO_2 + 2e^-$	$O_2 + 4e^- \rightarrow 2O^{2-}$

FCs have six main types, i.e., direct methanol fuel cells (DMFCs), proton exchange membrane fuel cells (PEMFCs), alkaline fuel cells (AFCs), phosphoric acid fuel cells (PAFCs), molten carbonate fuel cell (MCFCs) and solid oxide fuel cells (SOFCs). These six major FCs are operated by different half-cell reactions depending upon the characteristics of the electrolyte. The principal half-cell reactions operated in each FC and the technical characteristics of different FCs are given in Table 1.1.

Here we focus on the SOFC, which is most widely used as an alternative energy sources and power generating equipment, which is expected to produce highly efficient energy with hydrocarbon and even original fossil fuels. Application of SOFC can produce electricity with low pollution and high efficiency of approximately 60% by the environment friendly energy-conversion method [1].

A typical SOFC also includes three parts: electrolyte, cathode and anode. The porous cathode and anode are separated by a dense solid electrolyte. The fuel and oxidant gas flow into the anode and cathode, respectively, but the electrolyte is a barrier to gas diffusion, and instead, it allows oxide-ion or proton transportation in it.

As shown in Figure. 1.2, for the proton conductor electrolyte, the protons are produced at the anode side, then diffuse through the solid electrolyte, arrive at the electrochemical active area of the cathode, and react with oxide ions to produced water.

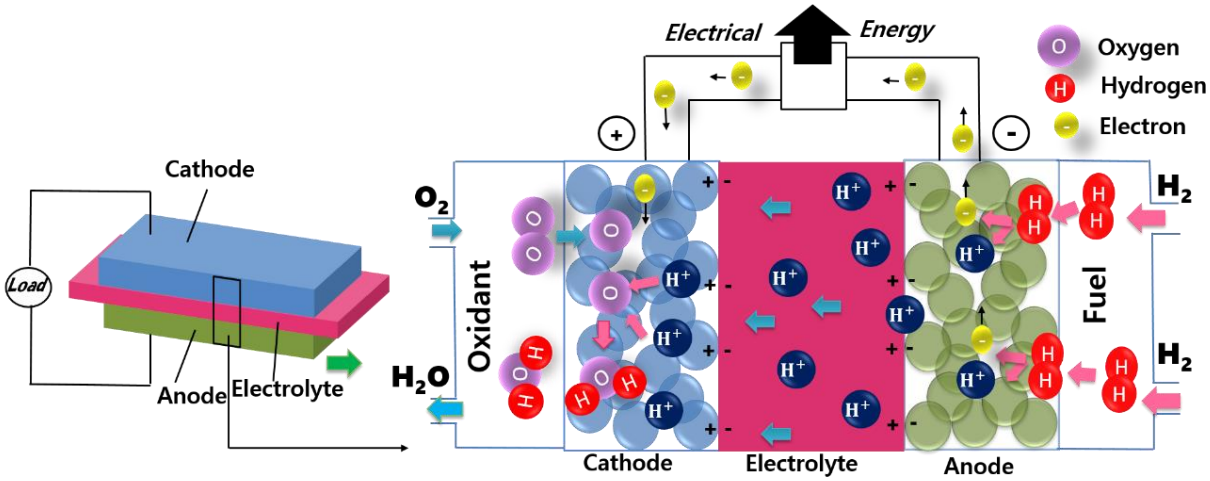

Figure 1.2 Mechanisms of proton conductor electrolyte solid oxide fuel cell

Figure 1.3 shows a SOFC using the other kind of electrolyte, in which the oxide ions produced at the cathode side, diffuse through the solid electrolyte towards the porous anode, where they participate in the electrochemical fuel oxidation. This is oxide ion conductor electrolyte. In this dissertation, this kind of oxide ion conductor was considered as the electrolyte.

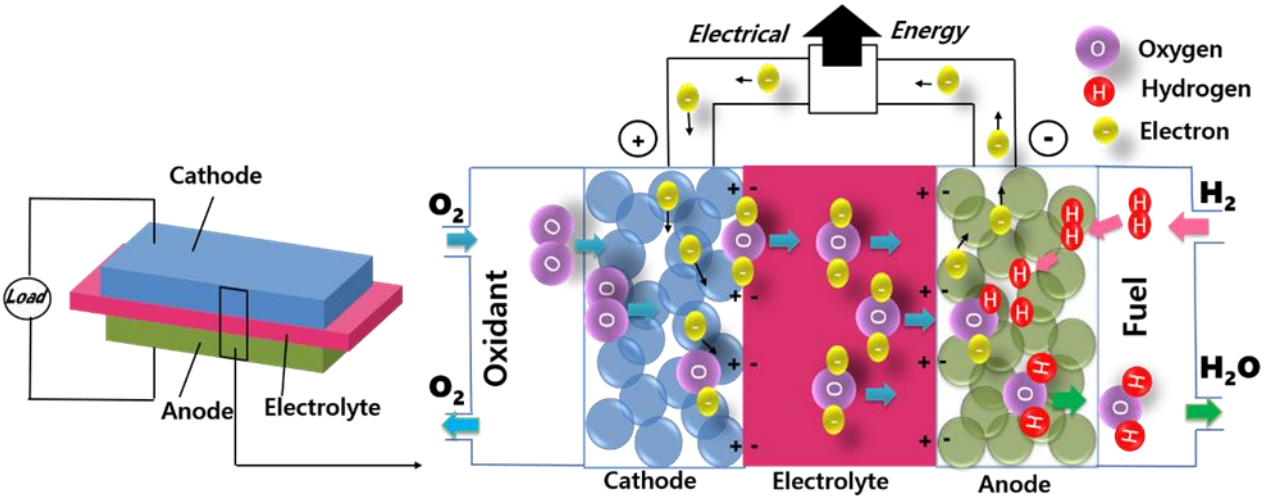

Figure 1.3 Mechanisms of oxide-ions conductor solid oxide fuel cell.

1.2 Development of solid oxide fuel cell materials

1.2.1 Electrolyte

An electrolyte is a component in a SOFC used for the ion transportation between the porous anode and cathode. High oxygen conductivity over a wide range of oxygen partial pressure is needed by an electrolyte. Electrolyte conducts oxide ions from the cathode to the anode where it reacts with hydrocarbons to form H_2O and CO_2, or just only H_2O in hydrogen as fuel, and thus completes the overall electrochemical reaction [2]. Therefore, the primary requirement for electrolyte materials is that it should have stable structure, good ionic conductivity to minimize Ohmic resistance but it should have little or no electron conductivity to minimize loss of current density. In addition, chemically inertness toward electrode materials during both processing and service, the electrolyte must be chemically compatible with electrode components of the anode and cathode. There are many problems such as stability and chemical compatibility with electrode materials during the development of electrolytes [3, 4]. For efficient operation of a SOFC with less the Ohmic losses, thin electrolyte thin-film is always necessary. Generally, the oxide ion conduction occurs through an oxygen vacancy hopping mechanism, which is a thermally activated process. Moreover, the electrolyte must be completely dense in order to avoid any cross-diffusion of fuel and oxidant constituents. Typically, in a metal oxide electrolyte, the size of the oxide ion is larger

than that of the metal cation. Thus, it is expected that the smaller sized cations are more likely to possess appreciable mobility in the lattice.

The most common oxygen ion conductor solid electrolyte materials used in SOFCs is yttria-stabilized zirconia (YSZ) [5], in which, Yttria is added in the cubic fluorite phase to stabilize the structure, increase the concentration of oxygen vacancy, and thus increase the ionic conductivity. Another most widely used oxide is gadolinia-doped ceria (GDC) [6], which also shows higher conductivity, and lower polarization resistance than YSZ. Unfortunately, current density will be decreased by the doping of ceria since ceria is an electronic conductor at low oxygen partial pressures. In addition, Lanthanum gallate ceramics, especially lanthanum strontium gallium magnesium perovskite (LSGM), are also used with excellent oxygen-ion conductivity behavior [7]. Its conductivity of LSGM is higher than that of YSZ but without any easily reducible ions. In this study, LSGM was used as the electrolyte material to evaluate the performance of the developed oxide electrode materials.

1.2.2 Anode

One of the most important compounds of SOFCs is the anode, which can promote reaction of the O^{2-} from the electrolyte and conduct the electrons produced in the following

electrochemical reaction:

$$H_2+O^{2-} = H_2O+ 2e^-$$

The anode must have important properties such as high electrical conductivity, matching of thermal expansion coefficient with electrolyte and good chemical compatibility with electrode, high coke resistance at reaction site, chemical compatibility with electrolyte, large triple phase boundary (TPB), and high porosity [8].

In recent years, several types of materials have been used as anodes for SOFCs especially Ni- zirconia cermet anodes. However, the thermal expansion of stabilized zirconia mismatches with Ni at high temperatures [8]. Agglomerating of the anode powder materials in a practical process will reduce the porosity of anode, and simultaneously decrease the triple-phase boundary (TPB) required for the cell operation, thereby decreasing the cell performance. Moreover, Ni could promotes the carbon formation, reducing the anode performance of Ni-YSZ [9]. In order to overcome the carbon formation on the anode, Zhan and Barnett [10] firstly used a Ru-CeO_2 layer on the outer surface of the Ni-YSZ anode as the catalysts, limiting the direct exposure of the Ni-based anode to the hydrocarbon. It is found that the Ni-GDC anode is an ideal anode material to match with GDC electrolyte. In order to improve the cell carbon deposition, Fe was doped on the Ni-GDC. The result showed that the carbon formation was greatly hindered on the Fe-Ni alloys anode when compared to

the Ni-based anodes. Kan et al. [11] found that $Ni_{0.9}Fe_{0.1}$-GDC anode maintained a stable cell performance was stable for 50 h with a maximum power density of 0.34 W cm^{-2} in the dry methane at 650 ^{o}C. In contrast, the Ni/GDC anode was only kept the stability for 12 h operation. Herein, the addition of Fe on the Ni/GDC anode induced the methane fuel to be decomposed more easily and oxidized more completely, enhancing long-term stability significantly.

Cermet based anodes are considered as the best alternative anode materials since they can resist sulfur poisoning and carbon deposition. A significant one is the Ceria containing Cermet, in which Ce^{4+} phase can be reduced to the Ce^{3+}phase in a reduced air atmosphere, which can generates the oxygen ion vacancy and promote the ions transfers, resulting in the excellent catalytic activity. $Ce_{1-x}M_xO_{2-\delta}$ (M = rare earth element), has been considered as an alternative to YSZ because its conductivity is 4-5 times higher than that of YSZ [12,13]. Even though Ni cermet shows high electronic conductivity and catalytic activity, but Ni-based anode is unstable on the hydrocarbon fuel because Ni exhibits a tendency to catalyze carbon formation [14-16]. In the investigation of high performance electrodes, Samaria-doped ceria (SDC) was also examined [17]. In fact, SDC is also synthesized as an electrolyte, which has the same oxygen ion conductivity with LSGM [18, 19]. Ceria oxide generates oxygen ion vacancy and frees electrons in the electrolyte, therefore, SDC also shows high

electronic conductivity [20]. In a conclusion, Ni cermet exhibits high electrical conductivity with high activity and low cost, which has been considered as the best choice for the SOFC anode. Meanwhile, Ceria-based materials were also confirmed as the high performance hydrocarbons oxidation catalyst in the anodes. The combination of Ni and ceria-based material is expected to enhance the fuel oxidation at the SOFC anode.

1.2.3 Cathode

Cathode is another most important part of SOFCs. In general, cathode materials are oxygen rich oxides, which must have high electrochemical activity on the surface for an efficient oxygen reduction reaction (ORR), high diffusivity for the transfer of oxygen anions through the cathode, good chemical compatibility with electrolyte and interconnect materials and suitable thermal expansion coefficient matching with other components.

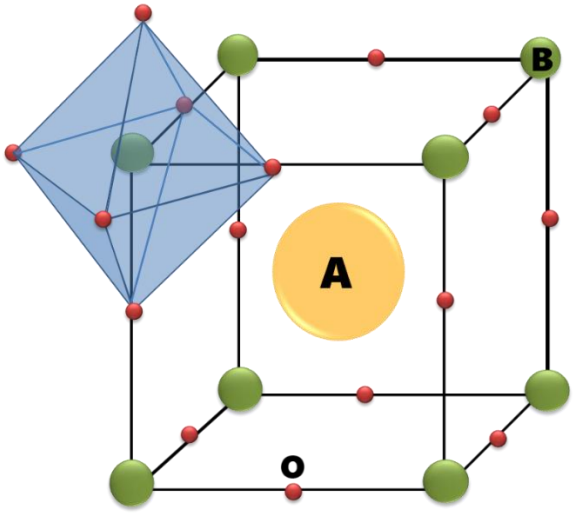

Figure 1.4 Cubic unit perovskite crystal structure.

Perovskite has always been selected as the best choice for a SOFC cathode material. Its properties can be significantly tuned by the cation ordering. Figure 1.4 shows a cubic unit perovskite chemical formula ABO_3 is shown in Figure 1.4, in which the A atoms are in the $(\frac{1}{2},\frac{1}{2},\frac{1}{2})$ position, the B atoms are in the (0,0,0) position, and oxygen atoms are in three positions ($\frac{1}{2}$, 0,0; 0, $\frac{1}{2}$,0; and 0,0, $\frac{1}{2}$). Herein, A-site cation is 12-fold-coordinated with oxygen ions, while the B-site cation is 6-fold-coordinated. Combining large oxide ion with small radius metal ion gives a cubic close-packed crystal structure of oxygen ions along with interstitial metal ions [21].

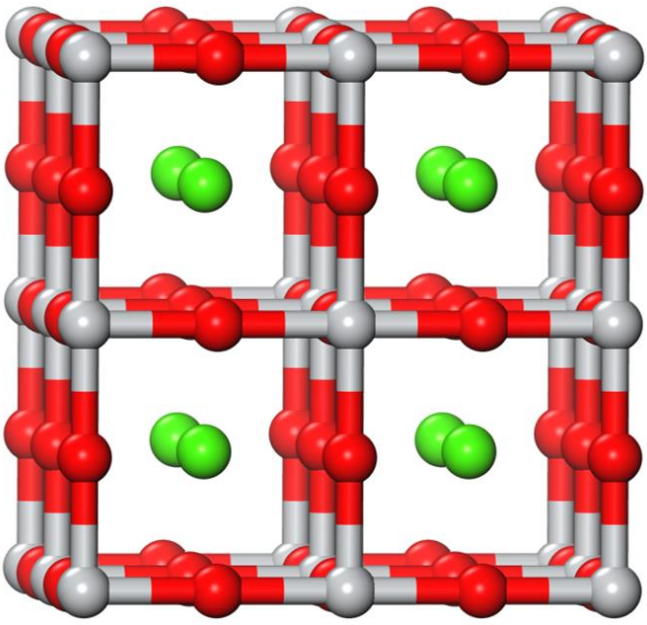

Figure 1.5 Constructed a model 2×2×2 perovskite.

In order to fit the cathode condition choice the mixed ionic and electronic conducting (MIEC) materials are always used as the cathode. As shown in Figure 1.6, the reactions only

occur on the surface of pure electronic conducting materials, in which only react on the surface path, as shown in Figure 1.6 generally two phase meeting point called double phase boundary (DPB) exists. In comparison, the MIEC have triple-phase boundary (TPB), where gas, cathode and electrolyte meeting point exists. As such, the reactions on the MIEC materials not only occur on the DPB but also on the TPB so that the MIEC materials have higher catalytic activity.

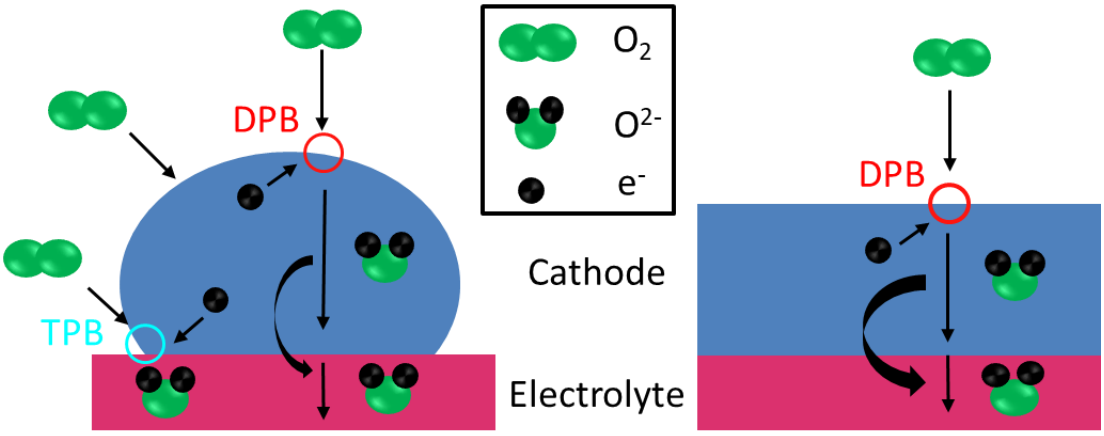

Figure 1.6 Schematic diagram of the cathode double phase boundary and triple phase boundary.

Moreover, MIEC materials allow ORR to occur on both surface and bulk pathes. In the MIEC materials, ORR occurs on TPB and also in the cathode itself by ions transferred through the bulk surface of the cathode because of the ionic conductivity property of MIEC materials.

Lanthanum Strontium-containing MIEC materials are widely used in the cathode. For

instance, $La_{0.8}Sr_{0.2}MnO_3$ [22], $La_{0.8}Sr_{0.2}FeO_3$ [22, 23], $La_{0.8}Sr_{0.2}CoO_3$ [22, 23] and $La_{0.6}Sr_{0.4}CoO_{3-\delta}$ [24] shows conductivities of 180, 90, 1360 and 2100 S cm^{-1} at 700 ^oC, respectively. Herein, the B-site doped cobalt obviously improved perovskite electrode electrical conductivity. However, this also leads to an increase in the coefficient of thermal expansion and mismatch between electrodes and electrolyte. Furthermore, the precursor cobalt nitrate is also a high cost chemical. In order to reduce the thermal expansion coefficient, Fe was doped on LSC. Especially, $La_{0.6}Sr_{0.4}Co_xFe_{1-x}O_{3-\delta}$ (LSCF) family attracted more attentions to find the optimum proportion of cobalt and iron. Kuhn et al. [25] investigated Fe-based perovskite type oxides with the formula $La_{0.6}Sr_{0.4}Co_yFe_{1-y}O_{3-\delta}$. Later the same group reported work about LSCF B-site doped Zn, Ni and Cu to increase oxygen activation and vacancy generations, and found that the Zn-doped catalyst showed the best performance [26]. Because perovskite materials electrical conductivity is affected by B-site metal, doping different metal on B-site could improve the conductivity by improving ORR. Wang et al. [27] doped copper to two different proportion LSCF ($La_{0.6}Sr_{0.4}Co_{0.2}Fe_{0.7}O_{3-\delta}$ and $La_{0.6}Sr_{0.4}Co_{0.1}Fe_{0.8}O_{3-\delta}$), and obtained much higher conductivity than LSCF. Other elements including Pt [28-30], Ag [30, 31] and Cu [26, 27, 32] were also doped on B-site. Serra et al [33] considered that the specific effect of B-site metal doping should be due to that metal substitution might promote the redox cycles of the charge carriers, and the redox of $Co^{3+/4+}$

and $Fe^{3+/4+}$ at B-site might enhance the reduction of oxygen atoms.

Other perovskites such as ABO_3-type oxides with A=Ln (lanthanides), Sr, Ba; B= Co, Fe, Mn, Ni, Nb, Mo. $Ba_xSr_{1-x}Co_yFe_{1-y}O_{3-\delta}$ were also investigated as high performance cathode materials for SOFCs with various electrolytes. Shao et al. [34] reported that Ni-SDC/SDC/$Ba_{0.5}Sr_{0.5}Co_{0.8}Fe_{0.2}O_{3-\delta}$ single cell with 20-μm-thick electrolyte had the maximum power density (MPD) of 1010 and 402 mW cm^{-2} at 600 and 500 ^oC, respectively, and the MPD was increased more with Ceria-doped $Gd_{0.1}Ce_{0.9}O_{1.95}$ (GDC) electrolyte, Liu et al. [35] reported that an anode supported single cell with BSCF as the cathode and Ni-GDC as the anode achieved MPD of 1329 and 454 mW cm^{-2} at 600 and 500^oC,respectively. Meanwhile, as LSGM electrolyte with high ionic conductivity was used, BSCF also gave a favorable cathodic performance. Martínez et al. [36] showed that the BSCF with 1.5-mm-thick LSGM electrolyte and $La_{0.75}Sr_{0.25}Cr_{0.5}Mn_{0.5}O_{3-\delta}$ (LSCM) as anode delivered MPD of 160 $mWcm^{-2}$ at 800 ^oC. However, as a cathode, YSZ has strong reaction with BSCF. To solve this problem, Duan et al. [37] added 1-μm-thick GDC buffering layer between YSZ and BSCF, which delivered the maximum power density of 1.56 W cm^{-2} at 800 ^oC when using hydrogen as fuel and air as oxidant.

With the development and maturity of cathode materials, researchers start to investigate Praseodymium (Pr) doping effect because its electron distribution and structural

characterization are similar to the rare-earth elements such as lanthanum (La) [38]. Meng et al. [39] characterized $Pr_{1-x}Sr_xCo_{0.8}Fe_{0.2}O_{3-\delta}$($0.2\leq x\leq 0.6$) cathode materials, and investigated thermal expansion coefficient between 30 ºC and 850 ºC, which were about 19.69×10^{-6} K^{-1} (x = 0.4) and 21.23×10^{-6} K^{-1} (x = 0.6). The electrical conductivities of $Pr_{1-x}Sr_xCo_{0.8}Fe_{0.2}O_{3-\delta}$ (x = 0.2–0.6) were all higher than 279 S cm^{-1}. Hansen [40] also reported that $(Pr_{0.6}Sr_{0.4})_{1-s}Co_{0.8}Fe_{0.2}O_{3-\delta}$ as SOFC cathode showed the maximum conductivity 402 S cm^{-1} at 520 ºC when s was 0.01. Meanwhile, as s was 0.05, the minimum total area specific resistances (ASRs) were 0.05, 0.20 and 1.72 at 800, 700 and 600 ºC, respectively. Other materials such as scandium-doped $Pr_{0.6}Sr_{0.4}(Co_{0.2}Fe_{0.8})_{(1-x)}Sc_xO_{3-\delta}$ [41] and Mo-doped perovskite $Pr_{0.4}Sr_{0.6}(Co_{0.2}Fe_{0.8})_{1-x}Mo_xO_{3-\delta}$ [42] were also investigated

1.3 Development of symmetrical SOFCs

With the development of electrode materials for SOFCs, reducing the cost and saving time are always desired. In the past few years, a novel SOFC named as the symmetrical Solid Oxide Fuel Cells (SSOFC) was proposed, in which the same porous electrode material was used as cathode and anode on both sides of the dense electrolyte. Since the electrolyte and the symmetrical electrodes can be assembled by just one sintering step, the fabrication cost and time can be greatly decreased. Meanwhile, this can solve thermal expansion mismatch

among three different materials and only consider the chemical compatibility between two materials. Furthermore, when hydrocarbon is used as the fuel, it is easily cracked on the anode, resulting in carbon deposition. In this case, as shown in Figure 1.7, when SOFC with symmetric electrodes, as the coke is formed on the anode, the gas lines for the cathode and anode can be exchanged so that the coke is burnt out by oxygen and electrode can be worked as the cathode continuously. As such, the SSOFCs can work well for a long time in the hydrocarbon fuels.

The first research on the symmetric electrode materials was started in 2007. The lanthanum calcium-based or lanthanum strontium- based symmetric electrodes have been investigated in details. Ruiz-Morales et al. [42] reported that SSOFCs with the electrode material of $La_{0.7}Ca_{0.3}CrO_{3-\delta}$ (LCC) showed MPD of 110 and 25 mW cm^{-2} as H_2 and CH_4 were used as the fuels respectively, at 950 ^oC with a electrolyte thickness of 2000 μm. Then, LCC contained LCC-YSZ [43] and LCC-CGO20 [44] were investigated, which achieved MPD of 92.1 mW cm^{-2} at 850 ^oC with 350 μm thickness YSZ electrolyte and 573 mW cm^{-2} @900 ^oC with 300 μm thickness LSGM electrolyte, respectively. In additions, $La_{0.75}Sr_{0.25}Cr_{0.5}Mn_{0.5}O_3$ (LSCM) was also developed as the symmetric electrode materials, but it showed a poor power density.

Various SSOFCs with different electrodes containing LSCM and YSZ, such as

$(La_{0.75}Sr_{0.25})_{0.9}Cr_{0.5}Mn_{0.5}O_{3-\delta}$ /LSCM: YSZ (7:3)/YSZ/LSCM: YSZ (7:3)/ $(La_{0.75}Sr_{0.25})_{0.9}Cr_{0.5}Mn_{0.5}O_{3-\delta}$ [45], LSCM: CGO: YSZ with ratio of 2:1:1 [46], LSCM:YSZ (63 wt% YSZ) and LSCM:YSZ (63 wt% YSZ) + 5 wt% CSO [47] were also developed.

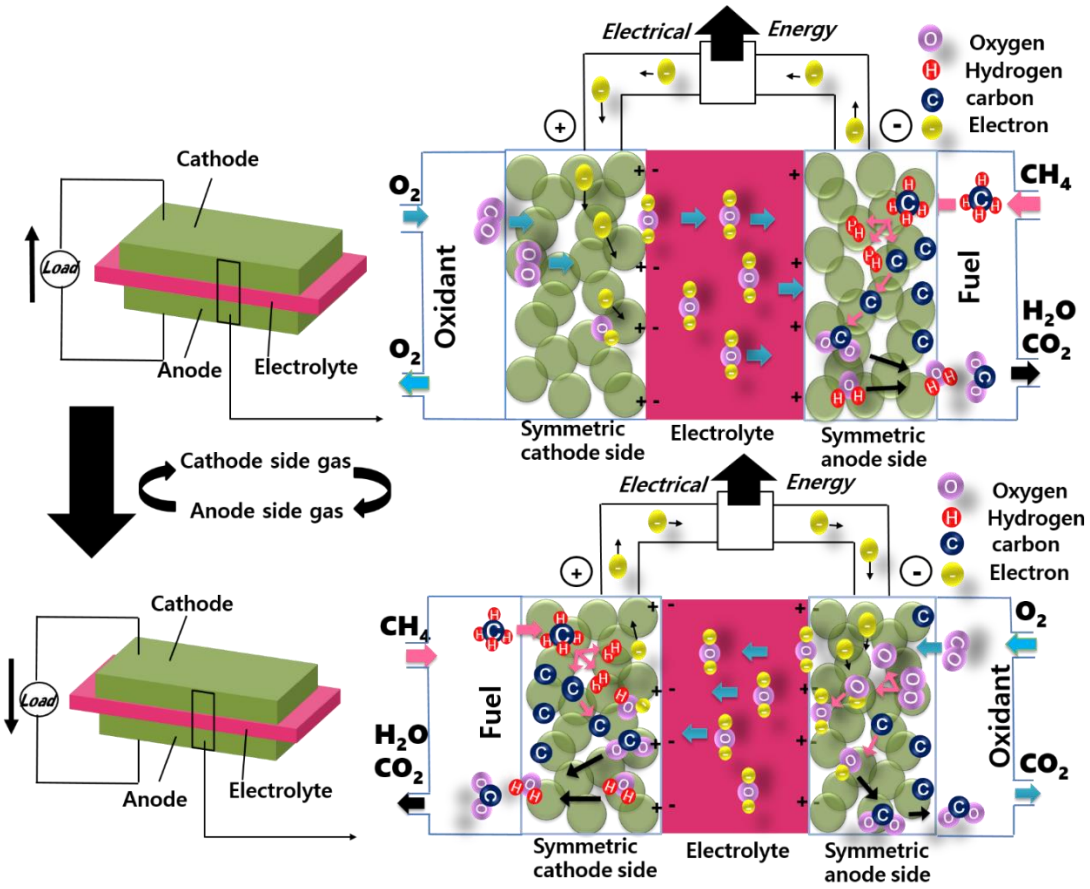

Figure 1.7 Schematic diagram of symmetric SOFC.

However, low power density was obtained by using these materials except LSCM:YSZ (1 : 1) [48] and LSCM:YSZ (63 wt%YSZ) + 6 wt% Ni [47]. MPD achieved by LSCM:YSZ (1 : 1) at 950 ^{o}C were 546 and 347 mWcm^{-2} for H_2 and CH_4 fuels respectively with a 250µm thickness YSZ. The MPDs of the symmetric cells with LSCM:YSZ (63 wt%YSZ) + 6 wt% Ni were 570 mWcm^{-2} in H_2 and 550 mWcm^{-2} in CH_4 respectively at 900 ^{o}C. El-Himri et al.

[49] substituted La with Pr in LSCM, and investigated the cell performance by using $Pr_{0.7}Ca_{0.3}Cr_{1-y}Mn_yO_{3-\delta}$ (y=0.2, 0.4, 0.6, 0.8). It is found that the SSOFCs with $Pr_{0.7}Ca_{0.3}Cr_{0.6}Mn_{0.4}O_{3-\delta}$ electrodes exhibited MPDs of 250 and 160 $mWcm^{-2}$ at 950 ^oC, under H_2 and CH_4, respectively.

Only a few reports with high MPD materials can be found. Since the symmetric electrode is generally started from the cathode material of SOFC, it always shows much lower electronic and ionic conductivity in a reducing environment than in an oxidizing environment [50, 51]. Therefore, developing the novel materials as the symmetric electrode directly is the best choice. Liu et al. [52] reported a novel symmetric electrode material of $Sr_2Fe_{1.5}Mo_{0.5}O_{6-\delta}$, which can work well with the LSGM electrolyte, showing high electrical conductivities of 550 Scm^{-1} and 310 Scm^{-1} at 780 ^oC in air and hydrogen, respectively, and polarization resistances of symmetric cell in air and in hydrogen of 0.10 and 0.21 $\Omega\ cm^2$ at 850 ^oC, respectively. In the case using 265μm thickness electrolyte, MPDs at 900 ^oC in wet H_2 and CH_4 reached 835 and 230 $mWcm^{-2,}$ respectively, indicating excellent redox ability. Zhang et al. [53] synthesized $(Pr_{0.4})_{1.05}Sr_{0.6}Co_{0.2}Fe_{0.7}Nb_{0.1}O_{3-\delta}$, which showed excellent performance in wet H_2 and CH_4 at 900 ^oC with MPDs of 1130 and 670 $mWcm^{-2}$, respectively. Cerium doped $La_{0.7}Sr_{0.3}Fe_{0.9}Ni_{0.1}O_{3-\delta}$ also exhibited good redox ability. When it was used in SSOFC, MPDs reached 889 and 522 $mWcm^{-2}$ at 850 ^oC under H_2 and CH_4, respectively [54].

A-site Samarium doped electrode materials for SSOFCs were also discovered by some researchers. Zhang et al. [55] synthesized $SmBaMn_2O_{5+\delta}$, which showed high electrical conductivity in air and in wet H_2 and exhibited acceptable polarization resistances under air and H_2, i.e., 0.066 and 0.313Ω cm^2 at 900 ^oC, respectively. The obtained symmetric cell showed a MPD at 900^oC of 782 $mWcm^{-2}$ with Co-Fe catalyst in H_2. In contrast, Fan et al. [56] synthesized $Sm_{0.8}Sr_{0.2}Fe_{0.8}Ti_{0.15}Ru_{0.05}O_{3-\delta}$ and $Sm_{0.7}Sr_{0.2}Fe_{0.8}Ti_{0.15}Ru_{0.05}O_{3-\delta}$ (SSFTR) and used as the symmetric electrode. Compared with two proportions of A-site deficient SSFTR, although the MPD was improved, the values were only 271 and 417 mW cm^{-2} at 800 ^oC, respectively. All in all, the symmetric electrode materials must have either cathode or anode properties, because the same materials will be operated in air and hydrogen atmosphere, the materials with strong redox ability are acceptable. To date, the candidates of the symmetrical electrode material are very limited.

1.4 Objective of this study

As reviewed above, cermet electrodes especially the perovskite cermet are still considered as the best choice for the oxidation of fuels in SOFC due to their high electrical conductivities and good catalytic activity. However, the common anode and cathode materials still show some problems, such as the mismatch among the anode, cathode, and electrolyte, leading to

poor long-term stability; poor electrical conductivity, leading to high resistance and low catalytic activity of cathode at low temperature; carbon deposition, resulting in losing activity of anode. The objective of this study is the development of novel electrode materials, especially cathode electrode materials, which have similar thermal expansion values with electrolyte, high electrical conductivity for the oxygen reduction reaction to keep high oxygen reduction kinetics at low temperatures. Furthermore, the symmetric SOFCs with the developed electrode materials were fabricated to solve the coking problem in the case of the direct use of hydrocarbon fuels.

1.5 Scope of this dissertation

Chapter 1 reviews the progress of development of various electrodes for SOFCs, especially the symmetric electrode materials and states the objectives of this study.

Chapter 2 gives detailed descriptions about synthesis process of various materials, characterization and measurements method, including cell performance system setup with some schematic diagrams.

Chapter 3 focuses on the B-site Niobium doped $Pr_{0.4}Sr_{0.6}(Co_{0.3}Fe_{0.6})_{1-x}Nb_xO_{3-\delta}$ (PSCFNx), i.e., a novel peroviskite oxide for SOFC cathode materials. The crystal structure, electrical conductivity, thermal expasion, X- ray photoelectron sepectrum and

electrical impedance sepectrum were incestigated. Optimum proportion with high cell performance was obtained for the cathode materials, and the stability was tested under constant current density. The results showed that $PSCFN_{0.5}$ is a promissing cathode for SOFC.

Chapter 4 introduces a novel peroviskite $(Ce_{0.1}Sr_{0.9})_xCo_{0.3}Fe_{0.7}O_{3-\delta}$ for SOFC cathode. By creating A-site deficiency can provide more oxygen vacancies, and enhance oxygen ion conductivity in the cathode. The electrical conductivity, X-ray photoelectron spectrum, O_2-TPD and electrical impedance spectrum were investigated. The cell performance test was conducted to determine whether the A-deficient can enhanced catalytic activity.

In **Chapter 5**, $Pr_{0.4}Sr_{0.6}Co_{0.9-x}$ $Fe_xNb_{0.1}O_{3-\delta}$ oxide was evaluated as the symmetrical electrode for SSOFCs. The redox ability of PSCFN under either air or H_2 environments was checked. The crystal structure, electrical conductivity, thermal expasion, X- ray photoelectron sepectrum and electrical impedance sepectrum were investigated. Furthermore, the effects of different proportions of Fe and Co on materials were discussed.

Chapter 6 gives the general conclusions of this research and discusses the challenges and prospects for the future work.

References

[1] H. Taroco, J. Santos, R. Domingues, T. Matencio, Ceramic materials for solid oxide fuel cells. INTECH Open Access Publisher, 2011.

[2] N. Mahato, A. Banerjee, A. Gupta, S. Omar, K. Balani. Progress in material selection for solid oxide fuel cell technology: A review. Prog Mater Sci. 72 (2015) 141–337.

[3] S. M. Haile, G. Staneff and K. H. Ryu, Non-stoichiometry, grain boundary transport and chemical stability of proton conducting perovskites. J Mater Sci 36 (2001) 1149-1160.

[4] P. Sawant, S. Varma, B. N. Wani and S. R. Bharadwaj, Synthesis, stability and conductivity of $BaCe_{0.8-x}Zr_xY_{0.2}O_{3-\delta}$ as electrolyte for proton conducting SOFC. Int J Hydrogen Energ 37 (2012) 3848-3856.

[5] J. W. Fergus, Electrolytes for solid oxide fuel cells. J Power Sources 162 (2006) 30-40.

[6] D. S. Khaerudini, G. Guan, P. Zhang, X. Hao, A. Abudula, Prospects of oxide ionic conductivity bismuth vanadate-based solid electrolytes, Rev Chem Eng 30 (2014) 539-551.

[7] N. Liu, M. Shi, C. Wang, Y. P. Yuan, P. Majewski and F. Aldinger, Microstructure and ionic conductivity of Sr- and Mg-doped $LaGaO_3$. J Mater Sci 41 (2006) 4205-4213.

[8] S. P. S. Shaikh, A. Muchtar, M. R. Somalu, A review on the selection of anodes materials for solid oxide fuel cells, Renew Sust Energ Rev, 51 (2015) 1-8.

[9] H. Inaba, H. Tagawa, Ceria-based solid electrolytes, Solid State Ion ,83(1996) 1–16.

[10] Z. Zhan and S. A. Barnett, An octane-fueled solid oxide fuel cell. Science 308 (2005) 844-847.

[11] H. Kan , H. Lee, Enhanced stability of Ni–Fe/GDC solid oxide fuel cell anodes for dry methane fuel. Catal Commun 12 (2010) 36-39

[12] O.A. Marina, M. Mogensen, High-temperature conversion of methane on a composite gadolinia-doped ceria–gold electrode. Appl Catal A: Gen 189 (1999) 117–126.

[13] J.B. Goodenough, Y.H. Huang, Alternative anode materials for solid oxide fuel cells. J Power Sources, 173 (2007) 1–10.

[14] R. T. K. Baker, Catalytic growth of carbon filaments. Carbon, 27 (1989) 315–323.

[15] M.L. Toebes, J.H. Bitter, A.J. Van Dillen, K.P. de Jong, Impact of the structure and reactivity of nickel particles on the catalytic growth of carbon nanofibers, Catal Today 76 (2002) 33–42.

[16] E. Ivers-Tiffée, A. Weber, D Herbstritt, Materials and technologies for SOFC components. J Eur Ceram Soc, 21 (2001) 1805–1811.

[17] X. Zhang, S. Ohara, R. Maric, K. Mukai, T. Fukui, H. Yoshida, M. Nishimura, T. Inagaki, K. Miura, Ni-SDC cermet anode for medium-temperature solid oxide fuel cell with lanthanum gallate electrolyte, J Power Sources, 83 (1999) 170-177.

[18] K. Eguchi, Ceramic materials containing rare earth oxides for solid oxide fuel cell,

J. Alloys Compd. 250 (1997) 486-491.

[19] K. Eguchi, T. Setoguchi, T. Inoue, H. Arai, Electrical properties of ceria-based oxides and their application to solid oxide fuel cells, Solid State Ion, 52 (1992) 165-172.

[20] H. Uchida, H. Suzuki, M. Watanabe, High‐Performance Electrode for Medium‐Temperature Solid Oxide Fuel Cells: Effects of Composition and Microstructures on Performance of Ceria‐Based Anodes J Electrochem Soc, 145 (1998) 615-620.

[21] A. Jun, J. Kim, J. Shin, G. Kim, Perovskite as a Cathode Material: A Review of its Role in Solid‐Oxide Fuel Cell Technology, chemelectrochem, 3(2016) 511-530.

[22] F. Tietz, I. Arul Raj, M. Zahid, D. Stover, Electrical conductivity and thermal expansion of $La_{0.8}Sr_{0.2}(Mn,Fe,Co)O_{3-\delta}$ perovskites, Solid State Ion, 177(2006) 1753–1756.

[23] L. W. Tai, M. M. Nasrallah, H. U. Anderson, D. M. Sparlin, S. R. Sehlin, Solid State Ionics 1995, 76, 259–271.

[24] O. Gwon, S. Yoo, J. Shin, G. Kim, Optimization of $La_{1-x}Sr_xCoO_{3-\delta}$ perovskite cathodes for intermediate temperature solid oxide fuel cells through the analysis of crystal structure and electrical properties, Int. J. Hydrogen Energy, 39 (2014) 20806–20811.

[25] J.N. Kuhn, U.S. Ozkan, Effect of Co content upon the bulk structure of Sr- and Co-doped $LaFeO_3$, Catal Lett, 121(2008) 179–188.

[26] S.F. Wang, C.T. Yeh, Y.R. Wang, Y.F. Hsu, Effects of $(LaSr)(CoFeCu)O_{3-\delta}$

cathodes on the characteristics of intermediate temperature solid oxide fuel cells, J. Power Sources, 201(2012) 18–25.

[27] N. Lakshminarayanan, H. Choi, J.N. Kuhn, U.S. Ozkan, Effect of additional B-site transition metal doping on oxygen transport and activation characteristics in $La_{0.6}Sr_{0.4}Co_{0.18}Fe_{0.72}X_{0.1}O_{3-\delta}$ (where X = Zn, Ni or Cu) perovskite oxides, Appl. Catal. B, 103 (2011) 318–325.

[28] H.J. Hwang, J.W. Moon, S. Lee, E.A. Lee, Electrochemical performance of LSCF-based composite cathodes for intermediate temperature SOFCs, J. Power Sources, 145 (2005) 243–248.

[29]. K. Sasaki, J. Tamura, H. Hosoda, T.N. Lan, K. Yasumoto, M. Dokiya, Pt-perovskite cermet cathode for reduced-temperature SOFCs. Solid State Ion, 148 (2002) 551–555.

[30] V.A.C. Haanappel, D. Rutenbeck, A. Mai, S. Uhlenbruck, D. Sebold, H. Wesemeyer, B. Röwekamp, C. Tropartz, F. Tietz, The influence of noble-metal-containing cathodes on the electrochemical performance of anode-supported SOFCs. J. Power Sources, 130(2004) 119–128.

[31] S. Wang, T. Kato, S. Nagata, T. Honda, T. Kaneko, N. Iwashita, M. Dokiya, Performance of a $La_{0.6}Sr_{0.4}Co_{0.8}Fe_{0.2}O_3$-$Ce_{0.8}Gd_{0.2}O_{1.9}$-Ag cathode for ceria electrolyte SOFCs. Solid State Ion, 146(2002) 203–210.

[32] T.J. Huang, X.D. Shen, C.L. Chou, Characterization of Cu, Ag and Pt added $La_{0.6}Sr_{0.4}Co_{0.2}Fe_{0.8}O_{3-\delta}$ and gadolinia-doped ceria as solid oxide fuel cell electrodes by temperature-programmed techniques. J. Power Sources, 187 (2009) 348–355.

[33] J.M. Serra, H.P. Buchkremer, On the nanostructuring and catalytic promotion of intermediate temperature solid oxide fuel cell (IT-SOFC) cathodes, J Power Sources, 172 (2007) 768–774.

[34] Z.P. Shao, S.M. Haile, A high-performance cathode for the next generation of solid-oxide fuel cells, Nature 431 (2004) 170-174.

[35] Q.L. Liu, K.A. Khor, S.H. Chan, High-performance low-temperature solid oxide fuel cell with novel BSCF cathode, J. Power Sources 161 (2006) 123-128.

[36] J. Pe˜na-Martínez, D. Marrero-López, J.C. Ruiz-Morales, B.E. Buergler, P. Nú˜nez, L.J. Gauckler, SOFC test using $Ba_{0.5}Sr_{0.5}Co_{0.8}Fe_{0.2}O_{3-\delta}$ as cathode on $La_{0.9}Sr_{0.1}Ga_{0.8}Mg_{0.2}O_{2.85}$ electrolyte, Solid State Ionics 177 (2006) 2143-2147.

[37] Z. Duan, M. Yang, A. Yan, Z. Hou, Y. Dong, Y. Chong, M. Cheng,W. Yang, J. Power Sources 160 (2006) 57.

[38] R. Ran, X. Wu, C. Quan, D. Weng, Effect of strontium and cerium doping on the structural and catalytic properties of $PrMnO_3$ oxides, Solid State Ion, 176 (2005) 965–971.

[39] X. Meng, S. Lu, Y. Ji, T. Wei, Y. Zhang, Characterization of $Pr_{1-x}Sr_xCo_{0.8}Fe_{0.2}O_{3-\delta}$

($0.2 \leq x \leq 0.6$) cathode materials for intermediate-temperature solid oxide fuel cells, J Power Sources, 183 (2008) 581-585.

[40] K.K. Hansen, A-Site Deficient $(Pr_{0.6}Sr_{0.4})_{1-s}Fe_{0.8}Co_{0.2}O_{3-\delta}$ Perovskites as Solid Oxide Fuel Cell Cathodes, J Electrochem Soc, 156 (2009) B1257-B1260.

[41] Y. Yin, M. Xiong, N. Yang, Z. Tong, Y. Guo, Z. Ma, E. Sun, J. Yamanis, B. Jing, Investigation on thermal, electrical, and electrochemical properties of scandium-doped $Pr_{0.6}Sr_{0.4}(Co_{0.2}Fe_{0.8})_{(1-x)}Sc_xO_{3-\delta}$ as cathode for IT-SOFC, Int J Hydrogen Energy, 36 (2011) 3989-3996.

[42] P. Zhang, G. Guan, D. S. Khaerudini, X. Hao, C. Xue, M. Han, Y. Kasai, A. Abudula, Mo doped $Pr_{0.4}Sr_{0.6}Co_{0.2}Fe_{0.8}O_{3-\delta}$ cathode material with high catalytic activity for intermediate-temperature solid oxide fuel cells, Electrochim Acta, 146 (2014) 591-597.

[42] J. C. Ruiz-Morales, H. Lincke, D. Marrero-Lo´ pez, J. Canales-Va´zquez and P. Nu´n˜ ez, Lanthanum chromite materials as potential symmetrical electrodes for Solid Oxide Fuel Cells ,Bol. Soc. Esp. Ceram. V., 46 (2007) 218-223.

[43] B. Lin, S. Wang, X. Liu and G. Meng, Simple solid oxide fuel cells, J Alloys Compd, 490 (2010) 214-222.

[44] Y. Zhang, Q. Zhou and T. He, $La_{0.7}Ca_{0.3}CrO_3$–$Ce_{0.8}Gd_{0.2}O_{1.9}$ composites as symmetrical electrodes for solid-oxide fuel cells, J. Power Sources, 196 (2011) 76-83.

[45] D. M. Bastidas, S. Tao and J. T. S. Irvine, A symmetrical solid oxide fuel cell demonstrating redox stable perovskite electrodes, J Mater Chem, 16(2006) 1603-1605.

[46] J. C. Ruiz-Morales, J. Canales-Va´zquez, B. Ballesteros-Pe´rez, J. Pen˜a-Martı´nez, D. Marrero-Lo´ pez, J. T. S. Irvine and P. Nu´n˜ ez, LSCM–(YSZ–CGO) composites as improved symmetrical electrodes for solid oxide fuel cells, J Eur Ceram Soc, 27 (2007) 4223-4227.

[47] G. Kim, G. Corre, J. T. S. Irvine, J. M. Vohs, R. J. Gorte, Engineering Composite Oxide SOFC Anodes for Efficient Oxidation of Methane, Electrochem. Solid-State Lett., 11 (2008) B16-B19.

[48] J. C. Ruiz-Morales, J. Canales-Va´zquez, J. Pen˜a-Martı´nez, D. Marrero-Lo´pez and P. Nu´n˜ ez, On the simultaneous use of $La_{0.75}Sr_{0.25}Cr_{0.5}Mn_{0.5}O_{3-\delta}$ as both anode and cathode material with improved microstructure in solid oxide fuel cells, Electrochim. Acta, 52(2006) 278-284.

[49] A. El-Himri, D. Marrero-López, J. C. Ruiz-Morales, J. Peña-Martínez, P. Núñez, Structural and electrochemical characterisation of $Pr_{0.7}Ca_{0.3}Cr_{1-y}Mn_yO_{3-\delta}$ as symmetrical solid oxide fuel cell electrodes, J Power Sources, 188(2009) 230-237.

[50] A. Yan, M. Cheng, Y. Dong, W. Yang, V. Maragou, S. Song and P. Tsiakaras, Investigation of a $Ba_{0.5}Sr_{0.5}Co_{0.8}Fe_{0.2}O_{3-\delta}$ based cathode IT-SOFC. Appl Catal B: Environ,

66 (2006) 64-71.

[51] A. Yan, V. Maragou, A. Arico, M. Cheng and P. Tsiakaras, Investigation of a $Ba_{0.5}Sr_{0.5}Co_{0.8}Fe_{0.2}O_{3-\delta}$ based cathode SOFC. Appl Catal B: Environ, 76 (2007) 320-327.

[52] Q. Liu, X. Dong, G. Xiao, F. Zhao, F. Chen, A novel electrode material for symmetrical SOFCs, Adv. Mater. 22 (2010) 5478-5482.

[53] P. Zhang, G. Guan, D. S. Khaerudini, X. Hao, M. Han, Y. Kasai, K. Sasagawa, A. Abudula, Properties of A-site nonstoichiometry $(Pr_{0.4})_xSr_{0.6}Co_{0.2}Fe_{0.7}Nb_{0.1}O_{3-\delta}$ ($0.9 \leq x \leq 1.1$) as symmetrical electrode material for solid oxide fuel cells, J Power Sources 248 (2014) 163-171.

[54] L. Bian, C. Duan, L. Wang, R.O. Hayre, J. Cheng, K.C. Chou, Ce-doped $La_{0.7}Sr_{0.3}Fe_{0.9}Ni_{0.1}O_{3-\delta}$ as symmetrical electrodes for high performance direct hydrocarbon solid oxide fuel cells, J Mater Chem A, 5(2017) 15253-15259.

[55] Y. Zhang, H. Zhao, Z. Du, K. Swierczek, Y. Li, High performance $SmBaMn_2O_{5+\delta}$ electrode for symmetrical solid oxide fuel cell, ACS Appl Mater Inter, 31 (2019) 3784-3793.

[56] W. Fan, Z. Sun, Y. Bai, K. Wu, Y. Cheng, Highly stable and efficient perovskite ferrite electrode for symmetrical solid oxide fuel cells, ACS Appl Mater Inter, 11 (2019) 23168-23179.

Chapter 2 Experimental

2.1 Sample preparation

2.1.1 Powder synthesis

$Pr_{0.4}Sr_{0.6}(Co_{0.3}Fe_{0.6})_{1-x}Nb_xO_{3-\delta}$ ($PSCFN_x$) (x=0, 0.05, 0.1 and 0.2) perovskites were prepared by the solid-state reaction from the oxide, nitrate and carbonate powders with high purity: $Pr(NO_3)_3 \cdot 6H_2O$, $SrCO_3$, $Co(NO_3)_2 \cdot 6H_2O$, Fe_2O_3 and Nb_2O_5 (99.9% Wako, Japan). The stoichiometric amounts of these materials were completely mixedwith ethanol and milled for 8 h in a planetary ball mill. The resulting mixture was wash with ethanol and magnetic stirring until most ethanol dry, then dry at 100^oC for 12 h and thoroughly ground and calcined in air for 10 h with different temperature, find optimum calcined temperature at 1050 ^oC. To ensure complete reaction the powders were intermediate ground and re-calcined using similar temperature and time.

$(Ce_{0.1}Sr_{0.9})_xCo_{0.3}Fe_{0.7}O_{3-\delta}$ ((CS)xCF) (x=0.90, 0.95, 1.0, 1.05and 1.10) perovskites were prepared by using a solid-state reaction method, in which oxide, nitrate and carbonate powders, i.e., $Ce(NO_3)_3 \cdot 6H_2O$, $SrCO_3$, $Co(NO_3)_2 \cdot 6H_2O$ and Fe_2O_3 (99.9% Wako, Japan), were used. The stoichiometric amounts of these chemicals were completely mixed by ball milling for 10 h at first, and then calcined at 1100 °C for 10 h in air. Herein, based on the preliminary experiments, it is found that when the mixtures were calcined at this condition,

the pure phase can be obtained. Finally, the obtained product with pure phase was treated by ball milling for 5 h again.

$Pr_{0.4}Sr_{0.6}Co_{0.9-x}Fe_xNb_{0.1}O_{3-\delta}$ ($PSCF_xN$) (x=0, 0.2, 0.4, 0.6 and 0.9) perovskite oxides were prepared by using the solid-state reaction method, in which the chemicals with high purity, i.e., $Pr(NO_3)_3 \cdot 6H_2O$, $SrCO_3$, $Co(NO_3)_2 \cdot 6H_2O$, Fe_2O_3 and Nb_2O_5 (all with 99.9% purity, Wako, Japan), were used. The stoichiometric amounts of these chemicals were completely mixed by the ball milling for 10 h at first, and then calcined in air. Based on the preliminary experiments, it was found that the pure phase was obtained when the mixed powders were calcined at 1100 °C for 7 h in air. Finally, the obtained powder with pure phase was treated by ball-milling for 3 h again.

2.1.2 Single cell preparation

$La_{0.8}Sr_{0.2}Ga_{0.8}Mg_{0.2}O_{3-\delta}$ (LSGM, 99.9% FCM, USA), was used for the fabrication of electrolyte, the powders wee further ground mixing with 1 wt.% PVB (PolyvynilButyral, Butvar B-98, Sigma-Aldrich, German) binder to make a tablet sample (20 mm in diameter × 1 mm in thickness) and compacted at 220MPa for 2 minutes. The prepared tablet were then sintering for 10 h at 1450 ^oCin air, heating and cooling rates of 3 $^oC\ min^{-1}$ during room temperature to 700^oC, until 700^oC to 1450^oC heating and cooling rates of 2 $^oC\ min^{-1}$to obtain the dense samples.

Electrodes (PSCFNx, $(CS)_xCF$, $PSCF_xN$). Electrode materials paste was made by mixing the desired weight ratio of the powder with organic additive binder (α-terpineol + ethyl cellulose) solution to form slurry. Once an appropriate viscosity was reached, the slurry coat on electrolyte both sideby doctor blade method, get symmetrical electrode cells for electrical impedance test (EIS), and control electrolyte thickness around 500 μm, the electrode thinkness of around 40μm and geometric surface areas of ~0.78 cm^2. These cells were dried at 100 ^oC for 30-60 minutes and subsequently sintered at desired sintering temperatures of different electrodes (1250 ^oC for 2 h for $PSCFN_x$, 1300 ^oC for 2 h for $(CS)_xCF$ and $PSCF_xN$).

Single cell. Single cell studied in this work was LSGM electrolyte supported (~ 300μm thickness) fuel cell. LSGM electrolyte supported cell was fabricated to evaluate the electrochemical performance of investigated cathodes. In this study testing two type fuel cell, one is single cell both side will used investigated cathode materials and Ni-SDC as anode materials, another is symmetric cell electrolyte both side used same electrode materials. For single cell anode materials the powder consisting of 50 wt.% NiO and 50 wt.% SDC were mixed and slurry coat on the surface of the dense electrolyte and sintered at 1350 ^oC for 2 h. the cathode slurry was coated on the opposite side of the electrolyte, followed by sintering similar as in the symmetric cell for EIS. Au paste and Pt mesh was used as the current collector for all electrochemical evaluations.

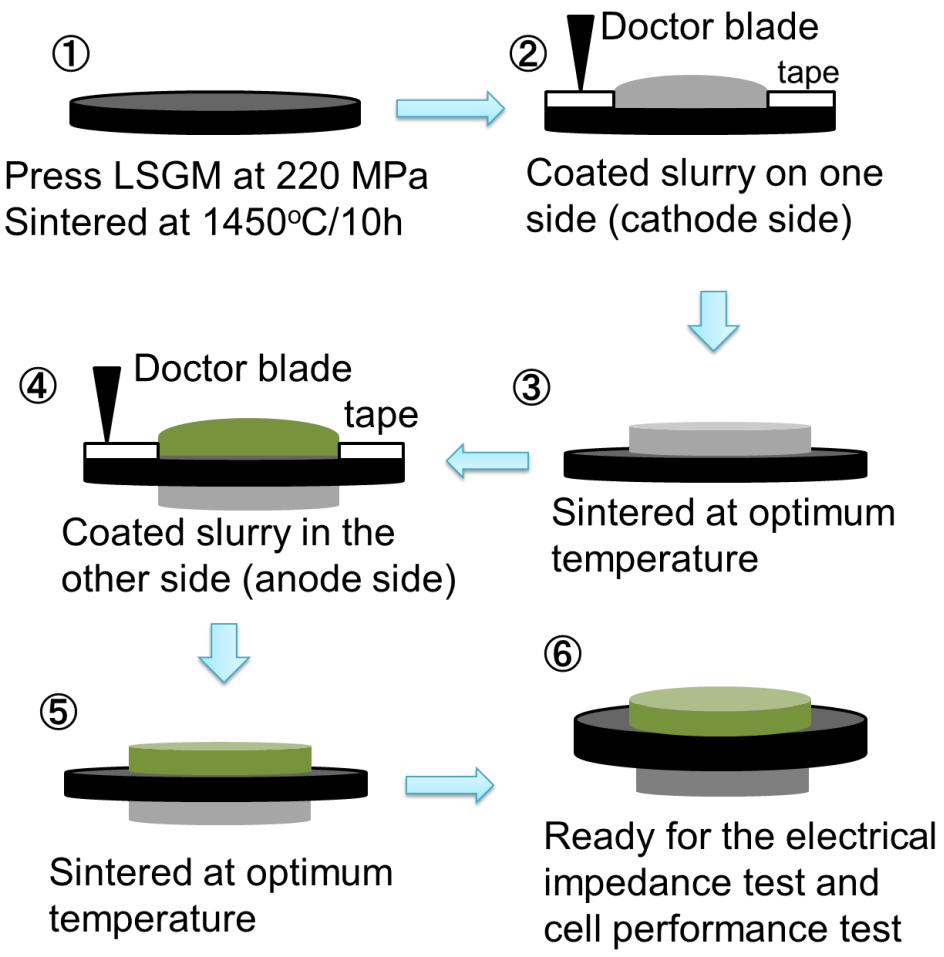

Figure 2.1 Schematic diagram of slurry coating method.

2.2 Characterization techniques

2.2.1 X-ray Diffraction (XRD).

The samples were characterized using XRD (RigakuSmartLab X-Ray Diffractometer) in air using Cu-Kα radiation (λ=0.15405 nm) source within the angular range of $20^{o} \leq 2\theta \leq 80^{o}$ and with scan rate of 5^{o}/min. Lattice parameters of the materials were calculated by POWDERX and PDXL2 Rigaku data analysis Software package using whole pattern

fitting and Rietveld refinement. X-ray diffraction in Bragg-Brentano geometry was used for phase identification, as prepared or obtained samples. X-ray diffraction was also used to define inter phase reactivity between electrolyte and cathode.

2.2.2 Scanning Electron Microscopy (SEM).

Scanning electron microscopy (SEM) was used to analyze surface morphology of sample include cathode powder, cathode bar and electrode-electrolytes. Hitachi SU8000 scanning electron microscope at an acceleration voltage of 15-20.0 kV. The dried sample was put on conductive carbon tape which attached to the specimen stub.

2.2.3 Thermomechanical analyzer (TMA)

Thermomechanical analyzer (TMA，Thermo plus EVO2，Rigaku) was the measurement of a change of a dimension or a mechanical property of the cathode bar while it is subjected to a temperature regime. 20*5*3 mm^3 cathode bar put to measure tray and measurement.

2.2.4 X-ray photoelectron spectroscopy (XPS)

X-ray photoelectron spectroscopy analysis was carried out to study and determine the valence states of the cations in oxide phases. XPS (Kratos AXIS Ultra DLD XPS analyzer) was used for selected samples in this study using Al-Kα radiation as the photon source and generation at 150 W.

2.2.5 Oxygen temperature programmed desorption (O_2-TPD)

Oxygen reduction reaction (ORR) behavior of electrode materials evaluation by oxygen desorption experiments were performed to the surface oxygen desorption behavior by the O_2-TPD catalyst analyzer (Belcat, Bel Japan, Inc). The sample of 0.1 g was placed in a quartz fixed bed microreactor with 8 mm inner diameter. Before each run, the sample was treated in O_2 with a flow rate of 20 cm^3 min^{-1} at 500 ^oC for 1 h, in order to confirm that O2 can be adsorbed and activated completely across the bulk structure of the sample. Then, it followed by cooling to RT in O_2 and argon purging with flow rate of 50 cm^3 min^{-1} for 30 min. the purpose of argon purging was to remove gas phase oxygen in the system. The sample was then heated from RT to 900 ^oC with a heating rate of 10 ^oC min^{-1}. The effluent was monitored by a thermal conductivity detector (TCD).

2.2.6 Electrochemical impedance spectroscopy (EIS)

EIS measurement were performed using a Solarton 1255B Frequency Response Analyzer and a Solarton 1287 Electrical Interface (EI), which act as a potentiostat/galvanostant, in atmospheric condition (air/ wet H_2) over a frequency range from 0.1 Hz to 1 MHz with an AC perturbation of 10 mV and fitted with the commercial program Z-view. Impedance spectroscopy was performed at 700-900 ^oC for single cell test.

2.3 Experimental setup

In this study, as shown in Fig 2.2, the as-prepared cell performances were tested in a Norwegian Electro Ceramics AS (NorECs) SOFC performance testing rig. Pt mesh and wire were used as the current collector, the fuel gases in the anode side were supplied from the inside tube and the oxidant gas was supplied from the outlet tube. A sealant ring (glass ring) was used for sealing. Fig. 2.2 shows the schematic diagram of the SOFC performance testing system used in this study. Pure O_2 was used as the oxidant, and hydrogen or methane was used as fuel. The single cell was tested at 750-900℃ with humidified H_2 as fuel and air/ pure O_2 as oxidant . The level of humidification in H_2 and air were all 3% H_2O and the flow rates of gases were all 50 ml min^{-1}. The cell performances were determined by an electrochemical workstation. The applied frequency range was from 0.10 Hz to kHz.

The base unit is the main part of the ProboStat system; all versions are compatible with all accessories and methods. The sample under test rests on a 50 cm long support tube of alumina, inside a closed outer tube of alumina or silica. A spring-loaded alumina assembly holds the sample and electrodes in place. 16 electrical feedthroughs allow use of 4 shielded electrode leads, surface guard, and up to three thermocouples. Electrical connections are made via coax cables suitable for standard impedance spectrometer connectors, and standard thermocouple compensation cables.

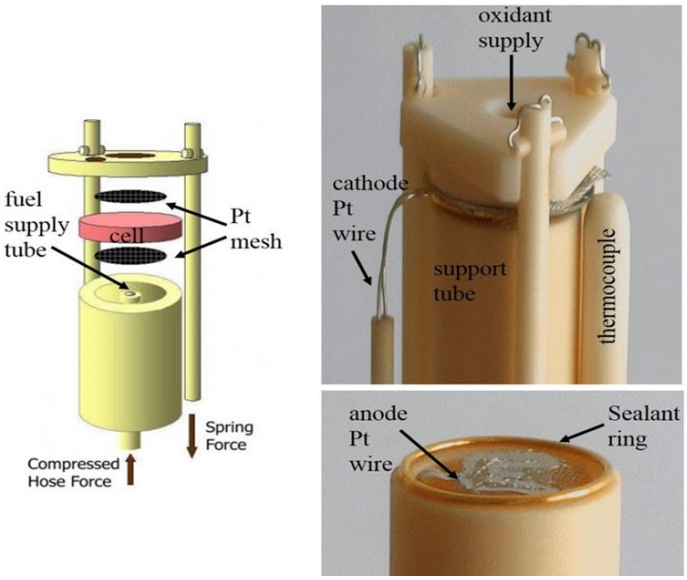

Figure 2.2 Photos for the test ring (Source: norecs.com).

Gases can be fed in single or dual chamber modes directly onto or from electrodes, allowing measurements under controlled atmospheres, transport number measurements in gradients, and testing of fuel cell, pump, and sensor components. Gas supply is via Swagelok quick-connects.

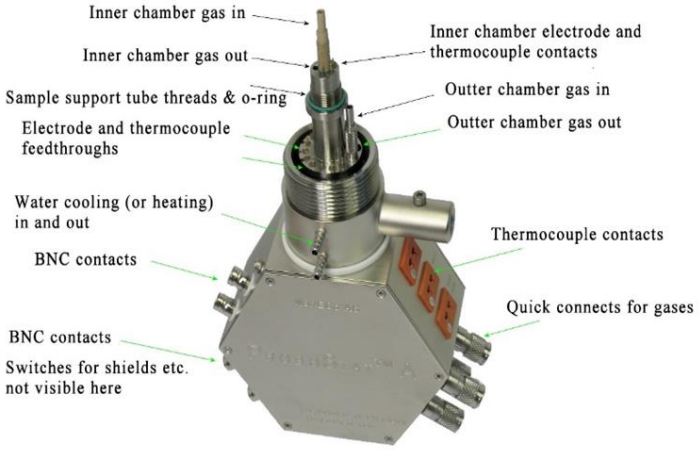

Figure 2.3 ProboStat system of SOFC

Chapter 3 Characterization of B-site Niobium-doped $Pr_{0.4}Sr_{0.6}(Co_{0.3}Fe_{0.6})_{1-x}Nb_xO_{3-\delta}$ (x = 0, 0.05, 0.1 and 0.2) perovskites as cathode materials for solid oxide fuel cells

3.1 Introduction

Environmental pollution and global warming are generally caused by inefficient energy conversion technologies and the excessive applications of fossil fuels, which should be solved in near future. Solid oxide fuel cells (SOFCs) are electrochemical energy conversion devices that possess high energy conversion efficiency.[1-3] Main components of the SOFCs are the anode (for fuel oxidation), the cathode (for oxygen reduction), and the electrolyte (for proton or oxygen anion transportation), plus the interconnect materials. Electrode materials must be porous to allow the fuel to diffuse freely and simultaneously conduct both oxygen anions and electrons. For the electrolyte, a dense layer of ceramics, such as magnesium-doped lanthanum gallium oxide (LSGM), yttria stabilized zirconia (YSZ) and gadolinium doped ceria (GDC), which are enable to conduct oxygen anion well, have been developed. Traditional SOFCs operated at a high temperature around 1000°C always suffer from serious problems, such as materials degradation, short-term stability and high fabrication and operation cost. Therefore, many researchers focused on the improvement of materials for the solid oxide fuel cells.[4, 5]

However, the low operating temperature usually results in worse electrode kinetics and the increase of the polarization loss related to the catalytic activity of the oxygen reduction reaction (ORR) which occurs in the cathode. Oxygen vacancies are oxygen ion transportation channels into the bulk area, and also supply oxygen adsorption, dissociation and diffusion at the cathode surface.[6] Thus, it is important to increase the active reaction area and reduce the polarization resistance. In general, mixed ionic electronic conductor (MIEC) materials could satisfy these requirements since they are good electron and oxygen ion conductors.[7] Among MIEC materials, perovskite (ABO_3) is one of the best candidates as SOFC electrode materials. It is a compound containing various metal ions with convertible oxidation states, which could tolerate appreciable vacancies in the anionic sublattices.[8] For a single cubic structure, A site cation is always 12-coordinated with oxygen ions while B site cation is 6-coordinated with oxygen ions. Also, the materials properties could change with the cation ordering.[9]

In recent years, numerous cobalt-based perovskite materials such as $Ba_{0.5}Sr_{0.5}Co_{0.8}Fe_{0.2}O_{3-\delta}$,[10] $SrCo_{1-y}Nb_yO_{3-\delta}$,[11] $GdBa_{0.5}Sr_{0.5}Co_2O_{5+\delta}$,[12]$PrBa_{0.5}Sr_{0.5}Co_{2-x}Fe_xO_{5+\delta}$[13] and $Pr_{1-x}BaCo_2O_{5+\delta}$ [14] were developed as cathode materials in IT-SOFCs because of their high electro-catalytic activity for the ORR, which attributes to high diffusion of oxygen ions and surface exchange kinetics. However, cobalt-rich cathodes have some disadvantages including high thermal expansion coefficient (TEC), easy evaporation of cobalt

element, and high cost. It is found that thermal expansion mismatch between electrolytes and electrodes always results in cracking or peeling off after sintering.[17] Compared with the cobalt-based cathode materials, cobalt-free or cobalt-less cathode materials have some benefits, such as close thermal expansion with electrolytes and long-term stability although electrochemical activity is partly sacrificed. [15,16] Besides, Fe-based perovskite oxides are particularly competitive candidates due to the low TEC and low price of iron compared to cobalt. Moreover, Fe-Co-based perovskites have much lower TEC than Co-based ones, and meanwhile have higher conductivity than Fe-based perovskites. The catalytic activity of the perovskite is always resulted from its B-site ions[20]. As such, doping elements to the B-site of perovskite could improve the performance. When a higher cation valance element is doped on the B-site, extra positive charge has to be balanced by the reduction of B^{4+} to B^{3+}, which will increase oxygen vacancies and enhance the transformation of the oxygen ions. Based on the previous studies[21,23,41,42,43], various elements such as Pd, Pt, Ag, Cu, Zn, Ni, Mn, Co, Fe, Cr, Ga, Sc, Mn and Mo could serve as the B-site dopants.The doping of these elements with optimum proportions can improve the electronic conductivity, TEC of the material, thereby improving the electrical impedance of the material and enhance materials` ORR and catalytic activity. These investigation results also indicated that doping of the element with a large radius can increase peroviskite free volume to increase the oxygen vacancy.

For example, $PrSrFeCoO_3$ (PSCF) is considered as one of the new-type Fe-Co-based cathode materials, in which Fe cations are in a mixed valence state ranging from +4 to +3, corresponding to a wide range of oxygen nonstoichiometry (from 0 to 0.5). Thus Nb^{5+} doping should obey the charge neutrality criterion since Fe^{4+} can be reduced to Fe^{3+}.[18] Furthermore, its structure alters from cubic to orthorhombic brownmillerite type with long range ordering of oxygen vacancies.[19]

Moreover, more selections for B-site dopants are allowed when compared to A-site doping. In general, iron ions in the B-sites of Fe-Co-based perovskites exhibit higher stability, higher electrochemical activity and more suitable ionic size than cobalt ones. In addition, iron is cheaper and more abundant than cobalt. Meanwhile, other metals coexisted in Fe-Co based perovskite oxides result in the further improvement of the catalytic activity and stability. For example, transition metal doped Fe-Co based perovskite oxides such as $Ln_{1-x}Sr_xCo_{1-y}Fe_yO_{3-\delta}$ (LnSCF, Ln = La, Pr, Sm, and Gd) were found to have high electronic-ionic mixed conductivity and high activity for the cathodic reaction in SOFC.[21] Zhang *et al.* reported that PSCF exhibited the great electrochemical performance after Mo doped, the maximum power density at 850°C was 0.662 Wcm^{-2}.[22] In order to maintain the oxygen vacancy-disordered cubic lattice, various dopants with high-valence such as Zr^{4+}, Ce^{4+}, Nb^{5+} and Mo^{5+} were applied in B-site to stabilize the cubic structure of PSCF at lower operation temperatures.

To date, $Pr_{0.6}Sr_{0.4}(Co_{0.2}Fe_{0.8})_{(1-x)}Sc_xO_{3-\delta}$ (x=0.0-0.2),[21] $Pr_{0.4}Sr_{0.6}(Co_{0.2}Fe_{0.8})_{1-x}Mo_xO_{3-\delta}$ (x=0, 0.05, 0.1 and 0.2),[23] and $(Pr_{0.4})_xSr_{0.6}Co_{0.2}Fe_{0.7}Nb_{0.1}O_{3-\delta}$ ($0.9 \leq x \leq 1.1$)[24] were successfully used as symmetrical electrode materials in SOFCs. Especially, it is found that Nb^{5+} can stabilize the perovskite against reduction,[20] and was doped in various original perovskite cathode materials for not only stabilizing the perovskite cubic structure, but also enhancing the ORR activity of the cathode.[25]

As previously mentioned，Co and Fe are optimum species for occupying the B-site of perovskites and used as cathodes because of their ability to generate oxygen vacancies and high surface exchange kinetics, as well as their high electrical conductivities. However, for perovskite oxides doped with iron only in the perovskite B-site, phase transitions and deep reduction tend to occur under highly reducing anode atmospheres. However, it is found that only cobalt can increase thermal expansion coefficient. One way to improve the phase stability of oxides with iron in the B-site is to introduce a metal ion with higher chemical stability than iron. In this study, the effect of Nb doping at the B site of $Pr_{0.4}Sr_{0.6}(Co_{0.3}Fe_{0.6})_{1-x}Nb_xO_{3-\delta}$ on the performance of the selected perovskite materials of $Pr_{0.4}Sr_{0.6}(Co_{0.3}Fe_{0.6})_{1-x}Nb_xO_{3-\delta}$ (x=0, 0.05, 0.1 and 0.2) as the cathode materials for SOFCs with a LSGM electrolyte were investigated. The crystal phase, chemical reactivity with LSGM electrolyte, morphology of

cathode particles, electrical conductivity, and electrical impedance were also characterized. It is expected to obtain a promising cathode material for SOFCs.

3.2 Experimental and measurements

3.2.1 Sample preparation and cell fabrication

$Pr_{0.4}Sr_{0.6}(Co_{0.3}Fe_{0.6})_{1-x}Nb_xO_{3-\delta}$ ($PSCFN_x$) (x=0, 0.05, 0.1 and 0.2) perovskites were prepared by the solid-state reaction from the oxide, nitrate and carbonate powders with high purity: $Pr(NO_3)_3 \cdot 6H_2O$, $SrCO_3$, $Co(NO_3)_2 \cdot 6H_2O$, Fe_2O_3 and Nb_2O_5 (99.9% Wako, Japan). The stoichiometric amounts of these materials were completely mixed by ball milling for 8 h, and then calcined at 1050°C for 10 h in air to obtain a pure phase. Thereafter, the product was ball milled again for 8 h. For the conductivity test, the finely ground powder was pressed into a bar under a uniaxial pressure of 100 MPa, and the obtained bar was further sintered at 1200°C for 10 h in air with a heating rate of 3°C min^{-1}. The commercially available powder, $La_{0.8}Sr_{0.2}Ga_{0.8}Mg_{0.2}O_{3-\delta}$ (LSGM, 99.9% FCM, USA), was applied for the fabrication of electrolyte. In brief, a dense LSGM pellet with 20 mm in diameter was obtained by pressing the LSGM powder at 220 MPa and then sintered at 1450°C for 10 h in air. The other anode material, NiO-SDC (Samarium-doped cerium oxide ($Sm_{0.2}Ce_{0.8}O_{1.9}$, KOJUNDO CHEMICAL LABORATORY CO., LTD.))

powder, was prepared as reported elsewhere. [22] Symmetrical cells of PSCFN/LSGM/PSCFN for impedance test and single SOFC cell of PSCFN/LSGM/NiO-SDC were prepared by the slurry coating method. That is, for the impedance test, NiO-SDC slurry was coated on the anode side of LSGM electrolyte pellet and 1350°C for 2 h, and then PSCFN slurry was coated onto the cathode side and then sintered at 1250°C for 2 h in air. For a single SOFC cell performance testing, the cell was sealed on an alumina tube using a Pyrex glass ring.

3.2.2 Material characterization

Crystallographic phases of the $PSCFN_x$ powders were characterized using a RIGAKU Smartlab X-ray diffractometer with CuKα radiation (λ=0.154 nm) generated at 45 kV and 200 mA. The conductivity of sintered $PSCFN_x$ bar was determined by the four-terminal DC method, in which the temperature was increased from 100 to 900°C with an interval of 50°C and maintained for 10 min at each temperature before the conductivity was measured in order to make the system equilibrated. The composition and valence of each element on the surface of fresh powder were determined by X-ray photoelectron spectroscopy (XPS, AXIS ULTRA DLD, Japan). The thermal expansion coefficient (TEC) of the Sample were measured between 20 and 800^{o}C using a dilatometer (TMA Instruments, Thermo plus EVO2).

Half-cell and symmetrical cell were fabricated for polarization resistance and cell performance tests, respectively in a temperature range of 750-900°C. A frequency response analyzer and a potentiostat (Solartron 1255B and 1287) were applied for the measurement of electrochemical impedance spectra (EIS) of the half-cell at open circuit voltage (OCV) over the frequency range of 0.01 Hz-1MHz with the AC signal amplitude of 10 mV. The impedance response was analyzed using the equivalent RC circuit method. Before the single SOFC cell performance test, the anode was annealed at 900°C in H_2 for 1 h. Then, the test was performed in a wet H_2 (3% H_2O) flow with a flow rate of 50 cm^3 min^{-1}. Here, air was introduced into the cathode side with a flow rate of 50 cm^3 min^{-1}. Au paste was used to enhance the electronic contact with a Pt mesh. The impedance of the single SOFC cell after the cell performance test was also measured at OCV by the same method.

3.3 Result and discussion

3.3.1 Crystal structure and chemical compatibility

Figure 3.1(a) shows XRD patterns of the synthesized $PSCFN_x$ (x=0, 0.05, 0.1 and 0.2) powders sintered at 1050°C for 10 h. One can see that the peaks for all samples of $x \leq 0.1$ possessed a cubic perovskite phase structure (ABO_3) and in the Pm/3 m phase group. No other peaks were observed, indicating that no additional phases were formed.

Thus, the obtained materials with different Nb doping amounts in this study were of high phase-purity. In contrast, for the sample with x=0.2, the peaks corresponding to the impurity phases defined as strontium ferroniobate and niobium oxides appeared at 2θ=32.7°, 57.2°, 25.4°and 41.0°, respectively, indicating that the excess limit of Nb doping content in $PSCFN_x$ at 1050°C in air should be less or equal than 10%.

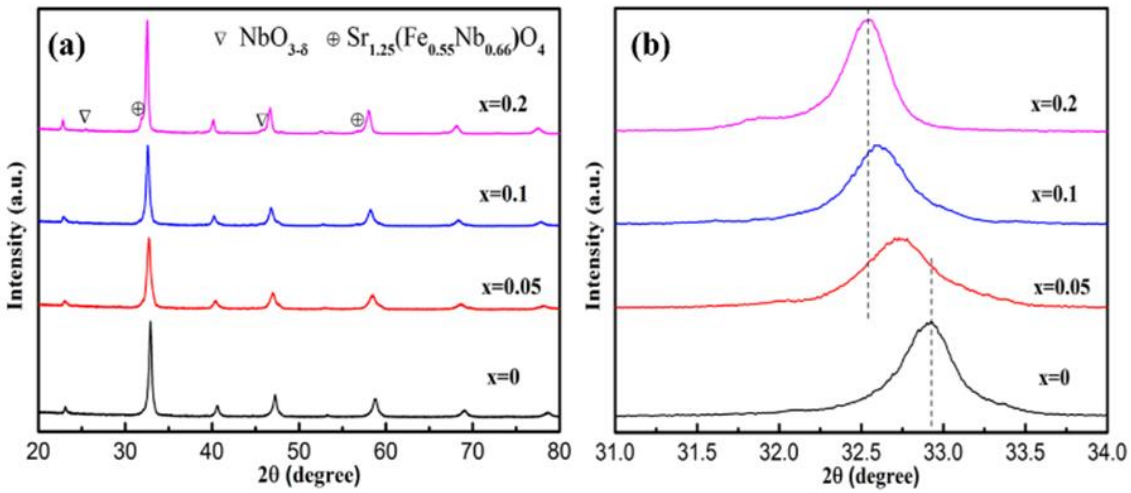

Figure 3.1 (a) X-ray diffraction patterns of $PSCFN_x$(x=0, 0.05, 0.1 and 0.2) sintered in air at 1050°C. (b) Magnified XRD patterns for 31≤2□≤34°. The peak positions of $Sr_{1.25}(Fe_{0.55}Nb_{0.66})O_4$ (PDF: #41-1225) and $NbO_{3-\delta}$(PDF: #35-0789) are taken from database.

From Figure 3.1 (b), the main XRD peak of the $PSCFN_x$ gradually shifted to the lower 2θ direction with the increase in the doping content of Nb(x), indicating the expansion of the perovskite lattice, which confirms that the Nb cations were successfully doped into the lattice of PSCF. Herein, the ionic radius of Nb^{5+} (67 pm) is larger than Fe^{4+}

(58.5 pm) as well as Co^{4+} (53 pm), and meanwhile, the Nb^{5+} doping could reduce the Fe^{4+} and Co^{4+} to Fe^{3+} (64.5 pm) and Co^{3+} (61 pm) respectively in order to maintain the charge balance. [27]

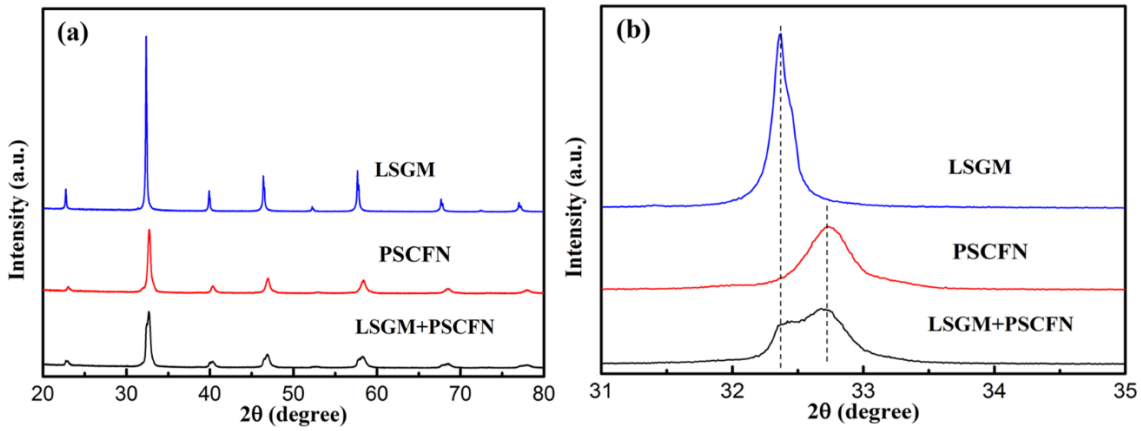

Figure 3.2 (a) PSCFN, LSGM and mixed PSCFN-LSGM powder after calcined at 1050°C for 8 h in air. (b) Magnified XRD patterns for $31 \leq 2\theta \leq 34°$.

To confirm the chemical compatibility of PSCFN and the electrolyte of LSGM, LSGM was mixed with PSCFN in a weight ratio of 1:1, and sintered at 1250°C for 8 h. As shown in Figure 3.2(a), no additional phases were formed in the composite. Also, from Figure 3.2(b), the peaks of PSCFN and LSGM separately appeared in the enlarged XRD pattern. These indicate that no reactions occurred between the cathode and electrolyte. Thus, both materials were chemically compatible during the cathode fabrication.

3.3.2 Electrical conductivity

Figure 3.3(a) shows the changes of electrical conductivity (σ) of $PSCFN_x$ (x=0, 0.05, 0.1 and 0.2) in air with the temperature from 100 to 900°C. One can see that all electrical

conductivities increased at first and then decreased by further increase of temperature over a transition point, which is in accordance with the small polaron hopping mechanism, in which the electron and holes acted as the charge carriers. [22, 27-29]

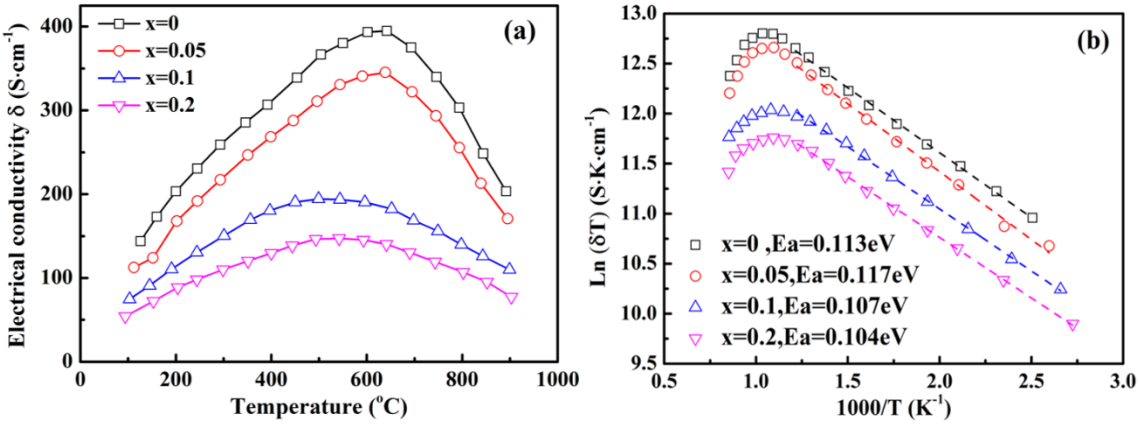

Figure 3.3 (a) Electrical conductivity and (b) corresponding Arrhenius of the PSCFNx(x=0, 0.05, 0.1 and 0.2) bar in air.

This is a thermally activated process at lower temperature where the conductivity increased with the increase in temperature. However, the conductivity decreased at a transition temperature between 500 and 650°C. Here, when the temperature was increased, oxygen was lost from the perovskite, resulting in oxygen vacancies formed in the perovskite structure. As a result, a decoupling of the overlap between the d-orbitals of the transition metal and the p-orbitals of oxygen occurred. That is the reason why the lowered conductivity was obtained at higher temperature. [30] Meanwhile, the Nb doping affected electrical conductivity sensitively and no Nb doping exhibited the highest conductivity value in the tested temperature range and the conductivity decreased with the increase in

the content of Nb doping from 0.05 to 0.2. Although Nb-doping resulted in a decrease in conductivity, the suppression of oxygen vacancies by doping with Nb could recover the transport chains for holes and improve their mobility since B-site was doped with high valence element, which could increase the lattice free volume and result in the decrease in the metal-oxygen average bond energy, and the improvement of the oxygen transport ability. The oxygen vacancies also could be increased by reducing Fe^{4+} to Fe^{3+} as described in the follows:

$$2Fe_{Fe}^{\bullet} + O_{O}^{\times} \rightarrow 2Fe_{Fe}^{\times} + V_{O}^{\bullet\bullet} + \frac{1}{2}O_2 \quad (1)$$

where$Fe_{Fe}^{\bullet}$ represents Fe^{4+}, $O_o^{\times}$ is the lattice oxygen, and $V_o^{\bullet\bullet}$ is the oxygen vacancy. As such, the decreasing of the number of the charge carrier Fe^{4+} may account for the decrease of electrical conductivity by increasing the Nb doping amount. The increase of oxygen vacancies generally improves the ORR rate. From Figure 3.3(b), a linear relationship was observed at low temperature range for each sample. From the slopes of the Arrhenius plots of Ln (σT) at this temperature range can be used for the calculation of activation energy, i.e., Ea value. Based on the mechanism of the small polaron conduction, the relationship of the conductivity σ and temperature T can be expressed by the following equation [31]:

$$\sigma = \frac{C}{T}\exp\left(\frac{-Ea}{kT}\right) \quad (2)$$

Where C is the pre-exponential constant, which is related to the charge carrier content and other material properties; T is temperature; k is the Boltzmann's constant and Ea is the activation energy. Here, the lower Ea indicates higher catalytic activity of ORR. As shown in Figure 3(b), a little amount of Nb doping (x=0.05) resulted in the increase in activation energy, indicating the decrease of the activity. However, with the increase of Nb doping amount, the catalytic activity increased. Here, the Ea values calculated from the slope of the Arrhenius plots (Figure 3.3(b)) were 0.113eV, 0.117eV, and 0.107eV, 0.104eV for PSCF, $PSCFN_{0.05}$, $PSCFN_{0.1}$, and $PSCFN_{0.2}$, respectively.

3.3.3 XPS analysis

XPS was used to characterize the chemical environments of O and Fe ions in the materials. The observed spectra in the O1s and Fe2p regions and their peak separations are shown in Figure 3.4. As shown in Figure 3.4(a) and (b), for PSCF and $PSCF_{0.1}$, the spectra observed in the O1s region were well convoluted into two peaks centered at around 528 eV and 531 eV. In general, the active oxygen locating on the surface (the outermost few monolayers,～2-3nm) and the lattice oxygen locating in the bulk (the following ～4-8nm) are possible to be distinguished by XPS as the former one has the higher binding energy. Therefore, the lower binding energy for the O1s peaks at 528.2eV

and 528.4 eV for PSCF and $PSCFN_{0.1}$ respectively in Figure 3.4(a) were attributed to the lattice oxygen of the perovskite structure[21, 22, 32-34].

Table 3.1. XPS results of O1s at the surface of materials.

Cathode materials	**O1s**	
	Binding energy(eV)	Percent in total oxygen (%)
PSCF	531.1	79.8
	528.2	20.2
$PSCFN_{0.1}$	531.4	84.9
	528.4	15.1

The small shift from 528.2 eV to 528.4 eV should be resulted from environmental difference of the O atoms. On the other hand, the higher binding energies for the O1s peaks at 531.1 eV and 531.4 eV for PSCF and $PSCFN_{0.1}$ respectively should be attributed to the active oxygen locating on the surface, which correspond to the chemisorbed oxygen in the forms of O_2^{2-} and O^-.

The absorbed oxygen states on the surface in transition metal oxide are also related to the amount of oxygen vacancies.[32] The percentage of the area of the surface species to the total area can indicate the relative concentration of oxygen vacancy in the material. As shown in Table 3.1, the ratio of active oxygen in $PSCFN_{0.1}$ (84.9%) was higher than

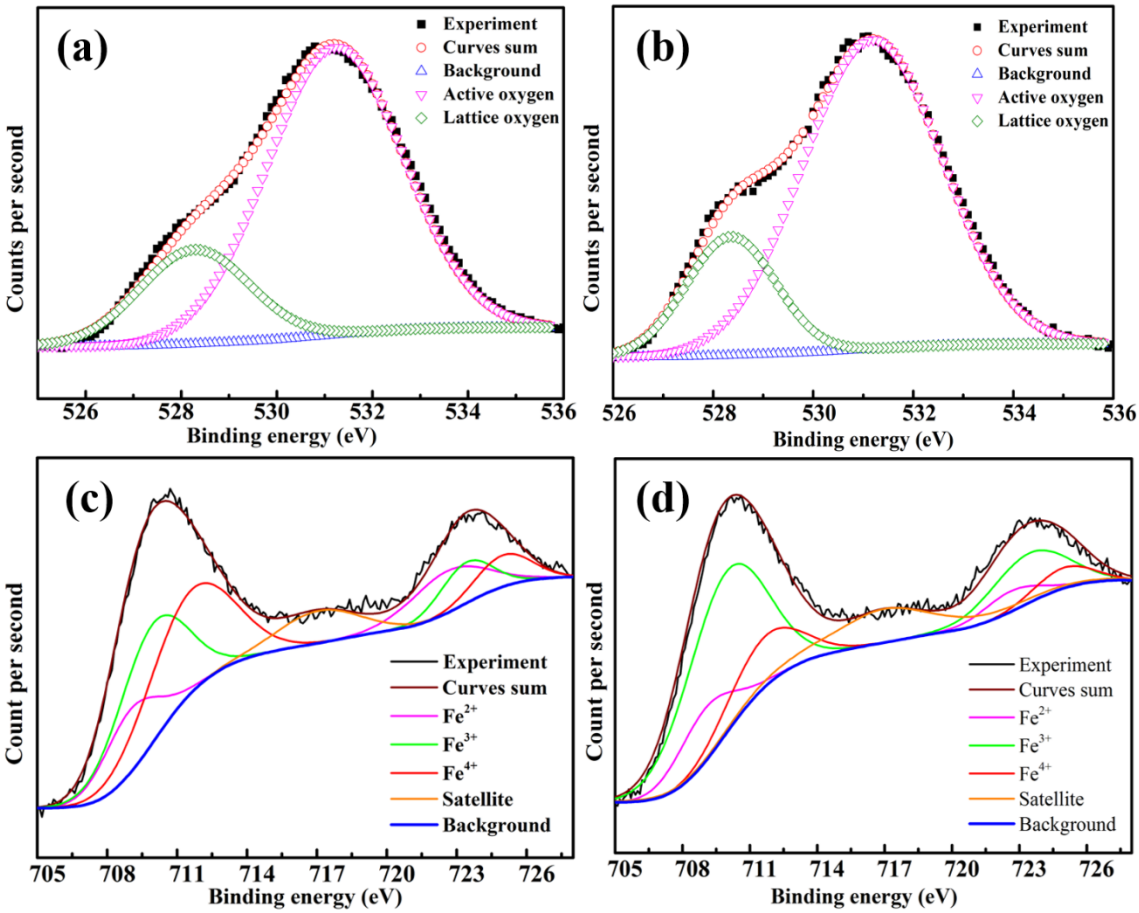

Figure 3.4 XPS spectra of (a, b) O1s and (c, d) Fe2p transitions for (a, c) PSCF and (b, d) $PSCFN_{0.1}$.

that in PSCF (79.8%), indicating a higher concentration of oxygen vacancy existed in surface of $PSCFN_{0.1}$ than that in PSCF.[35]This also explained that the electrical impedance spectra of $PSCFN_{0.1}$ was smaller than that of PSCF shown in the next section, in which the polarization included charge transfer ,adsorption-dissociation of oxygen, transport rate of oxide ion through the bulk cathode, and across the cathode-electrolyte interface. Hence, the concentration of the high oxygen ion vacancy on the surface of material could enhance the rate of oxygen exchange. Meanwhile, in the region of Fe2p3/2,

the observed spectra for both PSCF and $PSCFN_{0.1}$ were separated into three peaks. It is reported that the binding energy of Fe^{3+} species in the oxide materials was 711.0 eV [36] while that of Fe^{4+} species in the perovskite materials were observed in the range of 712-714 eV for the Fe2p3/2 transition. Therefore, the three peaks observed for PSCF and $PSCFN_{0.1}$ should be attributed to Fe^{2+}, Fe^{3+} and Fe^{4+} in the order of lower to higher binding energies. [22] As shown in Figure 3.4(c) and (d), the concentration of Fe^{4+} decreased and Fe^{3+} increased by Nb doping, indicating that the doping of high valence Nb^{5+} reduced the Fe^{4+} to Fe^{3+} for maintaining electro neutrality.

3.3.4 Thermal expansion behavior

In general, TECs of the electrodes and electrolyte should be well match in order to ensure a long-term operational stability. Less differences of TECs between the electrodes and electrolyte could avoid the degradation of cell performance. Figure 3.5 shows the measured thermal expansion curves of PSCFNx (x=0, 0.05, 0.1 and 0.2) cathode materials and LSGM in the temperature range of 100-800oC in air. Based on these measurements, Table 3.2 summaries the average TECs of PSCFNx, LSGM and Figure 3.5 Thermal expansion curves of cathode materials PSCFNx (x=0, 0.05, 0.1 and 0.2) temperature range of 100-800oC in air.

Compared with the reported data on Co-based materials. One can see that the TEC of PSCFNx. decreases with doping of Nb, and the Fe-Co based perovskites have smaller TEC than Co-based perovskites. Therefore, the Fe-Co based perovskite is more beneficial in terms of TEC since the Fe-Co based perovskites has a closer TEC to that of LSGM than Co-based perovskite.

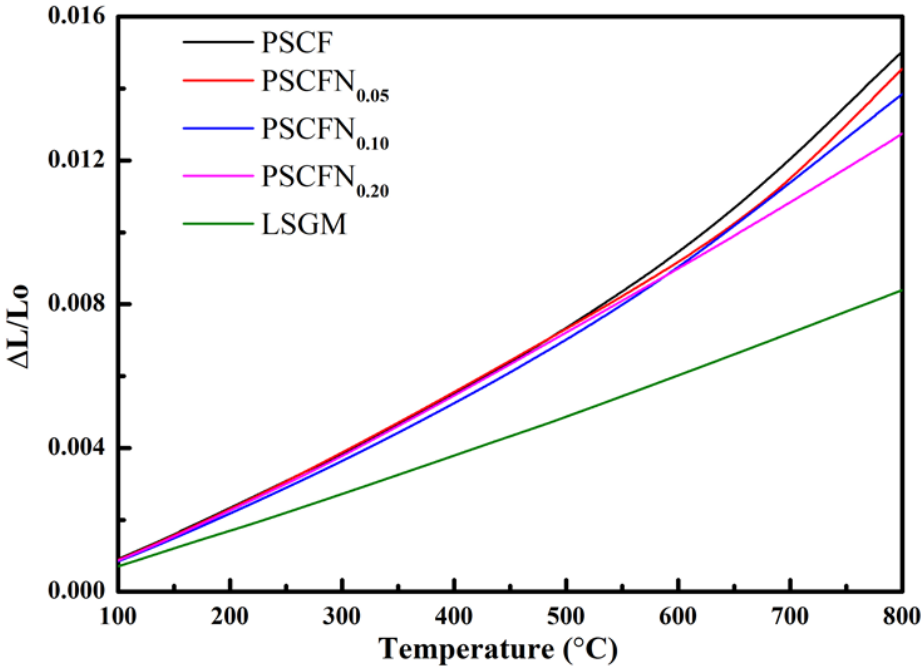

Figure 3.5 Thermal expansion curves of cathode materials PSCFNx (x=0, 0.05, 0.1 and 0.2) temperature range of 100-800oC in air.

Table 3.2 Measured average TEC values and compared with the reported data

Sample	TEC($\times 10^{-6}K^{-1}$)
PSCF	15.29
$PSCFN_{0.05}$	14.73
$PSCFN_{0.1}$	14.17

$PSCFN_{0.2}$	13.64
LSGM	10.01
$LaBaCo_2O_{5+\delta}$[37]	24.30
$SrCo_{0.9}Sb_{0.1}O_{3-\delta}$[38]	22.82
$SrCo_{0.8}Nb_{0.2}O_{3-\delta}$[39]	24.90

3.3.5 Impedance analysis

Electrochemical impedance spectroscopies (EIS) of the PSCFNx/LSGM/PSCFNx symmetrical cells with a thickness of LSGM electrolyte of 500 μm at different temperatures are displayed in Figure 3.6 Here, the Ohmic resistance was set at zero and the impedance response had strong relationship with the oxygen reduction. The EIS behavior was fitted by an equivalent circuit which is determined by two separable arcs over the whole frequency range in the Nyquist plot. The intercept with the real axis at high frequency represents the resistance of the electrolyte whereas the diameter of the depressed semicircle corresponds to the impedances of the two interfaces, i.e., the cathode-electrolyte interface (Rc) and the anode electrolyte interface (Ra). The interfacial resistance contains the contact resistance between the electrode and the electrolyte and other resistances related to the electrochemical processes such as charge transfer and mass transfer, but the anode-electrolyte interfacial impedance can be negligible. [37]

The difference of intercepts with the real axis between high and low frequency arcs corresponded to the polarization resistance of the cathode/electrolyte interface. [38] Here, two arcs appeared with different behavior plots as a function of temperature. The high frequency (10^3-10^2 Hz) arc (R_{HF}) is usually related to the charge-transfer resistance, while the low frequency (10^1-10^{-1} Hz) arc (R_{LF}) to the mass-transfer. Moreover, it is reported that the surface diffusion of oxygen specimen including the oxygen adsorption and dissociation processes can be represented by R_{LF}.[39] As such, the total polarization resistance (R_p) can be evaluated from the sum of R_{HF} and R_{LF}. As shown in Figure 3.6, with the increase in temperature, the impedance resistances of all samples decreased, which can be attributed to the enhanced catalytic activity at higher temperature.

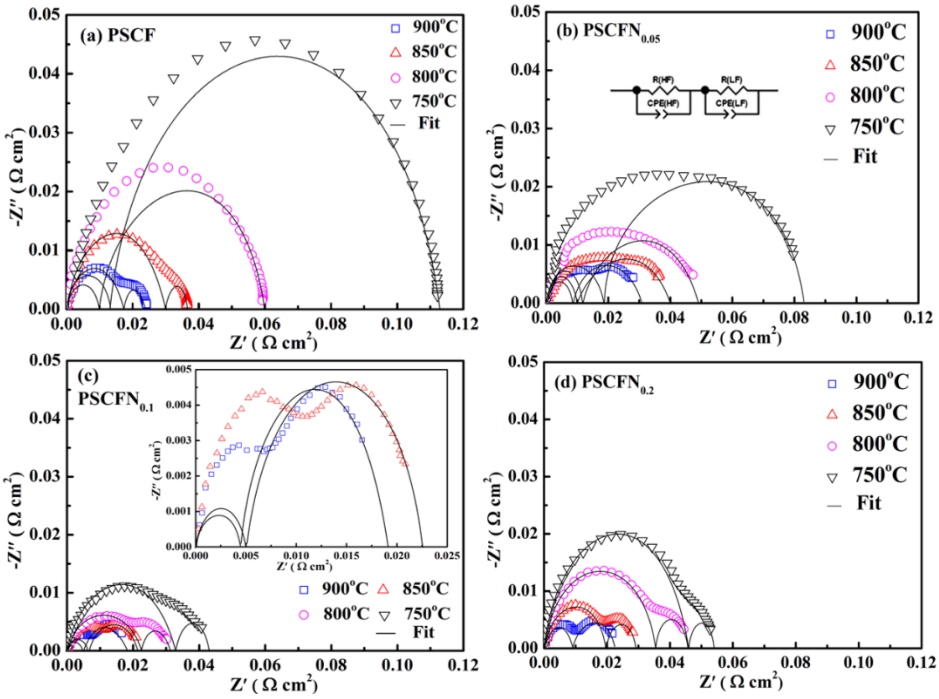

Figure 3.6 Nyquist plots of impedance spectra for (a) PSCF, (b) $PSCFN_{0.05}$, (c) $PSCFN_{0.1}$

and (d) $PSCFN_{0.2}$

Figure 3.7 shows Arrhenius plots based on the total polarization resistance (Rp) values obtained from the data in Figure 3.6(a-d). One can see that the activation energy of cathode decreased after Nb doping. This indicates that the doping of Nb into PSCF cathode extended the electrochemical three phase boundaries (TPB) and increased active sites effectively.[39] As shown in Table 3.3, the Rp values of PSCF, $PSCFN_{0.05}$, $PSCFN_{0.1}$ and $PSCFN_{0.2}$ were 0.024, 0.030, 0.018 and 0.023 Ωcm^2 at 900°C, respectively

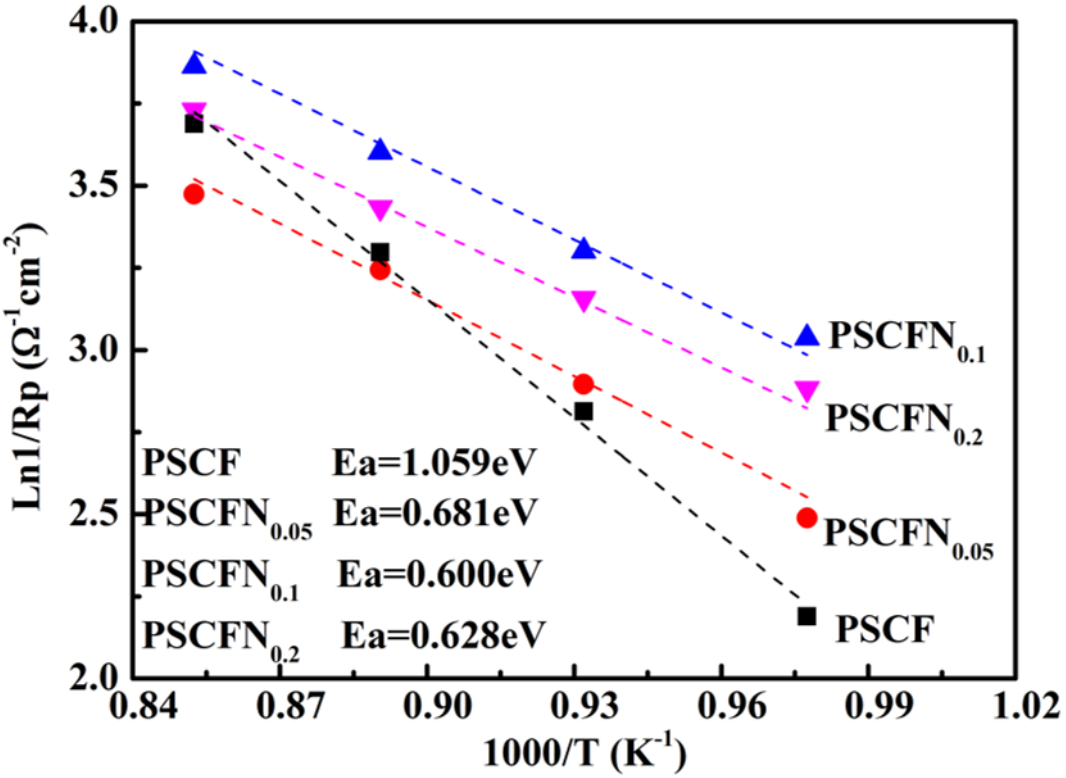

Figure 3.7 Comparison of Arrhenius plots of polarization resistance for PSCF, $PSCFN_{0.05}$, $PSCFN_{0.1}$ and $PSCFN_{0.2}$ at 750, 800,850 and 900°C.

Among all the cathodes, $PSCFN_{0.1}$ demonstrated the lowest Rp values at all testing temperatures. The polarization resistance of the $PSCFN_{0.1}$ cell decreased by about 25% as compared with that of PSCF, indicating that the Nb doping enhanced the transfer rate of oxygen anions and promoted the activity of cathode by the interaction with oxygen molecules on the surface without influencing porous structure of cathodes which facilitates oxygen transfer. [39] Also, the Arrhenius plots of polarization impedance shown in Figure 3.7 indicated the distinct decrease of the activation energy by doping Nb on PSCF. Furthermore, it is found that the polarization resistance of $PSCFN_{0.1}$ decreased 25% at 900°C but 61% at 750°C, indicating that the performance enhancement by Nb doping was more effective at lower temperatures because of its higher catalytic activity. Generally, the average bond between metal and oxygen can be reduced since Nb has larger radius, which could result in the increase oxygen transport rate. Also, the doping of Nb could increase the crystal lattice free volume, thus increase oxygen transport capacity with the increase of the doping amount. Moreover, as stated above, the doping of Nb into PSCF cathode could extend the electrochemical three phase boundaries (TPB) and increased active sites effectively. However, the doping amount should have an optimum value, if the doping amount is increased over this value, the lattice structure could be changed or some impurity phase will be generated. In this study, it is found that

Nb=0.1 is just the optimum value, and in this case, the material exhibited a high ionic transport kinetics with the minimum Rp. When Nb doping amount is over 0.1, for example, as x=0.2, the impurity is generated as shown in the XRD analysis results (Figure 3.1). Here, although $PSCFN_{0.2}$ had some impurity phase, the main perovskite components should still have high oxygen transfer capacity due to much more Nb doping in it than that in $PSCFN_{0.05}$. Meanwhile, from Arrhenius plots of the conductivity and polarization resistance results, it can be also concluded that $PSCFN_{0.2}$ has higher catalytic activity than $PSCFN_{0.05}$.

Table 3.3 summarizes the fitting results of the high- and low-frequency polarization resistances based on Figure 3.6. For $PSCFN_{0.1}$, the value of R_{HF} was much lower than that of R_{LF}, as also shown in Figure 3.6(c), in which there was an obvious difference between high- and low-frequency arcs, $PSCFN_{0.1}$ had high oxygen vacancy content for bulk oxygen ion transfer and enough catalytic activity for the oxygen activation on the surface. Also, the R_{HF} value of the $PSCFN_{0.05}$ cathode at high temperature range, from 900 to 850°C, was significantly lower than R_{LF} value. In contrast, at the low temperature range from 800 to 750°C, the RHF value became significantly higher than R_{LF} value. For the PSCF cathode, it had an opposing behavior from $PSCFN_{0.05}$.Here, $PSCFN_{0.05}$ demonstrated the lowest R_{HF} contribution to the total polarization resistance (~20-27%);

and in contrast, the R_{HF} contribution to the $PSCFN_{0.1}$ cathode at high temperature (900-850°C) was ~22-23% but reached ~74-77% at low temperature (800-750°C). It indicates that Nb doping in PSCF enhanced the transfer of oxygen anions via the increase of the total oxygen vacancies. Thus, the ORR can take place at much more TPBs. As a result, the whole oxygen diffusion in the SOFC could be enhanced by the diffusion of more oxygen anions into the LSGM electrolyte.

Table 3.3 High-and low-frequency polarization resistances in air at temperature range of 750-900°C

Cathode	Temperature	$R_P(\Omega\ cm^2)$	$R_{HF}(\Omega\ cm^2)$	$R_{LF}(\Omega\ cm^2)$
PSCF	900	0.024	0.017	0.007
	850	0.037	0.031	0.006
	800	0.059	0.009	0.049
	750	0.111	0.015	0.096
$PSCFN_{0.05}$	900	0.030	0.008	0.022
	850	0.040	0.010	0.030
	800	0.048	0.012	0.036
	750	0.084	0.017	0.067
$PSCFN_{0.1}$	900	0.018	0.004	0.014
	850	0.022	0.005	0.017
	800	0.031	0.023	0.008
	750	0.043	0.033	0.010
$PSCFN_{0.2}$	900	0.023	0.008	0.015
	850	0.029	0.020	0.009
	800	0.044	0.035	0.009
	750	0.054	0.044	0.100

3.3.6 Cell performance

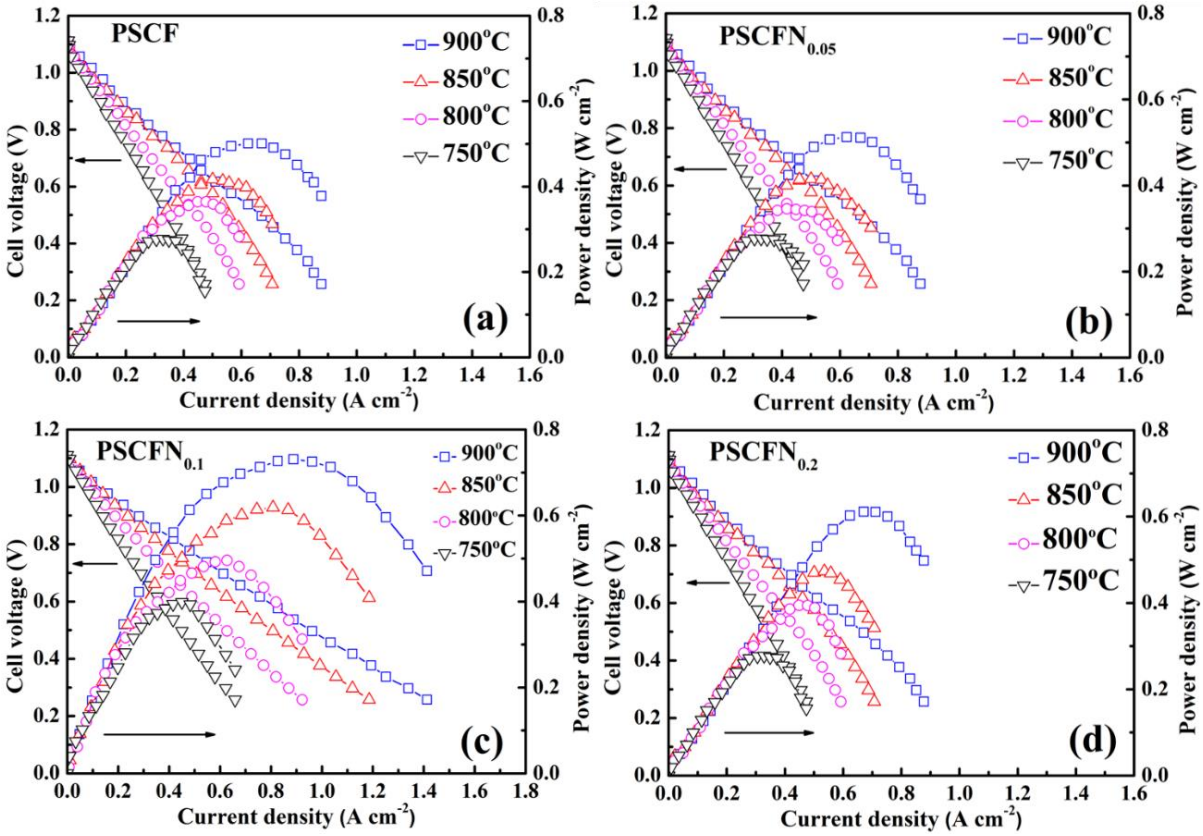

Figure 3.8 I-V curves and corresponding power density curves of the single cells (PSCFNx/LSGM/NiO-SDC) under various temperatures: (a) x =0, (b) x = 0.05, (c) x = 0.1 and (d) x = 0.2

Figure 3.8 shows the current-potential (I-V) characteristics of LSGM electrolyte supported SOFCs with PSCF, $PSCFN_{0.05}$, $PSCFN_{0.1}$ and $PSCFN_{0.2}$ as the cathodes. Here, the performance tests were conducted at different temperatures (750-900°C) with humidified H_2 (~3%H_2O) as a fuel and oxygenas an oxidant. It can be seen that the power density increased with the increasing of the operating temperature for all single cells. All

open-circuit voltages (OCVs) were approximately 1.1 V at 900°C and increased with the decrease in operating temperature.

For the cells using PSCF, $PSCFN_{0.05}$, $PSCFN_{0.1}$ and $PSCFN_{0.2}$ as the electrodes, the maximum power densities reached 0.501, 0.513, 0.731 and 0.611 Wcm^{-2} at 900°C, respectively. As shown in Figure 3.8, when x was less than 0.1, the electrode performance was enhanced by the increasing of the doping content; however, when x was further increased to 0.2, the power density decreased to some extent at each operating temperature. When x was 0.1, the maximum power densities of 0.618, 0.495, and 0.369 Wcm^{-2} were achieved at 850, 800 and 750°C, respectively. However, when x was increased to 0.2, these values were reduced to 0.474, 0.394 and 0.277 Wcm^{-2}, respectively. As indicated in Figure 3.8(a), (b) and (c), with the increasing of the operation temperature, the cell performance was improved more obviously in the case of more Nb doping. It is found that P_{max} was increased from 0.276 to 0.501 W cm^{-2} at x=0 and from 0.369 to 0.731 Wcm^{-2} at x=0.1 when the operation temperature was increased from 750 to 900°C. It indicates that the maximum power density for $PSCFN_{0.1}$ based cell was increased 46% when compared with that without Nb doping. However, as shown in Figure 3.8(d), as x was increased to 0.2, the P_{max} decreased to some extent, but when compared with that without Nb doping, the power density was still increased 22%. As shown in Figure 3.1(a),

$PSCFN_{0.2}$ contained some impurity phase. However, it is also found that the main peak shifted to lower 2θ. It indicates that the perovskite lattice was expanded since the larger radius of Nb^{5+} led to the reduction of metal-oxygen average bond in the main component. As such, the oxygen transfer capacity could be also increased. Meanwhile, from Arrhenius plots of the conductivity and polarization resistance result, it can be also concluded that $PSCFN_{0.2}$ had higher catalytic activity than $PSCFN_{0.05}$, thus in the case of $PSCFN_{0.2}$, higher power density was obtained when compared with that using $PSCFN_{0.05}$ at 900°C.

3.3.7 Stability test

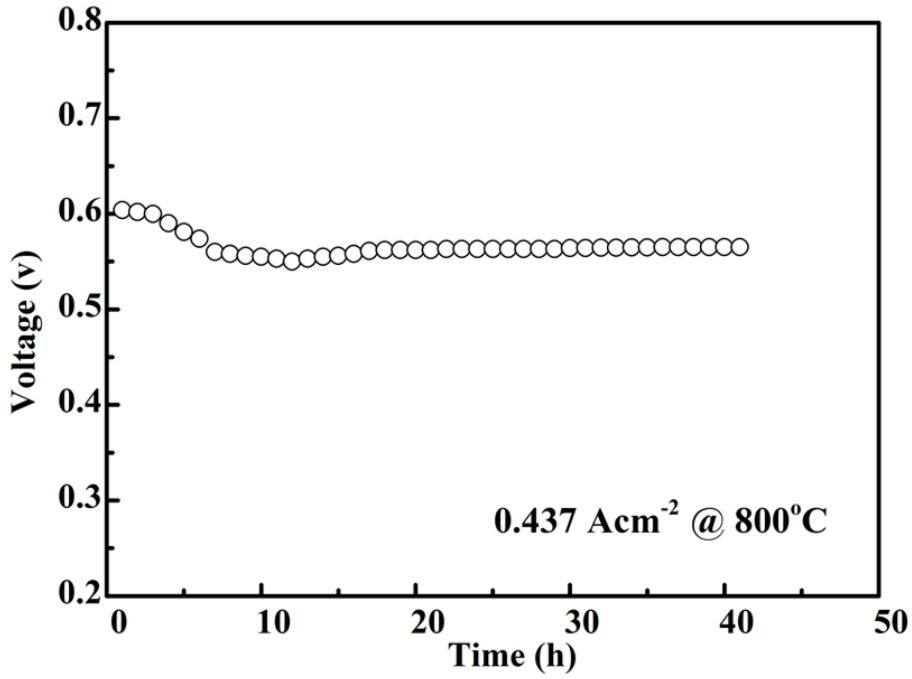

Figure 3.9 Stability test of PSCFN0.1/LSGM/NiO-SDC, measured at 800°C with wet H_2 as fuel and air as oxidant.

Stability test was performed under wet H_2 at 800°C with $PSCFN_{0.1}$ as cathode and LSGM as the supported layer, in which a 50 cm^3 min^{-1} wet H_2 flow at anode side and 50 cm^3 min^{-1} air flow at cathode side were applied. As shown in Figure 3.9, despite the decline in the first 13 h, which probably due to the activating process, the current density at an output voltage of 0.56 V decreased only about 8% in 40 h test.

3.3.8 Cell microstructure

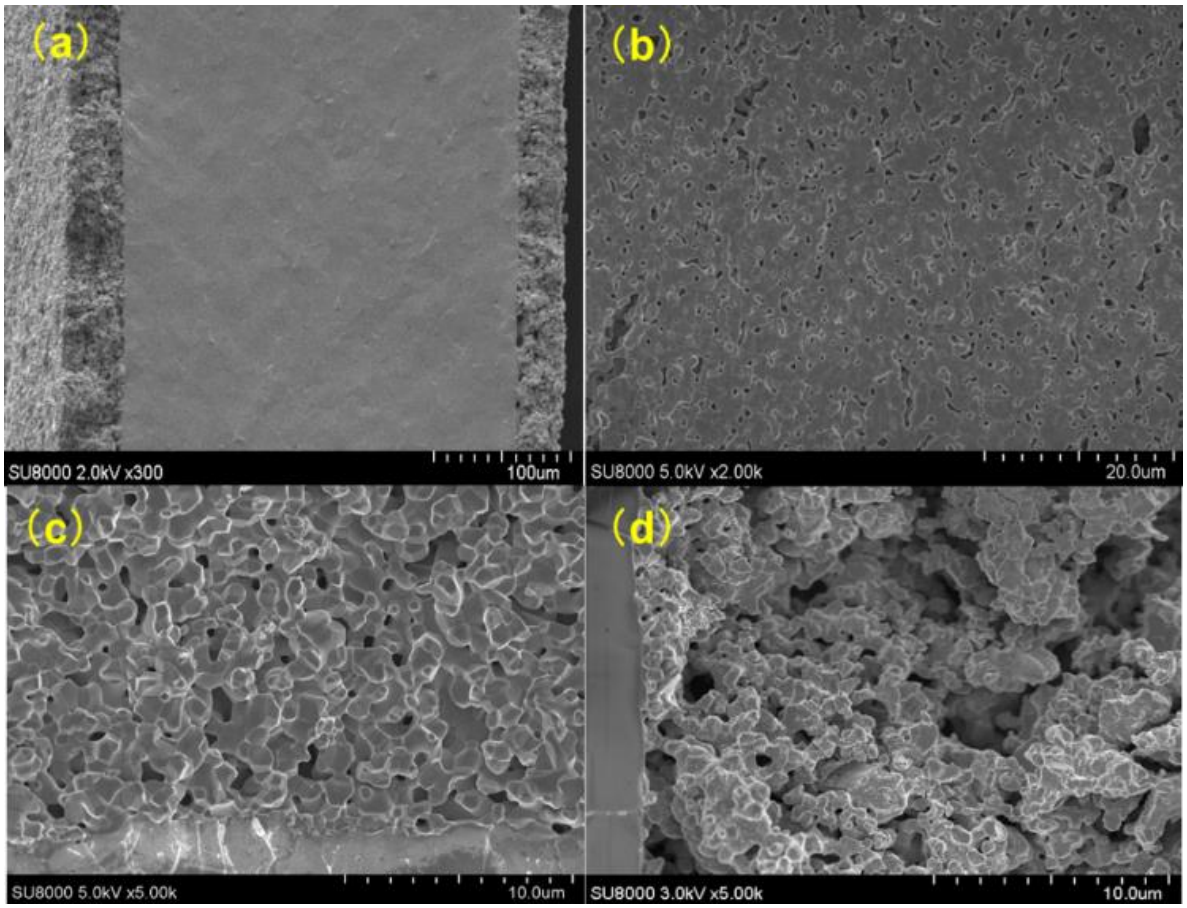

Figure 3.10 SEM images of (a) cell cross section of PSCFNx/LSGM/NiO-SDC, (b) single cell cathode side surface section, (c) cell section of PSCFNx/LSGM and (d) cell cross section of LSGM/NiO-SDC

The morphologies of $PSCFN_x$ cathodes after the cell performance test are shown in Figure 3.10(a). One can see that no obvious delamination and cracks were observed at the PSCFN/LSGM interface, indicating that PSCFN and LSGM had good compatibility. Figure 3.10(b) shows the surface of cathode side after the cell performance test. It is obvious that the surface still had homogeneous porous structure without any crack or delamination, indicating that the microstructure was stable during the performance test. From Figure 3.10(c) and (d), either the anode or cathode had a highly porous structure for the gas diffusion as well as good connect with the electrolyte. These results reveal that the PSCFN perovskite material should be a promising cathode material for IT-SOFCs.

3.4 Conclusions

A potential cathode material family of $PSCFN_x$ (x=0, 0.05, 0.1 and 0.2) for SOFC was obtained by the solid state reaction method. It is found that a pure cubic perovskite phase was formed after calcination at 1050°C in air for the samples with x=0, 0.05 and 0.1. However, impurity phases defined as strontium ferroniobate and niobium oxide were formed as x=0.2. The conductivity decreased with the increasing of Nb content, and the conductivity values at 800°C were 303.1, 259.6, 119.8 and 106.9 Ωcm^2 when x=0, 0.05, 0.1 and 0.2, respectively. It is found that the power density increased with the doping of Nb, and especially the maximum power density of a single SOFC with a $PSCFN_{0.1}$

cathode reached 0.731 Wcm^{-2} at 900°C in wet H_2, indicating that the $PSCFN_{0.1}$ should be a promising electrode for SOFCs.

References

[1] N. Q. Minh, Ceramic fuel cells, J. Am. Ceram. Soc. 76 (1993) 563–588.

[2] B. C. H. Steele， A. Heinzel, Materials for fuel-cell technologies, Nature 41 (2001) 345-352.

[3] S. C. Singhal, K. Kendall, High Temperature Solid Oxide Fuel Cells, Elsevier, 2003.

[4] C. Xia, M. Liu, Novel cathodes for low-tempearture solid oxide fuel cells, Adv. Mater. 14 (2002) 521–523.

[5] Z. Shi, W. Sun, Z. Wang, J. Qian, W. Liu, Samarium and yttrium codoped $BaCeO_3$ proton conductor with improved sinterability and higher electrical conductivity, Appl. Mater. Inter. 6 (2014) 5175–5182.

[6] S. Huang, F. Gao, Z. Meng, S. Feng, X. Sun, Y. Li, C. Wang, Bismuth‐Based Perovskite as a High‐Performance Cathode for Intermediate‐Temperature Solid‐Oxide Fuel Cells, ChemElectroChem,1 (2014) 554 – 558.

[7] J. Nielsen, J. Hjelm, Impedance of SOFC electrodes: A review and a comprehensive case study on the impedance of LSM:YSZ cathodes, Electrochim. Acta 115 (2014) 31– 45.

[8] J. Meng, N. Yuan, X.Liu, C. Yao, F. Meng, X. Niu, X. Wua, J. Meng, Assessment of $LaM_{0.25}Mn_{0.75}O_{3-\delta}$ (M = Fe, Co, Ni, Cu) as promising cathode materials for intermediate-temperature solid oxide fuel cells , Electrochim. Acta 169 (2015) 264–275

[9] A. Jun, J. Kim, J. Shin, G. Kim, Perovskite as a Cathode Material: A Review of its Role in Solid‐Oxide Fuel Cell Technology，ChemElectroChem 3（2016) 511-530.

[10] Z. Shao, S. M. Haile, A high-performance cathodes for the next generation of solid oxide fuel cells, Nature 431 (2004) 170-173.

[11] F. Wang, Q. Zhou, T. He, G. Li , H. Ding, Novel $SrCo_{1-y}Nb_yO_{3-\delta}$ cathodes for Intermediate temperature solid oxide fuel cells, J. Power Sources195 (2010) 3772–3778.

[12] J. Kim, A. Jun, J. Shin, G. Kim, Effect of Fe doping on layered $GdBa_{0.5}Sr_{0.5}Co_2O_{5+\delta}$ perovskite cathodes for intermediate temperature solid oxide fuel cells, J. Am. Ceram. Soc. 97 (2014) 651–656.

[13] S. Choi, S. Yoo, J. Kim, S. Park, A. Jun, S. Sengodan, J. Kim, J. Shin, H. Y. Jeong, Y.M. Choi, G. Kim， M. Liu, Highly efficient and robust cathode materials for low-temperature solid oxide fuel cells: $PrBa_{0.5}Sr_{0.5}Co_{2-x}Fe_xO_{5+\delta}$, Sci. Rep. 3 (2013) 1–6.

[14] L. Zhang, G. Yao, Z. Song, B. Niu, W. Long, L. Zhang,Y. shen, T.He, Effects of Pr-deficiency on thermal expansion and electrochemical properties in $Pr_{1-x}BaCo_2O_{5+\delta}$ cathodes for IT-SOFCs, Electrochimica Acta 212 (2016) 522–534

[15] L. Li, F. Jin, Y. Shen, T. He, Cobalt-free double perovskite cathode $GdBaFeNiO_{5+\delta}$ and electrochemical performance improvement by $Ce_{0.8}Sm_{0.2}O_{1.9}$ impregnation for intermediate-temperature solid oxide fuel cells, Electrochimica Acta 182 (2015) 682–692.

[16] A. Mai, V. A.C. Haanappel, F. Tietz, D. Stöver, Ferrite-based perovskites as cathode materials for anode-supported solid oxide fuel cells. Part II. Influence of the CGO interlayer, Solid State Ion. 177 (2006) 2103-2107.

[17] A. Mai, V. A.C. Haanappel, F. Tietz, D. Stöver, Ferrite-based perovskites as cathode materials for anode-supported solid oxide fuel cells. Part II. Influence of the CGO interlayer, Solid State Ion. 177 (2006) 2103-2107.

[18] F. Liang, Z. Wang, Z. Wang, J. Mao, J. Sunarso, Electrochemical Performance of Cobalt‐Free Nb and Ta Co‐Doped Perovskite Cathodes for Intermediate‐Temperature Solid Oxide Fuel Cells, ChemElectroChem 4 (2017) 2366-2372.

[19] P.K. Patro, T. Delahaye, E. Bouyer, Development of $Pr_{0.58}Sr_{0.4}Fe_{0.8}Co_{0.2}O_{3-\delta}$-GDC composite cathode for solid oxide fuel cell (SOFC) application, Solid State Ion. 181 (2010) 1378–1386.

[20] F. Dong, Y. Chen, R. Ran, D. Chen, M.O. Tadé, S. Liub, Z. Shao, $BaNb_{0.05}Fe_{0.95}O_{3-\delta}$ as a new oxygen reduction electrocatalyst for intermediate temperature solid oxide fuel cells, J. Mater. Chem. A 1(2013) 9781-9791.

[21] Y.M. Yin, M.W. Xiong, N.T. Yang, Z. Tong, Y.Q. Guo, Z.F. Ma, E. Sun, J. Yamanis, B.Y. Jing, Investigation on thermal, electrical, and electrochemical properties of scandium-doped

$Pr_{0.6}Sr_{0.4}(Co_{0.2}Fe_{0.8})_{(1-x)}Sc_xO_{3-\delta}$ as cathode for IT-SOFC, Int. J. Hydrogen Energy 36 (2011) 3989-3996.

[22] P. Zhang, G. Guan, D.S. Khaerudini, X. Hao, C. Xue, M. Han, Y. Kasai, A. Abudula, Mo doped $Pr_{0.4}Sr_{0.6}Co_{0.2}Fe_{0.8}O_{3-\delta}$ cathode material with high catalytic activity for intermediate-temperature solid oxide fuel cells, Electrochimica Acta 146 (2014) 591–597.

[23] P. Zhang, G. Guan, D.S. Khaerudini, X. Hao , C. Xue, M. Han , Y. Kasai , A. Abudula, B-site Mo-doped perovskite $Pr_{0.4}Sr_{0.6}$ $(Co_{0.2}Fe_{0.8})_{1-x}Mo_xO_{3-\delta}$ (x=0,0.05, 0.1 and 0.2) as electrode for symmetrical solid oxide fuel cell, J. Power Sources 276 (2015) 347-356.

[24] P. Zhang, G. Guan, D.S. Khaerudini, X. Hao , M. Han, Y. Kasai, K. Sasagawa, A. Abudula, Properties of A-site nonstoichiometry $(Pr_{0.4})_xSr_{0.6}Co_{0.2}Fe_{0.7}Nb_{0.1}O_{3-\delta}$ ($0.9 \leq x \leq 1.1$) as symmetrical electrode material for solid oxide fuel cells, J. Power Sources 248 (2014) 163-171.

[25] M. Li, W. Zhou, Z. Zhu, Comparative Studies of $SrCo_{1-x}Ta_xO_{3-\delta}$ (x=0.05–0.4) Oxides as Cathodes for Low‐Temperature Solid‐Oxide Fuel Cells, ChemElectroChem 2 (2015) 1331 – 1338.

[26] G. Chen, H. You, Y. Kasai, H. Sato, A. Abudula, “Characterization of planer cathode-supported SOFC prepared by a dual dry pressing method,” J. Alloys Compds., 16 (2011)5159-5162.

[27] Q. Liu, D. E. Bugaris, G. Xiao, M. Chmara, S. Ma, H. C. Loye, M.D. Amiridis, F. Chen, $Sr_2Fe_{1.5}Mo_{0.5}O_{6-\delta}$ as a regenerative anode for solid oxide fuel cells, J. Power Sources 196 (2011) 9148– 9153.

[28] Z. Du, H. Zhao, Y.Shen, L. Wang, M. Fang, K. Świerczek, K. Zheng, Evaluation of $La_{0.3}Sr_{0.7}Ti_{1-x}Co_xO_3$ as a potential cathode material for solid oxide fuel cells, J. Mater. Chem. A 2 (2014) 10290-10299.

[29] X. Li, H. Zhao, F. Gao, Z. Zhu, N. Chen, W. Shen, Synthesis and electrical properties of Co-doped $Y_{0.08}Sr_{0.92}TiO_{3-\delta}$ as a potential SOFC anode, Solid State Ionics 179 (2008) 1588-1592.

[30] K.K. Hansen, A-site deficient $(Pr_{0.6}Sr_{0.4})_{1-\sigma}Fe_{0.8}Co_{0.2}O_{3-\delta}$ perovskites as solid oxide fuel cell cathodes, J. Electrochem. Soc. 2009 156(10) B1257-B1260.

[31] G. Xiao, Q. Liu, S. Wang, V. G. Komvokis, M. D. Amiridis, A. Heyden, S. Ma, F. Chen, Synthesis and characterization of Mo-doped $SrFeO_{3-\delta}$ as cathode materials for solid oxide fuel cells, J. Power Sources 202 (2012) 63– 69.

[32] P.A.W. van der Heide, Systematic x-ray photoelectron spectroscopic study of $La_{1x}Sr_x$-based perovskite-type oxides, Surf. Inter. Anal. 33 (2002) 414-425.

[33] R. Scurtu, S. Somacescu, J.M.C.-Moreno, D. Culita , I. Bulimestru, N. Popa, A. Gulea, P. Osiceanu, Nanocrystalline $Sm_{0.5}Sr_{0.5}CoO_{3-\delta}$ synthesized using a chelating route for use in IT-

SOFC cathodes: Microstructure, surface chemistry and electrical conductivity, J. Solid State Chem. 210 (2014) 53–59.

[34] C.B. Azzoni, M.C. Mozzati, A. Paleari, V. Massarotti, D. Capsoni, M. Bini, Z. N. Forsch., Magnetic Order in Li-Mn Spinels , Z. Naturforsch. 53a (1998) 693.

[35] J. H. Kim, S. Baek, C. Lee, K. Park, J. Bae, Performance analysis of cobalt-based cathode materials for solid oxide fuel cell, Solid State Ionics, 179 (2008) 1490-1496.

[35] T. Yamashita , P. Hayes, Analysis of XPS spectra of Fe^{2+} and Fe^{3+} ions in oxide materials, App. Surf. Sci. 254 (2008) 2441–2449.

[36] C. Xia, M. Liu, Low-temperature SOFCs based on $Gd_{0.1}Ce_{0.9}O_{1.95}$ fabricated by dry pressing, Solid State Ion. 144 (2001)249–255.

[37] J. Meng, X. Liu, L. Han, Y. Bai, C. Yao, X. Deng, X. Niu, X. Wu, J. Meng, Improved electrochemical performance by doping cathode materials $Sr_2Fe_{1.5}Mo_{0.5-x}Ta_xO_{6-\delta}$ ($0.0 \leq x \leq 0.15$) for solid state fuel cell, J. Power Sources 247 (2014) 845-851.

[38] S.B. Adler, J.A. Lane, B.C.H. Steele, Electrode kinetics of porous of mixed conducting oxygen electrodes, J. Electrochem. Soc. 143 (1996) 3554-3564.

[39] D. S. Khaerudini, G. Guan, P. Zhang, X. Hao, Z. Wang, C. Xue, Y. Kasai, A. Abudula, Performance assessment of $Bi_{0.3}Sr_{0.7}Co_{0.3}Fe_{0.7}O_{3-\delta}$-LSCF composite as cathode for

intermediate-temperature solid oxide fuel cells with $La_{0.8}Sr_{0.2}Ga_{0.8}Mg_{0.2}O_{3-\delta}$ electrolyte, J. Power Sources 298 (2015) 269-279.

[40] S. B. Adler, Mechanism and kinetics of oxygen reduction on porous $La_{1-x}Sr_xCoO_{3-\delta}$ electrodes, Solid state ionics 111 (1998) 125-134.

[41] S. Guo, H. Wu, F. Puleo, L.F. Liotta, B-Site Metal (Pd, Pt, Ag, Cu, Zn, Ni) Promoted $La_{1-x}Sr_xCo_{1-y}Fe_yO_{3-\delta}$ Perovskite Oxides as Cathodes for IT-SOFCs, catalysts 5(2015) 366-391.

[42] T. J. Huang, X. D. Shen, C. L. Chou, Characterization of Cu, Ag and Pt added $La_{0.6}Sr_{0.4}Co_{0.2}Fe_{0.8}O_{3-\delta}$ and gadolinia-doped ceria as solid oxide fuel cell electrodes by temperature-programmed techniques, J. Power Sources 187 (2009) 348-355.

[43] D. N. Miller, J. T.S. Irvine, B-site doping of lanthanum strontium titanate for solid oxide fuel cell anodes, J. Power Sources, 196 (2011) 7323-7327.

Chapter 4 Evaluation of cerium doped perovskites $(Ce_{0.1}Sr_{0.9})_xCo_{0.3}Fe_{0.7}O_{3-\delta}$ as cathode materials for solid oxide fuel cells

4.1 Introduction

Solid oxide fuel cells (SOFCs) have received much attention in recent years due to its high efficiency with low pollution [1]. A typical SOFC includes three parts, i.e., the electrolyte, cathode, and anode. When hydrogen is used as the fuel, hydrogen decomposition on the anode side generates hydrogen ions (protons) and electrons, and the generated protons pass through the dense electrolyte to the cathode, and react with oxygen there to form water. In this process, gas diffusions in the anode and cathode to the electrode/electrolyte interface play an important role in the performance of SOFCs[2]. Meanwhile, the effective ion conducting in the electrolyte is also essential. To date, various ionic conducting oxide materials such as Gadolinium doped Ceria (GDC) [3], Yttria stabilized Zirconia(YSZ) [4] and Strontium- and Magnesium-doped Lanthanum Gallium oxide (LSGM) [5] have been developed and used as the electrolyte. Recently, it is found that the mixed conductor materials are excellent candidates as cathode materials of SOFCs. Among them, the perovskite type is the main one [6]. Ceramic materials have been widely used in the dense oxygen permeation membranes, catalysts for hydrocarbon

oxidation, oxygen sensors and cathode materials for SOFCs [7, 8]. Especially, ABO_3-type perovskite oxide, in which Ln, Sr, and Ba are the most popular elements for A-site and Mn, Co, Ni are the most popular elements for B-site, is common one [9]. To understand the effect of substitution of other cations in B-site on the performance of perovskite materials, Nagai et al. doped different elements including Nb, V, Zr, Ti, Ce, In, Ga, Al, Fe, Cr, Zn, Cu and Ni in $SrCoO_{3-\delta}$ based perovskite and found that Fe doped one, i.e., $Sr(Co_{0.9}Fe_{0.1})O_{3-\delta}$ exhibited the best performance [10]. According to the previous investigations, rare earth metals such as La, Pr, Nd, Sm and Gd were found to be the best choice as the A-site elements, and in addition, Ba-doping can achieve high power density at low temperature [27]. For $Ln_{0.6}Sr_{0.4}$-based (Ln= Ba, La, Pr, Nd, Sm and Gd) cathode [28], a Ln with a larger radius doped to A-site resulted in excellent electrical conductivity performance. Lee et al. [29] found that when La was doped to $Ln_{0.6}Sr_{0.4}CoO_{3-\delta}$ (Ln=La, Pr, Nd, Sm and Gd) , the maximum electrical conductivity and performance were obtained, however, doping of La also led to a higher TEC.

Meanwhile, A-site cation deficiencies in the lattice structure of perovskite were also found to have significant effect on the material performance since the A-site deficiency can provide more oxygen vacancies based on the charge compensation, and enhance the oxygen ion conductivity in the cathode [11]. Moreover, the A-site deficiency could reduce

the electrical conductivity of the material due to the formation of oxygen vacancies [12]. Thusly, it is important to find a suitable element doping on A-site to achieve the best performance of the material.

In this study, doping of Cerium (Ce) on A-site of $Sr_{0.9}Co_{0.3}Fe_{0.7}O_{3-\delta}$ with different amounts to form perovskite of $(Ce_{0.1}Sr_{0.9})_xCo_{0.3}Fe_{0.7}O_{3-\delta}$ ($(CS)_xCF$, x=0.9,0.95,1.0,1.05 and 1.10) was carried out. The effects of A-site deficiency and excess on the electrical conductivity, oxygen desorption property, composition and valence of each element on the surface and polarization resistance were investigated. Furthermore, a single cell of $La_{0.8}Sr_{0.2}Ga_{0.8}Mg_{0.2}O_{3-\delta}$(LSGM) supported SOFCs with $(CS)_xCF$ as the cathode and NiO-$Sm_{0.2}Ce_{0.8}O_{1.9}$(SDC) as the anode was fabricated and tested. It is expected that the larger ionic radius of Ce could result in a larger free volume to supply a large transportation pathway for oxygen ions, consequently enhance the diffusion of oxygen in bulk and improve the oxygen ion conductivity.

4.2 Experimental

4.2.1 Sample preparation and cell fabrication

$(Ce_{0.1}Sr_{0.9})_xCo_{0.3}Fe_{0.7}O_{3-\delta}$ ($(CS)_xCF$) (x=0.90, 0.95, 1.0, 1.05and 1.10) perovskites were prepared by using a solid-state reaction method, in which oxide, nitrate and

carbonate powders, i.e., $Ce(NO_3)_3 \cdot 6H_2O$, $SrCO_3$, $Co(NO_3)_2 \cdot 6H_2O$ and Fe_2O_3 (99.9% Wako, Japan), were used. The stoichiometric amounts of these chemicals were completely mixed by ball milling for 10 h at first, and then calcined at 1100 °C for 10 h in air. Herein, based on the preliminary experiments, it is found that when the mixtures were calcined at this condition, the pure phase can be obtained. Finally, the obtained product with pure phase was treated by ball milling for 5 h again. For the conductivity test, the finely ground powder was pressed into a bar under a uniaxial pressure of 100 MPa, followed by sintering at 1200 °C for 10 h in air with a heating rate of 3°C min^{-1}. The commercially available powder, $La_{0.8}Sr_{0.2}Ga_{0.8}Mg_{0.2}O_{3-\delta}$ (LSGM, 99.9% FCM, USA), was used for the fabrication of electrolyte. In brief, a dense LSGM pellet with 20 mm in diameter was obtained by pressing the LSGM powder at 220 MPa and then sintered at 1450 °C for 10 h in air. An anode material, NiO-SDC (Samarium-doped cerium oxide ($Sm_{0.2}Ce_{0.8}O_{1.9}$, Kojundo Chemical Laboratory Co., Ltd.)) powder, was prepared as reported elsewhere [13]. Symmetrical cell of $(CS)_xCF$/LSGM/$(CS)_xCF$ for impedance test and the single SOFC cell of $(CS)_xCF$ /LSGM/NiO-SDC were prepared by the slurry coating method. In brief, the $(CS)_xCF$ /LSGM/NiO-SDC cell was fabricated as follows: NiO-SDC slurry was coated on the anode side of LSGM electrolyte pellet and then calcined at 1350 °C for 2 h. Thereafter, $(CS)_xCF$ slurry was coated onto the cathode side

and then sintered at 1250 °C for 2 h in air. For the single cell performance testing, the cell was sealed on an alumina tube using a Pyrex glass ring.

4.2.2 Material characterization

Crystallographic phases of the $(CS)_xCF$ powders were characterized using a RIGAKU Smartlab X-ray diffractometer (XRD) with CuKα radiation (λ=0.154 nm) generated at 45 kV and 200 mA. The conductivity of sintered $(CS)_xCF$ bar was determined by the four-terminal DC method, in which the temperature was increased from 100 to 900 °C with an interval of 50 °C and maintained for 10 min at each temperature before the conductivity was measured in order to make the system equilibrated. The composition and valence of each element on the surface of fresh powder were determined by X-ray photoelectron spectroscopy (XPS, AXIS ULTRA DLD, Japan).

Oxygen desorption properties of different samples as a function of temperature were monitored by a Belcat oxygen temperature programmeddesorption (O_2-TPD) catalyst analyzer (Belcat, BelJapan, Inc.). In brief, approximately 0.1 g of powder was placed ina quartz fixed-bed microreactor with 8 mm inner diameter. Before each run, the sample was treated in O_2 atmosphere with a flow rate of 20 cm^3 min^{-1} at 500 °C for 1 h to confirm that O_2 was adsorbedand activated completely across the bulk structure of the sample. Then,

the sample was cooled down to room temperature in O_2 atmosphere, followed by purging with a helium flow rate of 50 cm^3 min^{-1} for30 min to remove all gas-phaseoxygen in the oxygen system. Thereafter, the sample was heated from room temperature to900 ^oC with a heating rate of 10 ^oC min^{-1}. The effluent gas was monitoredby a thermal conductivity detector (TCD). The amount of O_2desorbed from the sample was quantified by calibrating the peakarea against that of a standard O_2 pulse.

Half-cell and symmetrical cell were fabricated for the polarization resistance and cell performance tests, respectively, in a temperature range of 700-850 °C. A frequency response analyzer and a potentiostat (Solartron 1255B and 1287) were applied for the measurement of electrochemical impedance spectra (EIS) of the half-cell at open circuit voltage (OCV) over the frequency range of 0.01 Hz-1MHz with the AC signal amplitude of 10 mV. The impedance response was analyzed using the equivalent resistor–capacitor circuit method. Before the single SOFC performance test, the anode was annealed at 900 °C in H_2 for 1 h. Then, the test was performed in a wet H_2 (3% H_2O) flow with a flow rate of 50 cm^3 min^{-1}. Here, air was introduced into the cathode side with a flow rate of 50 cm^3 min^{-1}. Au paste was used to enhance the electronic contact with a Pt mesh. The impedance of the single SOFC after the cell performance test was also measured at the OCV using the same method.

4.3. Results and discussion

4.3.1 Structural characterization

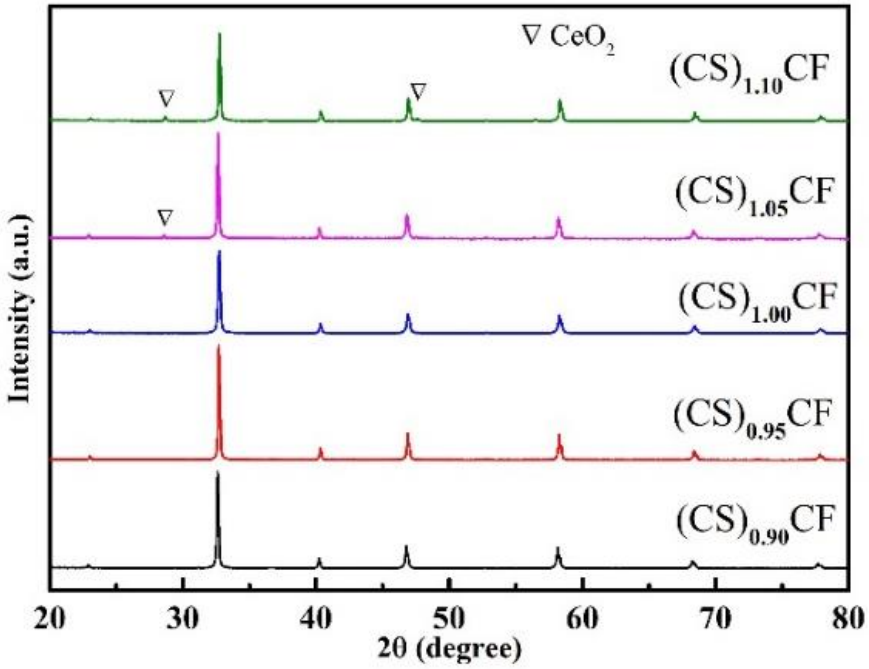

Figure 4.1 XRD patterns of $(CS)_xCF$ ($0.90 \leq x \leq 1.10$) sintered at 1100 ^oC in air.

Figure 4.1 displays XRD patterns of $(Ce_{0.1}Sr_{0.9})_xCo_{0.3}Fe_{0.7}O_{3-\delta}$ ($(CS)_xCF$, x=0.90,0.95,1.00,1.05 and 1.10) powders calcined at 1100 ^oC for 8 h in air. Characteristic peaks were appeared at 2θ of 32˚, 41˚, 47˚, 58˚, 68˚ and 77˚. One can see that the pure phase was obtained as x was 0.90, 0.95 or 1.00, but the impurity phase appeared at 2θ of around 29˚, 47.5˚as x was more than 1.00 since the A-site proportion exceeded the general value of ABO_3-peroviskite. Furthermore, the patterns peaks of $(CS)_xCF$ can be well indexed based on cubic perovskite lattice with Pm-3m (# 221) space group was formed with the equal value of a, b, c. The specific unit-cell parameters were calculated and the

results are listed in Table 4.1. One can see that the lattice volume increased with the decrease in A-site deficiency, and the A-site deficiency had great influence on the lattice parameters.

Table 4.1 Unit-cell parameters of the $(CS)_xCF$ samples.

Samples	a (Å)	Volume ($Å^3$)	Space group
$(CS)_{0.90}CF$	3.8861	58.69	Pm-3m
$(CS)_{0.95}CF$	3.8965	59.16	Pm-3m
$(CS)_{1.00}CF$	3.9069	59.63	Pm-3m
$(CS)_{1.05}CF$	3.9170	60.10	Pm-3m
$(CS)_{1.10}CF$	3.9240	60.42	Pm-3m

4.3.2 Electrical conductivity

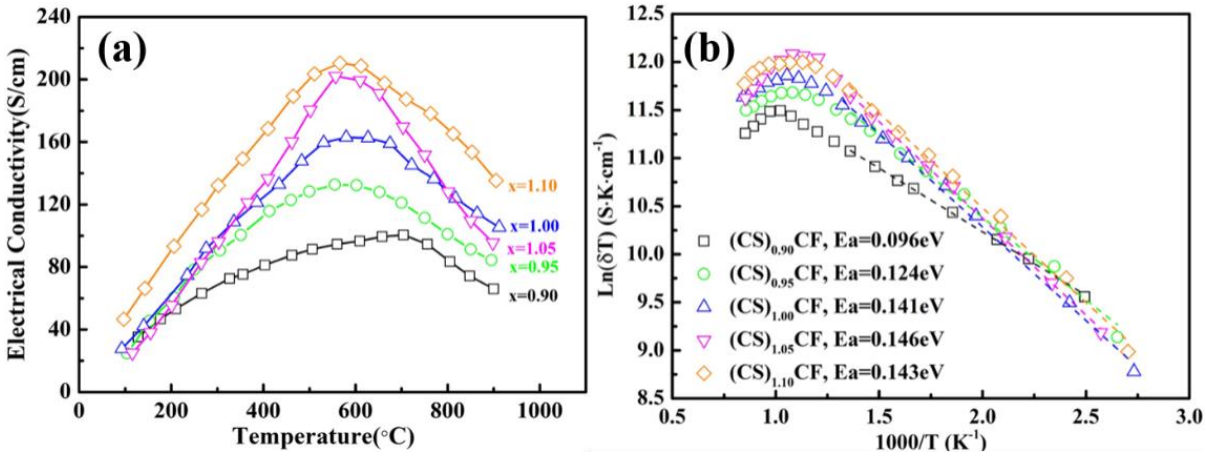

Figure 4.2 (a) Electrical conductivity in the range of 100-900°C (b) Corresponding Arrhenius plots of the $(CS)_xCF$ ($0.90 \leq x \leq 1.10$) in air.

Electrical conductivity (σ) of $(CS)_xCF$ (x=0.9, 0.95, 1.0, 1.05 and 1.1) in air as a

function of temperature ranged from 100 to 900 ^{o}C is shown in Figure 4.2(a). One can see that the conductivity increased with the increase in temperature until the maximum conductivity reached, and then decreased with the further increase in temperature. This indicates that $(CS)_xCF$ materials has p-type conducting behavior. And this behavior due to, before the transition temperature (Ts), they followed the small polaron hopping mechanism, where the electron and hole acted as the charge carriers. However, as the temperature was over T_s, the oxygen in the perovskite was lost and oxygen vacancies were formed by decoupling of the d-orbitals of the transition metal and the p-orbitals of oxygen [14]. Herein, it is actually constructed by the hopping hole between Fe^{2+} and Fe^{3+}, and the charge compensation by the reduction of Co^{3+} to Co^{2+}[12]. As shown in Figure 4.2(a), the electrical conductivity decreased with the increase in the A-site deficiency since the increase in deficiency amount decreased the p-type electronic carriers. The formation of A-site deficiency can be expressed as:

$$\boldsymbol{O_O^X = V_{\ddot{O}} + 2e' + \frac{1}{2}O_2} \quad (1)$$

From Figure 4.2(a), one can see that the transition temperature appeared at 500-600 ^{o}C, and the maximum conductivity values of all samples achieved 110-210 Scm^{-1}, in which $(CS)_{1.00}CF$ exhibited the maximum conductivity value of 163 Scm^{-1} at 580 ^{o}C. In contrast, the similar Fe-Co based cathode material of BSCF showed a much lower maximum

conductivity of 27.5 Scm^{-1} at 600 ºC [15]. However, the formation of oxygen vacancies could hinder the polaron hopping, leading to the decrease of concentration of charge carriers, which should be the reason why the electrical conductivity decreased after the temperature was over Ts. The annihilation of holes can be described in Equation (2):

$$\boldsymbol{e' + h^{\cdot} = 0} \quad (2)$$

With the increase in A-site deficiency, oxygen vacancies can be formed in the lattice. Based on the charge compensation mechanism, more oxygen vacancies could be formed instead of the oxidation [11]. Moreover, as shown in Figure 4.2(b), the activation energy increased with the decrease in A-site deficiency. Furthermore, based on the slopes of the Arrhenius plots of Ln (δT) at low temperature range of 100-500 ºC, the activation energy (Ea) can be calculated. Herein, the relationship of the conductivity δ and temperature T can be expressed by the following equation:

$$\sigma=\frac{\mathbf{C}}{\mathbf{T}}\exp\left(\frac{\mathbf{-Ea}}{\mathbf{kT}}\right) \quad (3)$$

where C is the pre-exponential constant, which is related to the charge carrier content and other material properties; T is temperature; k is the Boltzmann's constant and Ea is the activation energy. The lower Ea indicates higher catalytic activity of ORR. As shown in Figure 4.2(b), Ea were 0.096, 0.124, 0.141, 0.146, 0.143eV for $(CS)_{0.90}CF$, $(CS)_{0.95}CF$, $(CS)_{1.00}CF$, $(CS)_{1.05}CF$ and $(CS)_{1.10}CF$, respectively. That is, Ea incerased with the

decrease in A-site deficiency, indicating that A-site deficiency enhanced the catalytic activity . In contrast, the above mentioned BSCF material had an Ea value of 0.366eV [15], which was much higher than that of $(CS)_{1.00}CF$, indicating that the CSCF materials have high potential to be used as the cathode material of SOFCs.

4.3.3 XPS analysis

XPS analysis was used to characterize the composition and valence of each element on the surface of (CS)xCF material. Here, the valence state of Fe and O were estimated by curve-fitting of the Fe 2p (Figs. 3 a-c) and O 1s (Figs. 3 d-f) signals, as shown in Figure 4.3. The Fe 2p signals enveloped the signals from Fe2+, Fe3+ and Fe4+, where that from Fe2+ (2p3/2/2p1/2), Fe3+ (2p3/2/2p1/2) and Fe4+(2p1/2/2p3/2) located at 709.4-709.7/722.6-723.0 eV, 710.6-711.0/723.8-724.1 eV, and 712.6-712.8/724.9-725.4eV, respectively. This fitting result was in agreement with the results reported by Pan et al. [16], Lu et al. [17] and Yamashita et al. [18]. The percentage contributions of the valence states of Fe are summarized in Table 4.2.

Table 4.2 The proportion of valence states of Fe in $(CS)_xCF$ (x=0.90,1.00,1.10) samples.

	Fe^{2+} (%)	Fe^{3+} (%)	Fe^{4+} (%)
$(CS)_{0.90}CF$	46.3	33.7	20.0
$(CS)_{1.00}CF$	35.6	40.4	24.0
$(CS)_{1.10}CF$	31.3	41.0	27.7

$$2Fe^{3+} \leftrightarrow Fe^{2+} + Fe^{4+} \quad (4)$$

$(CS)_xCF$ is mix valence iron materials. When Fe^{3+} can be oxidized toFe^{4+}, based on the charge compensation mechanism, in this case, A-site deficient perovskite can be formed, resulting in the generation of oxygen vacancies [11]. As shown in Table 4.2, along with the increase of x, Fe^{2+} percentage decreased, indicating that Fe^{2+} was oxidized to Fe^{3+}/Fe^{4+}. These results confirmed that the increase in A-site deficiency led more oxygen vacancies were formed.

In Figure.4.3 (d-f), the O 1s core level spectrum consisted of higher bonding energy (HBE) and lower bonding energy (LBE). Here, HBE is the typical feature of hydroxyl group along with carbonate structure (active oxygen) while LBE stands for the lattice oxygen. LBEs of $(CS)_xCF$ (x= 0.9, 1.0 and 1.1) located at the positions of 528.5, 528.6 and 529.3 eV while the corresponding HBEs located at 531.1, 531.3 and 531.6 eV, respectively. It is obvious that the lower binding energy shifted to the left with the decrease in x, and the peak area corresponding to the lattice oxygen also increased,

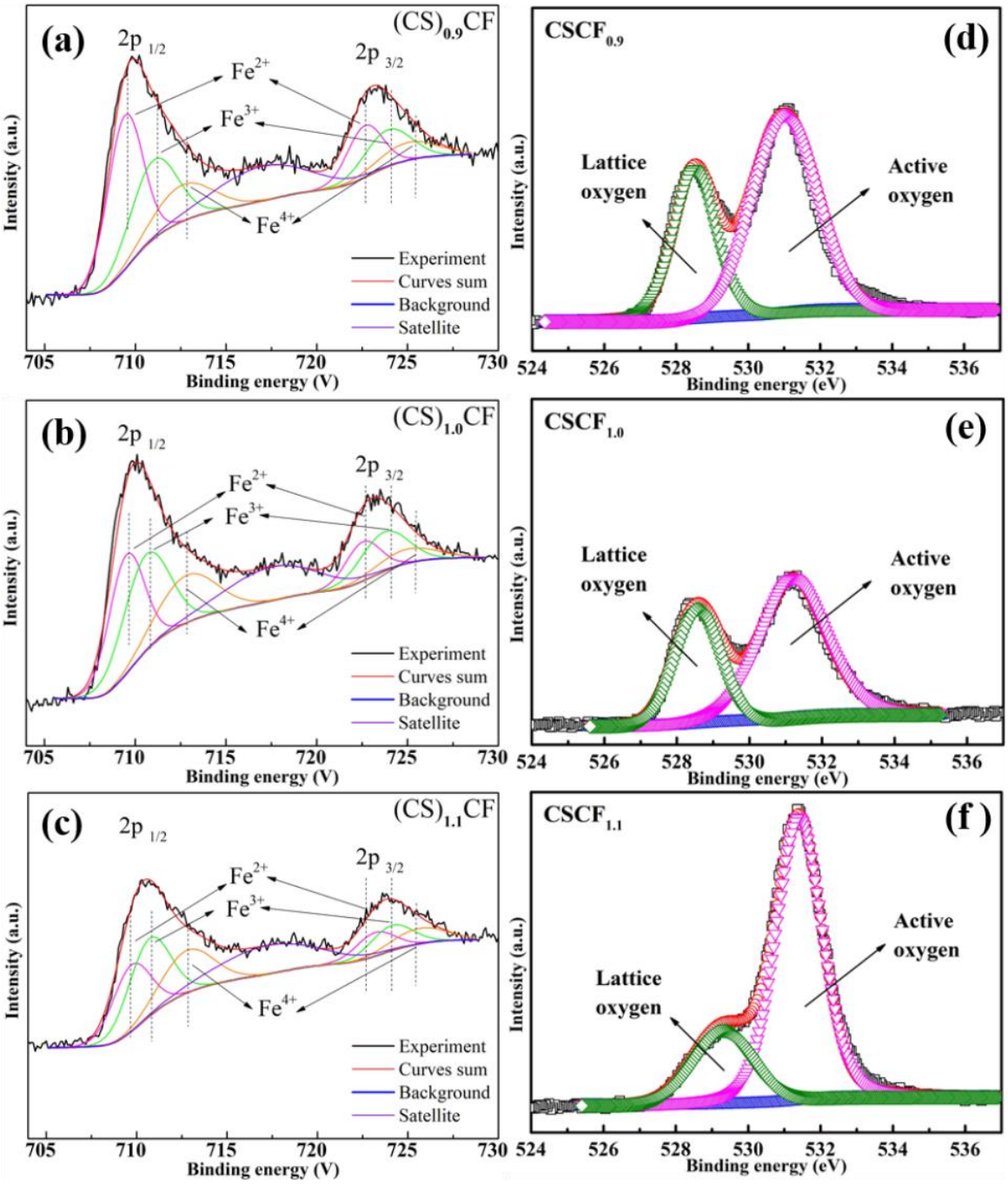

Figure 4.3 (a-c) XPS spectra of Fe 2p and (d-f) O 1s in $(CS)_xCF$ (x=0.90,1.00, and 1.10).

indicating that the concentration of oxygen vacancies increased due to the increase in the A-site deficiency [19]. The minimum conductivity value of $(CS)_{0.9}CF$ among the obtained

materials should be resulted from its maximum oxygen vacancy.

4.3.4 O_2-TPD

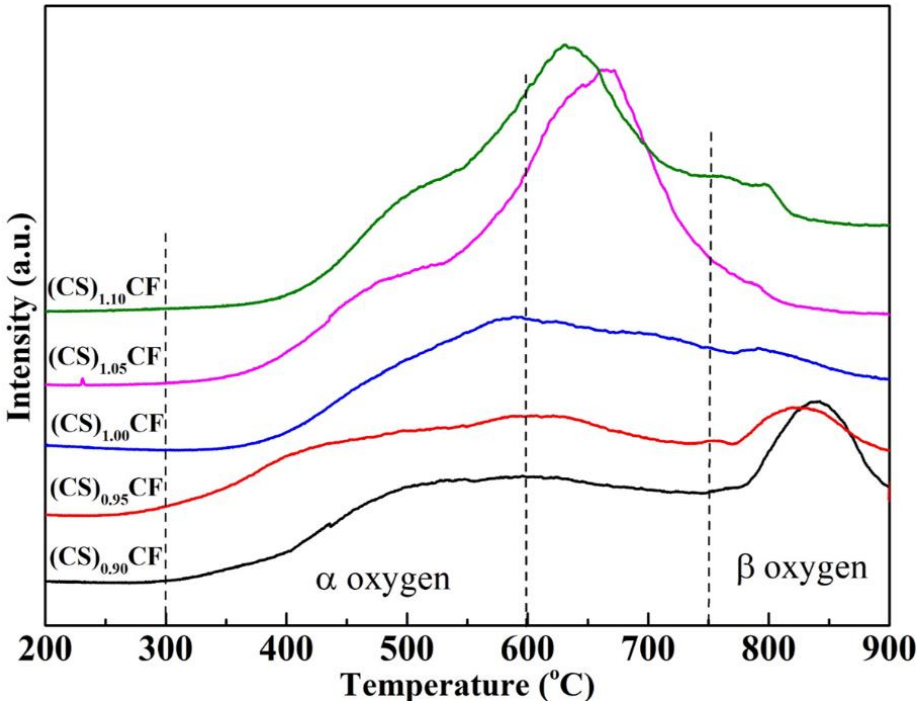

Figure 4.4 O_2-TPD profiles of $(CS)_{0.90}CF$, $(CS)_{0.95}CF$, $(CS)_{1.00}CF$, $(CS)_{1.05}CF$ and $(CS)_{1.10}CF$.

The oxygen desorption characteristics were determined by the temperature programmed desorption of oxygen (O_2-TPD) technique as reported in the literature [20]. α-oxygen desorbed at a lower temperature range during O_2-TPD measurement was confirmed here. In general, with the increase in oxygen vacancy concentration, the desorption peak corresponding to the α-oxygen should become more obvious, which also relates to the valences change of B-site ions [21]. Figure 4.4 shows O_2-TPD profiles of

$(CS)_{0.90}CF$,$(CS)_{0.95}CF$, $(CS)_{1.00}CF$, $(CS)_{1.05}CF$ and $(CS)_{1.10}CF$ after O_2 adsorption at 500 ^oC for 1 h. All samples exhibited two desorption peaks although some were not so obvious. Here, a-oxygen released at the temperature range of 300-600^oC and β-oxygen released at higher than 750^oC are associated with the formation of oxygen vacancies and desorption of surface oxygen on the lattice, respectively, as suggested by He et al. [21] and Deni et al. [20]. From these results, the oxygen vacancies on the surface can be estimated. As shown in Figure 4.4, an apparent peak was found for $CSCF_{1.05}$ or $CSCF_{1.10}$ when the temperature was over 550 ^oC, but this peak was not so apparent for other three materials. Here, with the increase in x, different valences of iron could be changed among Fe^{2+}, Fe^{3+} and Fe^{4+}. This has been confirmed by XPS analysis for Fe 2p shown above. Meanwhile, the second peak corresponding to β-oxygen desorption was observed at the temperature range over 750 ^oC. However, it should be noted that this peak was not so apparent when $x \geqslant 1$. As confirmed in Figure 4.3 (d-f), with the increase in x, the lattice oxygen also decreased. Here, the amounts of α-oxygen desorption over the $(CS)_{0.90}CF$, $(CS)_{0.95}CF$, $(CS)_{1.00}CF$, $(CS)_{1.05}CF$ and $(CS)_{1.10}CF$ were estimated to be 0.219, 0.234, 0.249, 0.283 and 0.298 mmol/g, respectively. Comparing with other A-site deficient materials, i.e., $(Bi_{0.4}Sr_{0.6})_xCo_{0.3}Fe_{0.7}O_{3-\delta}$ (x=0.9, 1.0) [22] with the amounts of α-oxygen desorption of 0.237 and 0.267 mmol/g, $(CS)_xCF$ had lower α-oxygen desorption ability, confirming that

$(CS)_{0.90}CF$, $(CS)_{0.95}CF$, $(CS)_{1.00}CF$ have strong adsorption ability to O_2. This result also confirmed that the oxygen vacancy increased with the increase in A-site deficiency, which is essential for ORR.

4.3.5 Electrocatalytic activity

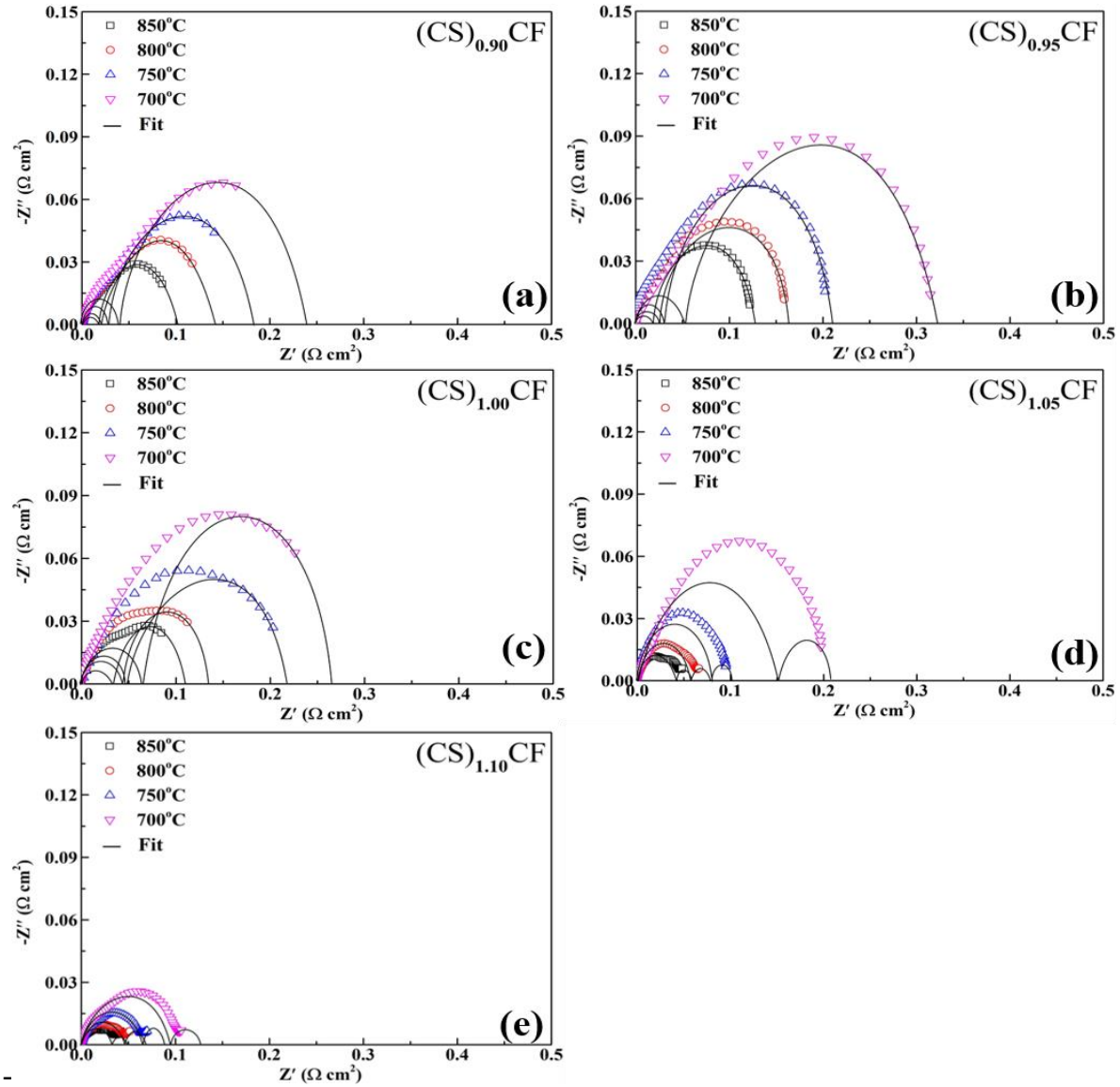

Figure 4.5 Nyquist plots of impedance at a temperature range of 700-850°C for (a)$(CS)_{0.90}CF$, (b) $(CS)_{0.95}CF$, (c)$(CS)_{1.00}CF$, (d) $(CS)_{1.05}CF$ and (e) $(CS)_{1.10}CF$.

Electrical impedance spectra (EIS) of the $(CS)_xCF/LSGM/(CS)_xCF$ symmetrical cells with a LSGM electrolyte thickness of 500 μm in the temperature range of 700-850 ^oC are displayed in Figure 4.5. Here, EIS values can be also used to quantify the ORR activity of $(CS)_xCF$ materials. In this study, ohmic resistance was set at zero. EIS behavior included high frequency polarization resistance (R_{HF}) and low frequency polarization resistance (R_{LF}). The sum of the R_{HF} and R_{LF} corresponds to the polarization resistance (R_P) of the cathode/electrolyte interface. R_{HF} refers to the middle frequencies ranged from 10^3 to 10^2 Hz, corresponding to the ion charge transport resistance [23] while R_{LF} refers to the lower frequencies ranged from the 10^1-10^{-1} Hz arc, which represents the oxygen adsorption and dissociation processes [24]. As shown in Figure 4.5, all R_p values for the detected materials increased with the decrease in the operation temperature, indicating that high temperature enhanced the catalytic activity. As such, the minimum R_p values of $(CS)_{0.90}CF$, $(CS)_{0.95}CF$, $(CS)_{1.00}CF$, $(CS)_{1.05}CF$ and $(CS)_{1.10}CF$ obtained at 850 ^oC were estimated to be 0.010, 0.124, 0.107, 0.057, 0.047 Ω cm^2, respectively.

Table 4.3 High-and low-frequency polarization resistances in air at the temperature range of 700-850 ^oC.

Cathode	Temperature	R_P(Ω cm^2)	R_{HF}(Ω cm^2)	R_{LF}(Ω cm^2)

$(CS)_{0.90}CF$	850	0.100	0.017	0.083
	800	0.141	0.020	0.121
	750	0.181	0.027	0.154
	700	0.235	0.040	0.195
$(CS)_{0.95}CF$	850	0.124	0.020	0.104
	800	0.161	0.027	0.134
	750	0.210	0.030	0.180
	700	0.318	0.050	0.268
$(CS)_{1.00}CF$	850	0.107	0.034	0.073
	800	0.134	0.044	0.090
	750	0.204	0.047	0.157
	700	0.261	0.064	0.194
$(CS)_{1.05}CF$	850	0.057	0.040	0.017
	800	0.077	0.057	0.020
	750	0.100	0.077	0.023
	700	0.201	0.147	0.054
$(CS)_{1.10}CF$	850	0.047	0.030	0.017
	800	0.067	0.047	0.020
	750	0.087	0.067	0.020
	700	0.124	0.094	0.030

As shown in Table 4.3, when x >1, lower Rp values were obtained. Here, $(CS)_{0.90}CF$ and $(CF)_{0.95}CF$ exhibited higher total polarization resistances, but their R_{HF} were lower than R_{LF}. It is reported that the high frequency usually relates to the charge transfer while

the low frequency relates to the mass-transfer. As such, to improve the interaction activity with surface oxygen, the rate of oxygen ion transfer should be enhanced [20]. As confirmed by O_2-TPD analysis shown above, when x<1, more oxygen vacancies existed in the material, resulting in its R_p higher but its R_{HF} lower than those materials with x>1. Herein, R_p decreased but R_{HF} increased with the increase in x, indicating that the ORR of material decreased with the increase in x. As x was increased until 1.05, R_{HF} was higher than R_{LF}. For $(CS)_{1.05}CF$ and $(CS)_{1.10}CF$, the R_{HF} contribution to the total polarization resistance at 850 ^oC were 70% and 64 %, respectively.

As shown in Figure 4.6(a), the polarization resistance increased at first as x was increased from 0.90 to 0.95, and then decreased with the further increase of x since more A-site deficiencies were generated, increasing the oxygen vacancy amount. In this study, among all obtained materials, $(CS)_{0.90}CF$ had higher oxygen vacancy concentration with the minimum R_{HF} value. This has been confirmed by using XPS and O_2-TPD analyses as shown above. Other researchers also verified that the increase of A-site deficiency resulted in the decrease of R_p of cathode [25], although the total R_p decreased and R_{HF} started to increase. Figure 4.6(b) shows Arrhenius plots based on the total polarization resistance values indicated in Figure 4.5(a-e). Activation energies (Ea) were calculated as 0.529, 0.584, 0.591, 0.769 and 0.598 eV for $(CS)_xCF$ x=0.90, 0.95, 1.00, 1.05 and 1.10,

respectively, based on the equation (3). One can see that much lower Ea values were obtained for the present materials than that of $Bi_{0.3}Sr_{0.7}Co_{0.3}Fe_{0.7}O_{3-\delta}$ (Ea=0.82 eV) [22].

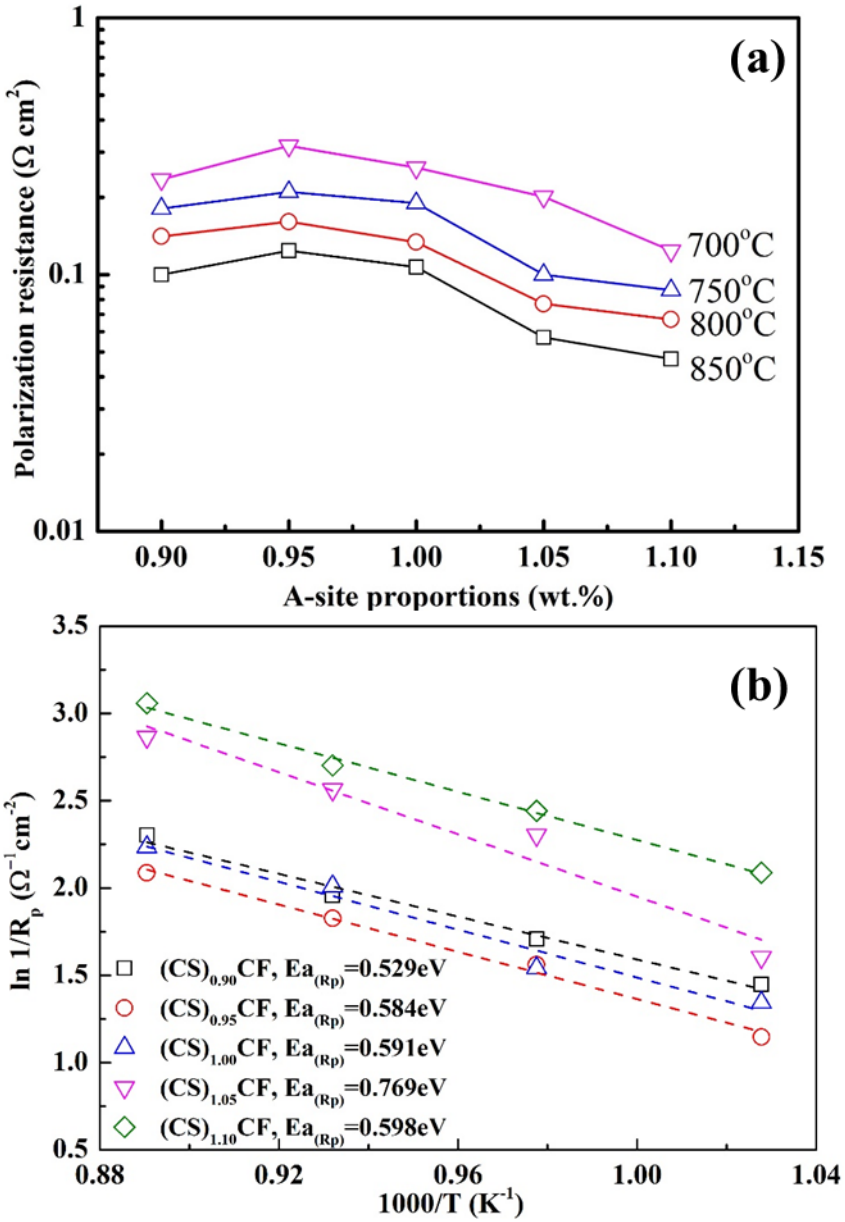

Figure 4.6 (a) Effect of A-site deficiency on the polarization resistance at the temperature range of 700-850°C.(b) Corresponding Arrhenius plots based on the polarization resistances for $(CS)_xCF/LSGM/(CS)_xCF$ ($0.90 \leq x \leq 1.10$).

Here, the Ea value increased with the increase in x. In general, the lower Ea indicates higher catalytic activity and thusly, the obtained materials are expected to have high performance for SOFCs.

4.3.6 Cell performance

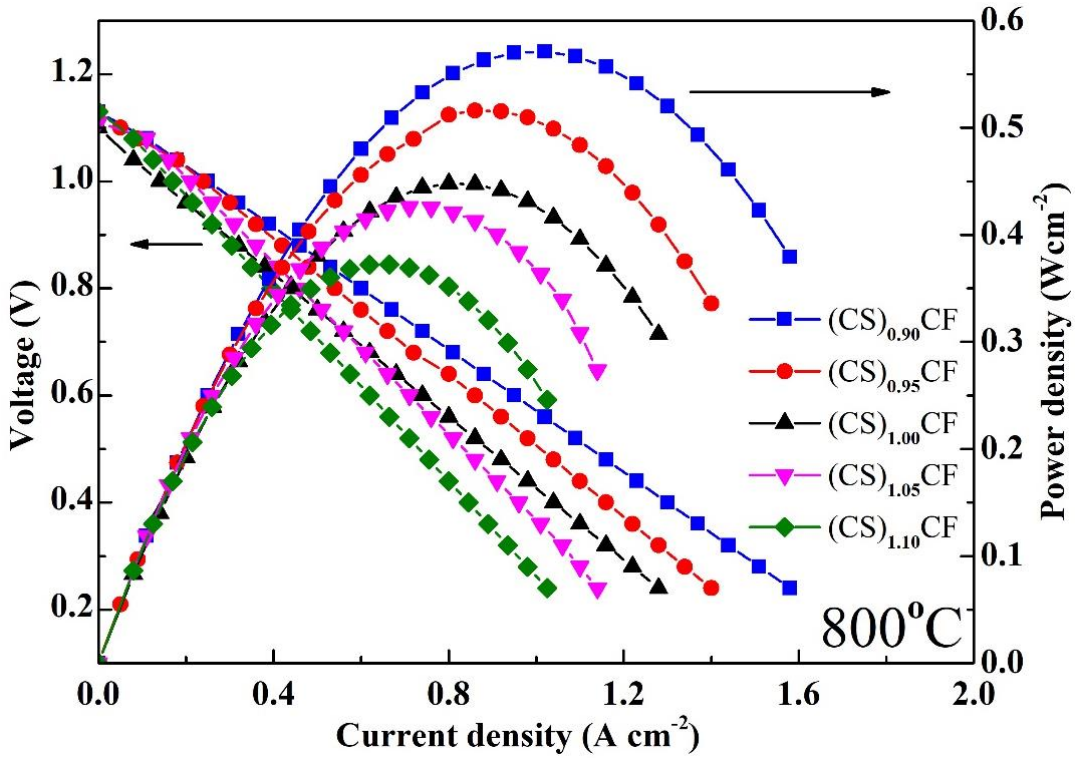

Figure 4.7 Single cell performance of LSGM electrolyte supported $(CS)_xCF$/LSGM/NiO-SDC (x=0.90, 0.95, 1.00, 1.05, 1.10) measured in H_2 as the fuel , oxygen as the oxidant at 800 ^oC.

Figure 4.7 displays the current density-potential (I-V) properties at 800 ^oC and the current density-power density (I-P) plots for the single cell of LSGM supported SOFCs with $(CS)_xCF$ as the cathode. Here, all open-circuit voltages (OCVs) were approximately

1.1 V at 800 °C. As shown in Figure 4.7, the maximum power densities of $(CS)_{0.90}CF$, $(CS)_{0.95}CF$, $(CS)_{1.00}CF$, $(CS)_{1.05}CF$ and $(CS)_{1.10}CF$ were 0.571, 0.516, 0.448, 0.426 and 0.372 Wcm^{-2}, respectively. It should be noted that these power density values were much higher than those of the similar Co-Fe based materials of $GdBa_{0.5}Sr_{0.5}Co_{1.5}Fe_{0.3}O_{5+\delta}$ (0.27 Wcm^{-2} at 800 °C) [26]. It is obvious that the materials with $x<1$ showed higher power densities than those with $x>1$. As stated above, A-site deficiency ($x<1$) provided more oxygen vacancies to enhance ORR compared with $(CS)_{1.00}CF$, the power density of $(CS)_{0.90}CF$ increased approximately 21.5% due to the A-site deficiency; and on the contrary, the power density $(CS)_{1.10}CF$ with A-site excess decreased approximately 17.0%. Moreover, as shown in Fig.1, in the case of $x>1$ with A-site excess some impurity phases appeared, which also resulted in the decrease of power density. Therefore, $(CS)_xCF$ with A-site deficiency should be promising materials for SOFCs.

4.4. Conclusions

In this study, cerium was doped on the A-site of perovskites of (CS)xCF with various x values and the applicability of the obtained materials for the cathode materials of SOFCs was investigated. Based on the XRD analysis, a perovskite phase was detected for all of the samples ($0.90 \leqslant x \leqslant 1.10$) when the precursor materials were calcined at 1100 °C for

10 h, but some impurity phases appeared as x>1.0. Furthermore, A-site variation had a great effect on the electrochemical performance of the Cerium doped $(CS)_xCF$ oxides. Especially, when x<1, more oxygen vacancies were generated so that the oxygen reduction reaction was improved, and the cell performance was enhanced. In addition, it is found that the minimum α-oxygen desorption amount of 0.219 mmol/g for $(CS)_{0.90}CF$ occurred in a temperature range of 300-600^oC. The SOFC cell with the constitution of $(CS)_{0.90}CF$/LSGM/NiO-SDC exhibited the maximum power density of 0.571 Wcm^{-2} at 800 ^oC. Indicating that $(CS)_{0.90}CF$ can be a promising cathode material for SOFCs.

References

[1]K. Nozawa, H. Orui, T. Komatsu, R. Chiba, H. Arai, Development of Highly Efficient Planar Solid Oxide Fuel Cells, NTT Technical review 6 (2008)1-5.

[2] J.D. Holladay, J. Hu, D.L. King, Y. Wang, An overview of hydrogen production technologies, Catal Today 139 (2009) 244–260.

[3] B. Dalslet, P. Blennow, P. V. Hendriksen, N. Bonanos, D. Lybye and M. Mogensen, Assessment of doped ceria as electrolyte, J. Solid State Electrochemistry 10 (2006) 547-561.

[4] J. W. Fergus, Electrolytes for solid oxide fuel cells, J. Power Sources 162 (2006) 30-40.

[5] N. Liu, M. Shi, C. Wang, Y. P. Yuan, P. Majewski and F. Aldinger, Microstructure and ionic conductivity of Sr- and Mg-doped $LaGaO_3$, J. Materials Science 41 (2006) 4205-4213.

[6] C. Yang, F. Zhao, F. Chen, M. Liu, Investigation of A-site deficient $Ba_{0.9}Co_{0.7}Fe_{0.2}Nb_{0.1}O_{3-\delta}$ cathode for proton conducting electrolyte based solid oxide fuel cells, International J. Hydrogen energy 39 (2014) 8431-8436.

[7] Q. Li, X. Zhu, Y. He, W. Yang, Partial oxidation of methane in $BaCe_{0.1}Co_{0.4}Fe_{0.5}O_{3-\delta}$ membrane reactor, Catal Today. 149 (2010) 185-190.

[8] N. Yamazoe, Y. Teraoka, Oxidation catalysis of perovskites—relationships to bulk structure and composition ,Catal Today 8 (1990) 175-199.

[9] J. Richter, P. Holtappels, T. Graule, T. Nakamura, L.J. Gauckler, Materials design for perovskite SOFC cathodes, MonatshChem 140 (2009) 985–999.

[10] T. Nagai, W. Ito, T. Sakon, Relationship between cation substitution and stability of perovskite structure in $SrCoO_{3-\delta}$-based mixed conductors, Solid State Ionics 177 (2007) 3433–3444.

[11]G.Ch. Kostogloudis, Ch. Ftikos, Properties of A-site-deficient $La_{0.6}Sr_{0.4}Co_{0.2}Fe_{0.8}O_{3-\delta}$-based perovskite oxides, Solid State Ionics 126 (1999) 143–151.

[12] A. Mineshige, J. Izutsu, M. Nakamura, K. Nigaki, J. Abe, M. Kobune, S. Fuji, T. Yazawa, Introduction of A-site deficiency into $La_{0.6}Sr_{0.4}Co_{0.2}Fe_{0.8}O_{3-\delta}$ and its effect on structure and conductivity, Solid State Ionics 176 (2005) 1145– 1149.

[13] P. Zhang, G. Guan, D.S. Khaerudini, X.Hao, C. Xue, M. Han, Y. Kasai, A. Abudula, Mo doped $Pr_{0.4}Sr_{0.6}Co_{0.2}Fe_{0.8}O_{3-\delta}$ cathode material with high catalytic activity for intermediate-temperature solid oxide fuel cells, Elctrochimic acta 146 (2014) 591-597.

[14] K. K. Hasen, A-Site Deficient $(Pr_{0.6}Sr_{0.4})_{1-s}Fe_{0.8}Co_{0.2}O_{3-\delta}$ Perovskites as Solid Oxide Fuel Cell Cathodes, J. the electrochemical society 156 (2009) B1257-1260.

[15] S. Li, Z. Lu, X. Huang, W. Su, Thermal, electrical, and electrochemical properties of

Nd-doped $Ba_{0.5}Sr_{0.5}$ $Co_{0.8}Fe_{0.2}O_{3-\delta}$ as a cathode material for SOFC, Solid State Ionic 178 (2008) 1853-1858.

[16] X. Pan, Z. Wang, B. He, S. Wang, X. Wu, C. Xia, Effect of Co doping on the electrochemical properties of $Sr_2Fe_{1.5}Mo_{0.5}O_6$ electrode for solid oxide fuel cell, International J. Hydrogen Energy 38 (2013) 4108-4115.

[17] S. Lu, B. Yu, X.Meng, X. Zhao, Y. Ji, C. Fu, Y. Zhang, L. Yang, H. Fan, J. Yang, Characterization of $SrCo_{0.7}Fe_{0.2}Nb_{0.1}O_{3-\delta}$ cathode materials for intermediate-temperature solid oxide fuel cells, J. Power Sources 273 (2015) 244-254.

[18] T. Yamashita, P. Hayes, Analysis of XPS spectra of Fe^{2+} and Fe^{3+} ions in oxide materials, Applid Surface Science 254 (2008) 2441-2449.

[19] P. Zhang, G. Guan, D.S. Khaerudini, X.Hao, C. Xue, M. Han, Y. Kasai, A. Abudula , B-site Mo-doped perovskite $Pr_{0.4}Sr_{0.6}$ $(Co_{0.2}Fe_{0.8})_{1-x}Mo_xO_{3-\sigma}$ (x = 0, 0.05, 0.1 and 0.2) as electrode for symmetrical solid oxide fuel cell, J. Power Sources 276 (2015) 347-356.

[20] D.S. Khaerudini, G. Guan, P. Zhang, , X.Hao, C. Xue, M. Han, Y. Kasai, A. Abudula J. Power Sources 298 (2015) 269-279.

[21] Y. He, X. Zhu, W. Yang, The role of A-site ion nonstoichiometry in the oxygen absorption properties of $Sr_{1+x}Co_{0.8}Fe_{0.2}O_3$ oxides , J. AIChe 57 (2011) 87-95

[22] D.S. Khaerudini, G. Guan, P. Zhang, , X.Hao, C. Xue, M. Han, Y. Kasai, A. Abudula,

Evaluation of $(Bi_{0.4}Sr_{0.6})xCo_{0.3}Fe_{0.7}O_{3-\delta}$ (x = 0.7, 0.8, 0.9, 1.0, 1.1) perovskite-type oxide as potential cathode for intermediate-temperature solid oxide fuel cells, International J. Hydrogen Energy 40 (2015) 11011 -11021.

[23] S.B. Adler, Limitations of charge-transfer models for mixed-conducting oxygen electrodes, Solid State Ionics 135 (2000) 603-612.

[24] S.B.Adler, J.A.Lane, B.C.H.Steele, Electrode kinetics of porous mixed‐conducting oxygen electrodes, J. Electrochemical Society 143(1996) 3554-3564.

[25] Z. Liu, L. Cheng, M. Han, A-site deficient $Ba_{1-x}Co_{0.7}Fe_{0.2}Ni_{0.1}O_{3-\delta}$ cathode for intermediate temperature SOFC, J. Power Sources 196 (2011) 868-871.

[26] C. Kuroda, K. Zheng, K. Swierczek, Characterization of novel $GdBa_{0.5}Sr_{0.5}Co_{2-x}Fe_xO_{5+\delta}$ perovskites for application in IT-SOFC cells, International J. Hydrogen Energy 38 (2013) 1027-1038.

[27] W. Zhou, R. Ran, Z. Shao, Progress in understanding and development of $Ba_{0.5}Sr_{0.5}Co_{0.8}Fe_{0.2}O_{3-\delta}$-based cathodes for intermediate-temperature solid-oxide fuel cells: A review, J. Power Sources 192 (2009) 231-246.

[28] A. Jun, J. Kim, J. Shin, G. Kim, Perovskite as a Cathode Material: A Review of its Role in Solid-Oxide Fuel Cell Technology, Chemelectrochem 3 (2016) 511-530.

[29] K. T. Lee, A. Manthiram, Comparison of $Ln_{0.6}Sr_{0.4}CoO_{3-\delta}$ (Ln= La, Pr, Nd, Sm, and

Gd) as cathode materials for intermediate temperature solid oxide fuel cells, J. Electrochem. Soc. 153 (2006) A794–A798.

Chapter 5 Effects of cobalt and iron proportions in $Pr_{0.4}Sr_{0.6}Co_{0.9-x}Fe_xNb_{0.1}O_{3-\delta}$ electrode material for symmetric solid oxide fuel cells

5.1 Introduction

Solid oxide fuel cells (SOFCs) can directly convert chemical energy to electric power with high efficiency, low pollution, and fuel flexibility [1, 2]. A typical SOFC consists of three parts: porous cathode and porous anode separated by dense solid electrolyte, in which O_2 is reduced to oxygen ions at the cathode, and then diffuse through the dense electrolyte towards the porous anode, and participate in the electrochemical fuel oxidation to generate water [3, 4]. As such, for an oxygen ions conducting electrolyte, it is necessary to develop porous cathode materials which can effectively convert O_2 molecule to oxygen ions and to find porous anode materials which can effectively convert H_2 molecule or hydrocarbon molecule to protons. Especially, as the hydrocarbon is used as the fuel, it is very important to avoid coking on the anode. However, it is always difficult to realize it by using the general anode materials. For example, Ni-based ceramics are the most commonly used anode materials, however, since hydrocarbon fuels are easily cracked on them and result in carbon deposition, such materials easily lose their activity, which will

reduce the cell performance. To solve this problem, one way is to develop electrode materials which can be used in either cathode or anode for the construction of symmetric solid oxide fuel cells (SSOFCs) [24]. As such, in the case of coke forming on the anode, the gas lines for the cathode and anode can be exchanged so that the coke is burnt out by oxygen and the electrode can be worked as the cathode continuously, and verse versa.

A favorable electrode material requires adequate mixed ionic-electronic conductivity [5, 6]. Perovskite oxide material plays an important role in SOFCs electrode since its property can be adjusted for some particular purposes by the introduction of different metal cations into its lattice and also exhibit high electrical conductivities [7]. ABO_3-type oxides with A-site element such as lanthanide (La), Strontium (Sr) and Barium (Ba) and the B-site element such as Mn, Fe, Ni and Co [8, 9]. For instance, $La_{1-x}Sr_xCo_{1-y}Fe_yO_{3-\delta}$ (LSCF) materials [10-12] have attracted much attention as the promising cathode material candidates of SOFCs. It derives from lanthanum strontium manganite (LSM) and herein, by replacing the Mn with Fe and Co in B-sites is found to be able to increase the oxygen exchange rate, and finally improve the whole cell performance. It is found that iron ion has higher chemical stability than cobalt ions with more favorable electrochemical activity and more suitable ion size in the B-site of perovskite. In addition, iron also has much lower price and wider availability than cobalt. Recently, a novel type of electrode

materials, i.e., $Pr_{1-x}Sr_xCo_yFe_{1-y}O_{3-\delta}$ (PSCF) have attracted great attention [13-18]. Ishihara et al. [19] found that A-site Pr-doped perovskite showed the highest electrical conductivity and the lowest over potential value as a resulting of Pr^{3+}/Pr^{4+} valence change. Moreover, as Niobium (Nb) was doped in the PSCF materials, the stability of the obtained PSCFN perovskite structures were improved [15]. Nagai et al. [20], and Zhang et al. [21] doped Molybdenum (Mo) to the B-site of PSCF in order to improve its performance. Meanwhile, Pr doped perovskite of $Pr_{0.7}Ca_{0.3}Cr_{1-y}Mn_yO_{3-\delta}$ (PCCM) was also used as the SSOFCs material, but it did not show a high performance [22]. Raj et al. found that the Pr replace A-site element could decrease the Mn oxidation state, making the material more likely to degradation under reduction conditions [23]. In addition, strontium based $SrTiO_{3-x}$, $SrCoO_{3-x}$, $SrFeO_{3-x}$ perovskite oxides were also used as the SSOFCs materials, in which various metals can be doped to enhance the stability and oxygen ion permeation. For instance, after investigated $Sr(Co_{0.9}X_{0.1})O_{3-\delta}$ (where X=Ni, Cu, Zn, Cr, Fe, Al, Ga, In, Ce, Ti, Zr, Sn, V and Nb) materials, it is found that the $SrCo_{0.9}Nb_{0.1}O_{3-\delta}$ has the best perovskite stability and the highest oxygen permeation. In addition, Radojkovic et al. [24] and Bartolomeo et al. [25] reported that $BaCe_{0.78}Nb_{0.12}Y_{0.1}O_{3-\delta}$ has higher stability than $BaCe_{0.9}Y_{0.1}O_{3-\delta}$. Moreover, it is confirmed that its chemical stability can be improved with the increase in Nb concentration.

$La_{0.75}Sr_{0.25}Cr_{0.5}Mn_{0.5}O_3$ (LSCM) was reported as a good alternative anode material to replace the traditional Ni-YSZ cermet [26, 27]. As the symmetric electrode material, however, it showed poor power density. For instance, the fabricated LSCM/YSZ/LSCM SSOFCs (YSZ: Yttria-stabilized zirconia) electrolyte only showed the maximum power density of 0.3 Wcm^{-2} at 900ºC [28]. After optimizing the microstructure of LSCM, a maximum power density of 0.5 Wcm^{-2} at 950 ºC was obtained [29]. Zhu et al. [30] added a small amount of Sm-doped CeO_2 (SDC) and 6 wt. % Ni in 32 wt. % LSCM impregnated YSZ, respectively and used them as the symmetric electrode materials. As a result, the maximum power densities of 0.559 and 0.547 Wcm^{-2} were achieved respectively. Meanwhile, the increase of Sr amount seems to have no enhancement function on the power density. For instance, Martinez-Coronado et al. [31] used $La_{0.5}Sr_{0.5}Co_{0.5}Ti_{0.5}O_{3-\delta}$ (LSCT) as the symmetrical electrode material, but only a maximum power density of 0.11 W cm^{-2} was obtained. Chen et al. [32] used Sr-rich $La_{0.3}Sr_{0.7}Fe_{1-x}Cr_xO_{3-\delta}$ (LSFCx, x=0-0.3) as the symmetrical electrode material, but the maximum power density of only about 0.3 W cm^{-2} at 800 ºC in wet H_2 for the $LSFC_{0.3}$ material was achieved. In addition, Ding et al. [33] reported two types of $La_{0.6}Ca_{0.4}Fe_{0.8}Ni_{0.2}O_{3-\delta}$-$30Sm_{0.2}Ce_{0.8}O_{1.9}$ symmetrical electrode materials prepared by the physical mixing and infiltration, respectively, and the obtained maximum power densities at 800 ºC were also not so high, i.e., only 0.140 and

0.279 W cm^{-2}, respectively.

In this study, a novel family of $Pr_{0.4}Sr_{0.6}Co_{0.9-x}Fe_xNb_{0.1}O_{3-\delta}$(x=0, 0.2, 0.4, 0.6 and 0.9) ceramics was synthesized and used as the symmetric electrode materials. Mainly, the effects of stoichiometric amount of iron and cobalt on the electrical conductivity, thermal expansion and electrochemical properties were investigated. It is expected to find the optimum proportion of Fe and Co so that the obtained PSCFxN materials have high symmetric cell performance.

5.2 Experimental

5.2.1 Materials preparation and cell fabrication

$Pr_{0.4}Sr_{0.6}Co_{0.9-x}Fe_xNb_{0.1}O_{3-\delta}$ ($PSCF_xN$) (x=0, 0.2, 0.4, 0.6 and 0.9) perovskite oxides were prepared by using the solid-state reaction method, in which the chemicals with high purity, i.e., $Pr(NO_3)_3 \cdot 6H_2O$, $SrCO_3$, $Co(NO_3)_2 \cdot 6H_2O$, Fe_2O_3 and Nb_2O_5 (all with 99.9% purity, Wako, Japan), were used. The stoichiometric amounts of these chemicals were completely mixed by the ball milling for 10 h at first, and then calcined in air. Based on the preliminary experiments, it was found that the pure phase was obtained when the mixed powders were calcined at 1100 °C for 7 h in air. Finally, the obtained powder with pure phase was treated by ball-milling for 3 h again. For the electrical conductivity test

and thermomechanical analysis, the finely ground oxide powders were pressed into bar sunder a uniaxial pressure at 100 MPa at first and then, sintered at 1200 ºC for 10 h in air at a heating rate of 3 ºC min^{-1} for the conductivity test. The commercially available powder of $La_{0.8}Sr_{0.2}Ga_{0.8}Mg_{0.2}O_{3-\delta}$ (LSGM, 99.9% FCM, USA) was used for the preparation of electrolyte. Dense LSGM pellets with 20 mm in diameter were prepared by pressing the LSGM powders at 220 MPa and then sintered at1450 ºC for 10 h in air. Symmetrical cells of PSCFN/LSGM/PSCFN for impedance andcell performance studies were prepared by slurry coating method. In brief, the PSCFN slurry was coated on the both sides of the dense LSGM electrolyte pellet and then calcined at 1300 ℃ for 2 h. For the cell performance testing, the cell was sealed on an alumina tube using a Pyrex glass ring.

5.2.2 Material characterizations

Crystallographic phases of the PSCFN powders were determined using a RIGAKU Smartlab X-ray diffractometer with a CuKα radiation (λ=0.154 nm) generated at 45 kV and 200 mA. The conductivities of sintered $PSCF_xN$ bars at different temperatures were measured by a four-terminal DC method in air by ascending the temperature ranging from 100 to 900 ºC, with an interval of 50 ºC and a dwell of 10 min at each temperature before

the conductivities were measured to allow the system to equilibrate. The composition and valence of each element on the surface of fresh powder were determined by X-ray photoelectron spectroscopy (XPS, AXIS ULTRA DLD, Japan). The thermal expansion coefficients (TECs) were measured between 20 and 900 ^{o}C using a dilatometer (TMA Instruments, Thermo plus EVO2).

Electrochemical measurements were performed using a symmetrical cell for both polarization resistance and cell performanc etest in the temperature range of 750-900 ^{o}C. Electrochemical impedance spectra (EIS) of the half-cell were recorded at the open circuit voltage(OCV) over the frequency range of 0.01 Hz-1 MHz with the ACsignal amplitude of 10 mV using a frequency response analyzer and a potentiostat (Solartron 1255B and 1287, respectively). The impedance responses were analyzed using the equivalent resistor-capacitor (RC) circuit method. For the symmetrical cell performance test, the anode side was firstly annealed at 900 ^{o}C in dry H_2 for 1 h, and then the test was performed with humidified H_2(3%H_2O) flow rate of 50 cm^3 min^{-1}. Air was used inthe cathode side as the oxidant with a flow rate of 50 cm^3 min^{-1}.Electronic contacts were realized by using a Pt mesh with Au paste. The impedance of the single cell after the cell performance test was measured at the OCV state using the same method.

5.3 Results and discussion

5.3.1 Crystal structure and chemical compatibility

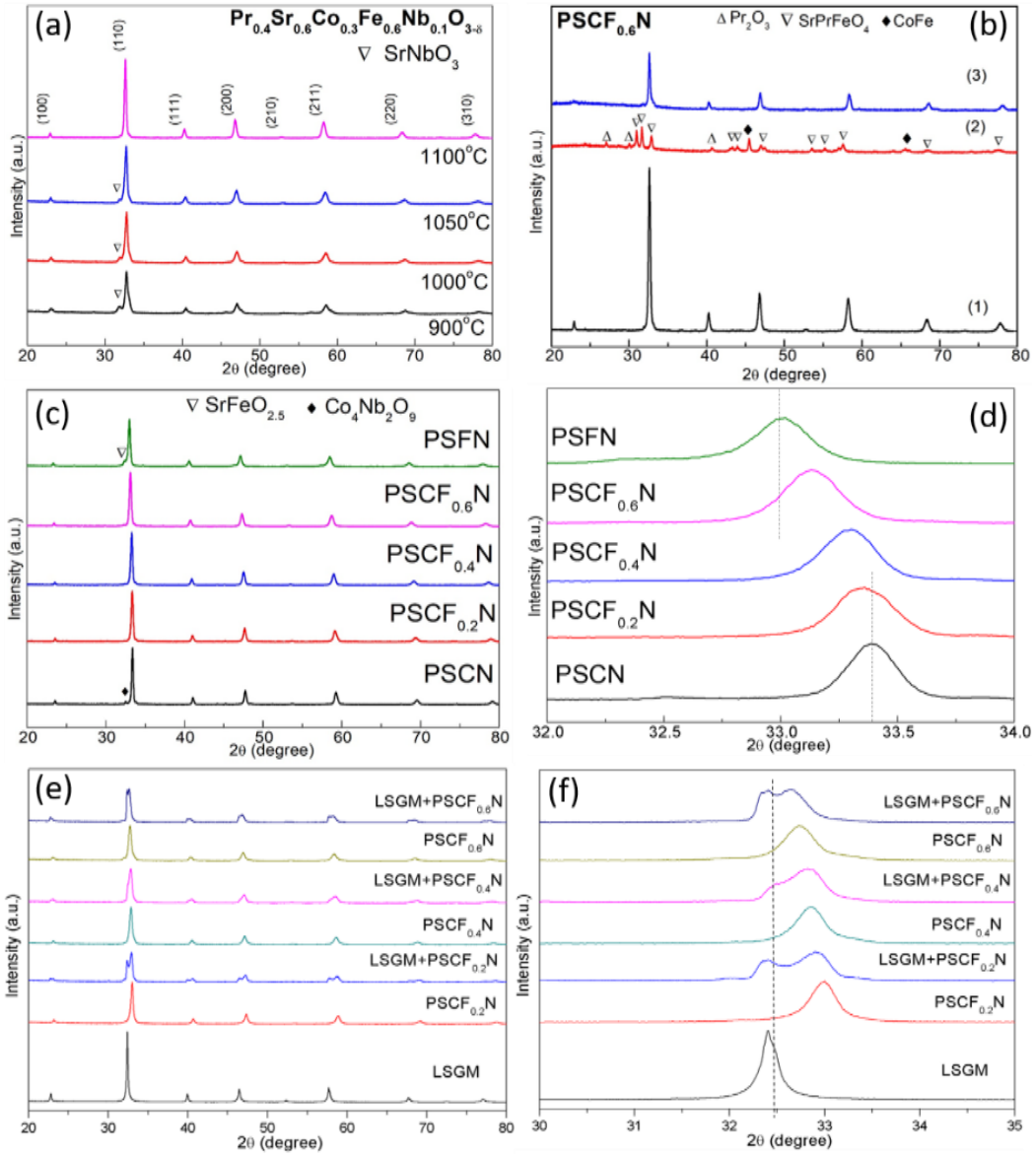

Figure 5.1 (a) XRD patterns of $PSCF_{0.6}N$ powders after the calcinations at different temperatures for 7 h. (b) (1) $PSCF_{0.6}N$ calcined at 1100 ºC in air for 7 h, (2) $PSCF_{0.6}N$ reduced at 1000 ºC in H_2 for 3 h, (3) reduced $PSCF_{0.6}N$ oxidized at 1000 ºC in air for 3 h after (2). (c)XRD patterns of PSCFxN perovskites (x=0, 0.2, 0.4, 0.6 and 0.9) calcined in air at 1100 ºC for 7 h. (d) Magnified XRD patterns of (c) in the range of $32.0° \leq 2\theta \leq 34.0°$.

(e) XRD patterns of PSCFN, LSGM and their mixed PSCFN-LSGM powder after calcined at 1300 ^{o}C for 8 h in air. (f) Magnified XRD patterns of (e) in the range of $30.0° \leq 2\theta \leq 35.0°$.

Fig. 5.1(a) shows XRD patterns of the synthesized $PSCF_{0.6}N$ powders calcined in air at 900 ^{o}C, 1000 ^{o}C, 1050 ^{o}C and 1100 ^{o}C for 7 h, respectively. One can see that the impurity phase at 31.9^{o} corresponding to $Sr_4Nb_{17}O_{26}$ (PDF: #45-0583) obviously existed for the sample calcined at 900 ^{o}C, and with the further increase in the calcined temperature, the impurity phase gradually disappeared, finally the sample became to pure phase as the calcined temperature was over 1100 ^{o}C, and the crystallinity also increased until the pure cubic structure appeared [34]. As a most important requirement for SSOFCs materials, they should have redox stability in hydrogen and air atmospheres. Thus, in order to evaluate the phase stability of $PSCF_{0.6}N$ in both anode and cathode atmospheres, the synthesized $PSCF_{0.6}N$ powders were treated in H_2 atmosphere at 1000 ^{o}C for 3 h at first. After XRD measurement, the powders were further oxidized in air at 1000 ^{o}C for 3 h. As shown in in Fig. 5.1 (b), one can see that the main peak was transformed from Pm/3m space group to I4/m space group (Fig. 5.1(b)-(2), with $SrPrFeO_4$ phase (PDF: #32-1237)) after H_2 treatment, and then the structure was transferred back to the pure cubic Pm/3m structure after oxidization it in air at 1000 ^{o}C (Fig. 5.1(b)-(3)). Thus, the obtained

$PSCF_{0.6}N$ powders should have redox stability in hydrogen and air atmospheres.

Figs.5.1 (c), and (d) show the change of XRD pattern with the increase in Fe species amount. Herein, PSCFxN (x=0, 0.2, 0.4, 0.6 and 0.9) powders were calcined at 1100 ^{o}C for 7 h. One can see that the powders with $0.2 \leq x \leq 0.6$ had pure phase. In comparison, in the case of x=0 and 0.9, the impurity phases defined as $Co_4Nb_2O_9$ (PDF:#38-1457) and $SrFeO_{2.5}$ (PDF:#17-0932) were observed at $2\theta=32.2°$ and 31.8°, respectively, indicating that the proportion of Fe in $PSCF_xN$ had great effect on the purity of final product. Moreover, as shown in Fig.5.1 (d), the main diffraction peaks of the $PSCF_xN$ perovskites gradually shifted to the lower values of 2θ with the increase in the concentration of Fe (x). It indicated that the Fe cations were successfully incorporated into the lattice of PSCN perovskite. Herein, the ionic radius of Fe^{4+} (58.5 pm) is larger than that of Co^{4+} (53 pm), which could weaken the B-O-B bond in B-sites, leading to the lattice expansion.

To examine the chemical compatibility between cathode and electrolyte materials, XRD pattern of the mixed PSCFN-LSGM powder calcined at 1300 ^{o}C for 8 h in air was also measured. As shown in Fig. 5.1(e), no impurity phase was observed although the main peak shifted to some extent. Especially, the peaks related to LSGM had no any change. Moreover, as indicated in Fig. 5.1 (f), the peaks corresponding to PSCFN and LSGM were individually found, indicating that no reaction occurred between PSCFN and

LSGM even at a temperature as high as 1300 °C. Thus, the electrode and electrolyte materials in this study were chemically compatible.

5.3.2 Electrical conductivity

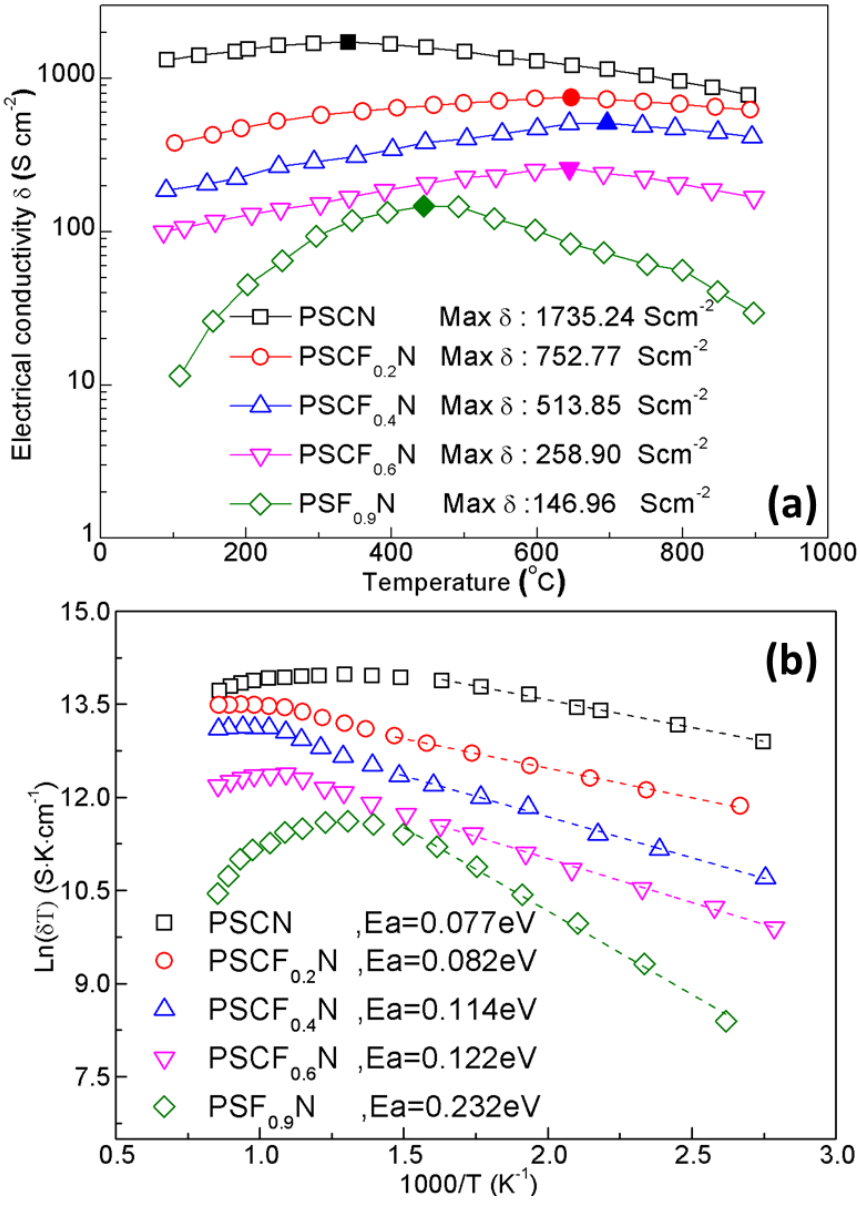

Figure 5.2 (a) Electrical conductivities and (b) corresponding Arrhenius plots of the PSCFxN (x=0, 0.2, 0.4, 0.6 and 0.9) bars in air.

Fig. 5.2(a) shows the electrical conductivities of $PSCF_xN$ (x=0, 0.2, 0.4, 0.6 and 0.9) samples measured in air. All the electrical conductivity increased at first and then decreased by further elevating the temperature over a transition temperature (T_s), which obviously exhibited a P-type semiconducting behavior. Herein, it is considered that these materials followed the small polaron hopping mechanism before T_s, in which the electron holes acted as the charge carriers. [14, 35-36]. However, over the T_s, the oxygen in the perovskite lost and oxygen vacancies were formed by decoupling of the d-orbitals of the transition metals and the p-orbitals of oxygen. Herein, with the doping of Fe species, as indicated in Fig. 5.4 in the section 5.3.4, parts of Fe^{4+} could be reduced to Fe^{3+} by other high valence metal ions such as Nb^{5+} in order to maintain the electrical neutrality [37]. As such, the hopping hole between Fe^{3+} and Fe^{4+} should be benefit for the generation of oxygen vacancies. In addition, it can be seen that the electrical conductivity was sensitively affected by the Fe doping and PSCN without Fe doping showed the highest conductivity values in the whole temperature range and the conductivity decreased by increasing the concentration of Fe doping from 0.2 to 0.9. Herein, as shown in Fig. 5.3, the cross section images of bars for the conductivity were similar to those used in the fabrication of SOFC test cells (Fig. 5.6). Meanwhile, the cobalt on the B-side may change the defect formation and charge compensation mechanisms, thus altering the electrical

conduction behavior.

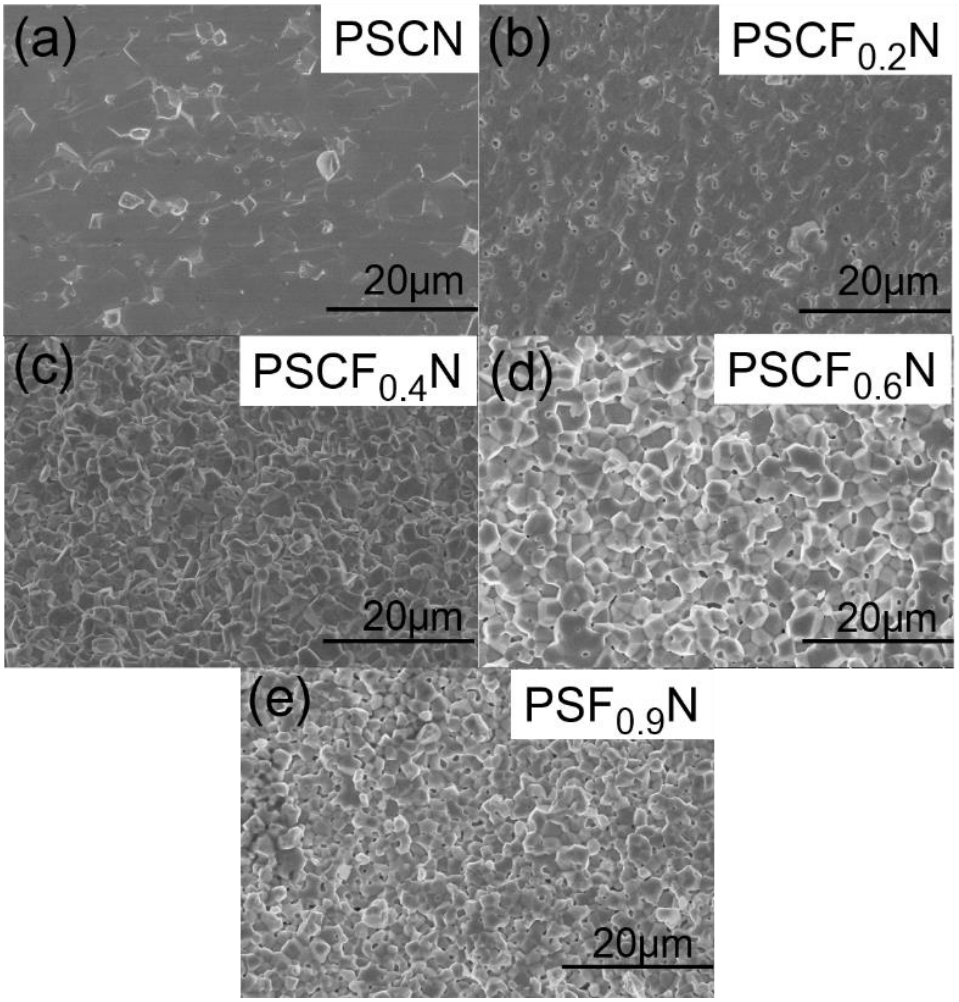

Figure 5.3 Cross section images of the electrode material bars for conductivity tests: (a) PSCN, (b) $PSCF_{0.2}N$, (c) $PSCF_{0.4}N$, (d) $PSCF_{0.6}N$ and (e) $PSF_{0.9}N$

For the Fe doped PSCN, Fe^{4+} /Co^{4+} should be reduced to Fe^{3+}/Co^{3+} in order to maintain the electrical neutrality. In this case, the oxygen vacancies could be increased by reducing Fe^{4+} to Fe^{3+} as described in the follows:

$$2Fe_{Fe}^{\bullet} + O_O^{\times} \rightarrow 2Fe_{Fe}^{\times} + V_O^{\bullet\bullet} + \frac{1}{2}O_2 \quad (1)$$

where $O_O^{\times}$ is the lattice oxygen, $V_O^{\bullet\bullet}$ is the oxygen vacancy, $Fe_{Fe}^{\bullet}$ and $Fe_{Fe}^{\times}$ represent Fe^{4+} and Fe^{3+}, respectively. It is considered that the increase in oxygen vacancies could improve the oxygen reduction reaction rate. From Fig. 5.2(b), a linear relationship was observed at the low temperature range, which could be illustrated by the small polaron conduction mechanism, following eq. (2): [14]

$$\sigma=\frac{C}{T}\exp(\frac{-Ea}{kT}) \quad (2)$$

where C is the pre-exponential constant related to the carrier concentration as well as other properties of the material, T is the absolute temperature, k is the Boltzmann's constant and Ea is the activation energy. The lower Ea indicates the higher catalytic activity of oxygen reduction reaction (ORR). From Fig. 5.2(b), one can see that the doping of Fe resulted in the increase of activation energy, indicating the decrease of catalytic activity. Herein, the Ea values, which calculated from the slopes of the Arrhenius plots were 0.077, 0.082, 0.114, 0.122, 0.232 eV for the PSCN, $PSCF_{0.2}N$, $PSCF_{0.4}N$, $PSCF_{0.6}N$ and PSFN materials, respectively. That is, along with the iron concentration increasing, the Ea value increased. Moreover, compared with those reported materials using as the symmetrical electrodes $La_{0.8}Sr_{0.2}Sc_{0.2}Mn_{0.8}O_{3-\sigma}$ [38], $La_{0.8}Sr_{0.2}Cr_{0.5}Mn_{0.5}O_{3-\sigma}$ [38] and $(Pr_{0.4})_xSr_{0.6}Co_{0.2}Fe_{0.7}Nb_{0.1}O_{3-\delta}$ (P_xSCFN) [39] with electrical conductivities of 45, 24 and 116 Scm^{-1} respectively at 850 °C, the present $PSCF_{0.6}N$ material had higher electrical

conductivity of 180 Scm^{-1} at the same temperature. In addition, the activation energy (0.122 eV) of $PSCF_{0.6}N$ was also lower than those of reported materials such as $La_{0.7}Ca_{0.3}Cr_{0.8}Mn_{0.2}O_{3-\sigma}$ (0.31 eV) [40], $La_{0.7}Ca_{0.3}Cr_{0.8}Ni_{0.2}O_{3-\sigma}$ (0.34 eV) [40], and $La_{0.6}Ce_{0.1}Sr_{0.3}Fe_{0.9}Ni_{0.1}O_{3-\sigma}$ (0.16 eV) [41].

5.3.3 Thermal expansion behavior

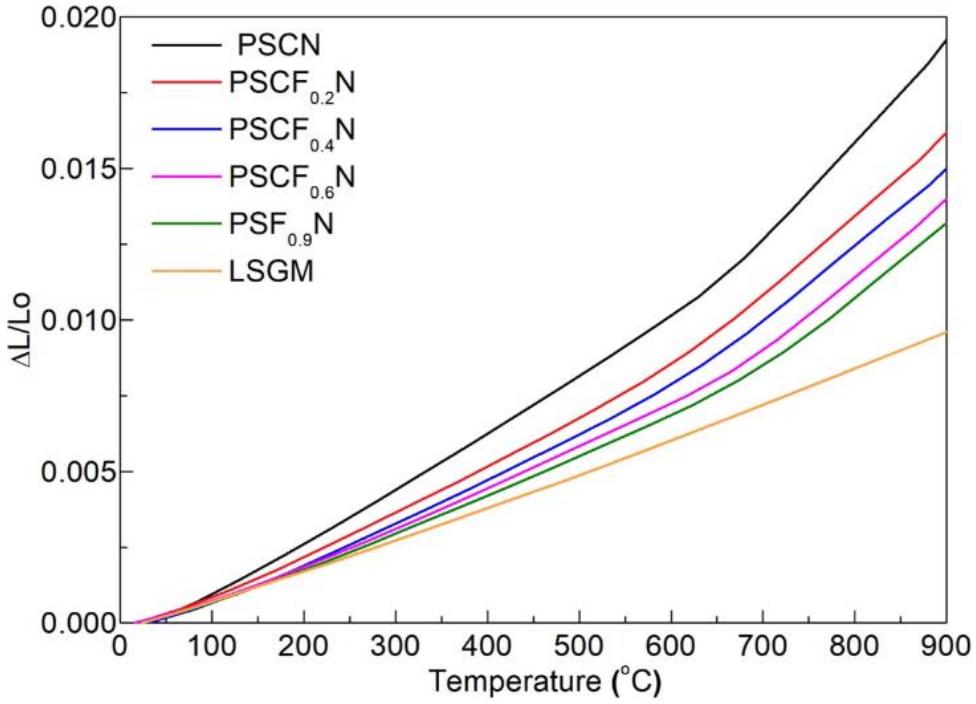

Figure 5.4 Thermal expansion curves of $PSCF_xN$ (x=0, 0.2, 0.4, 0.6 and 0.9) and LSGM in a temperature range from RT to 900 °C in air.

It is necessary to consider the thermal expansion coefficients (TEC) of the electrode and electrolyte during the fabrication of SOFC since the mismatch of TECs between them could result in the thermal stress, leading to the degradation of the performance [37, 38].

Cobalt-rich materials usually have higher TECs, and it is found that doping Fe could reduce it but not affect the conductivity obviously [39]. Figure 5.4 shows the thermal expansion curves related to the $PSCF_xN$ (x=0-0.9) bars in the temperature range from RT to 900 ºC. One can see that the △L/Lo value significantly decreased (Herein, △L is change in length of a rod due to thermal expansion from the initial Lo) with the increasing of the Fe doping amount. In the case of cobalt free (PSFN), the curve was closest to that of the LSGM electrolyte. The average TECs of $PSCF_xN$ (x=0-0.9) perovskite oxides were 17.39, 14.01, 13.31, 11.79 and 11.45×10^{-6} K^{-1} for x=0, 0.2, 0.4, 0.6 and 0.9, respectively. Obviously, these average TEC values were lower than those reported materials such as P_xSCFN ($18.02\text{-}18.70\times10^{-6}K^{-1}$) [34] and $Pr_{1-x}Sr_xCo_{0.8}Fe_{0.2}O_{3-\delta}$ ($19.7\text{-}21.23\times10^{-6}K^{-1}$) [40], which should be benefit for the fabrication of SOFCs.

5.3.4 XPS analysis

Surface compositions and elemental states of the prepared PSCFxN perovskite oxides were characterized by using XPS technique. Herein, to describe the different features of the different PSCFxN samples, the related Co 2p, Fe 2p and O 1s core-level XPS spectra were analyzed in the following.

Fig. 5.5 (a) shows XPS spectra and fitting lines corresponding to O 1s in PSCFxN

(x=0, 0.2, 0.4, 0.6 and 0.9). One can see that two clearly peaks centered at around 528.5 eV (lower bonding energy (LBE)) and 531.5 eV (higher bonding energy (HBE)) and an inconspicuous peak at around 533.5 eV attributed to H2O molecules adsorbed on the material surface existed for all samples. Herein, the LBE should be attributed to the surface lattice oxygen of the PSCFxN perovskite, and with the increase in the Fe doping amount, the surface oxidation state should be changed, which could change the environment around the O atoms, and affect LBE. As shown in Table 1, with the increase in Fe doping amount, the percentage of Olattice area increased, indicating the increase in oxygen vacancy amount. Herein, the lattice oxygen should be easily lost at high temperature to form oxygen vacancy.

Table 5.1 The area percentages of three forms of oxygen based on the O 1s fittings for $PSCF_xN$ (x=0, 0.2, 0.4, 0.6 and 0.9) samples.

	$O_{lattice}$ (%)	O_{ads} (%)	H_2O_{ads} (%)
PSCN	37.85	56.20	6.45
$PSCF_{0.2}N$	41.11	56.04	2.84
$PSCF_{0.4}N$	43.37	49.06	7.47
$PSCF_{0.6}N$	47.70	48.59	3.72
$PSF_{0.9}N$	44.46	52.11	3.43

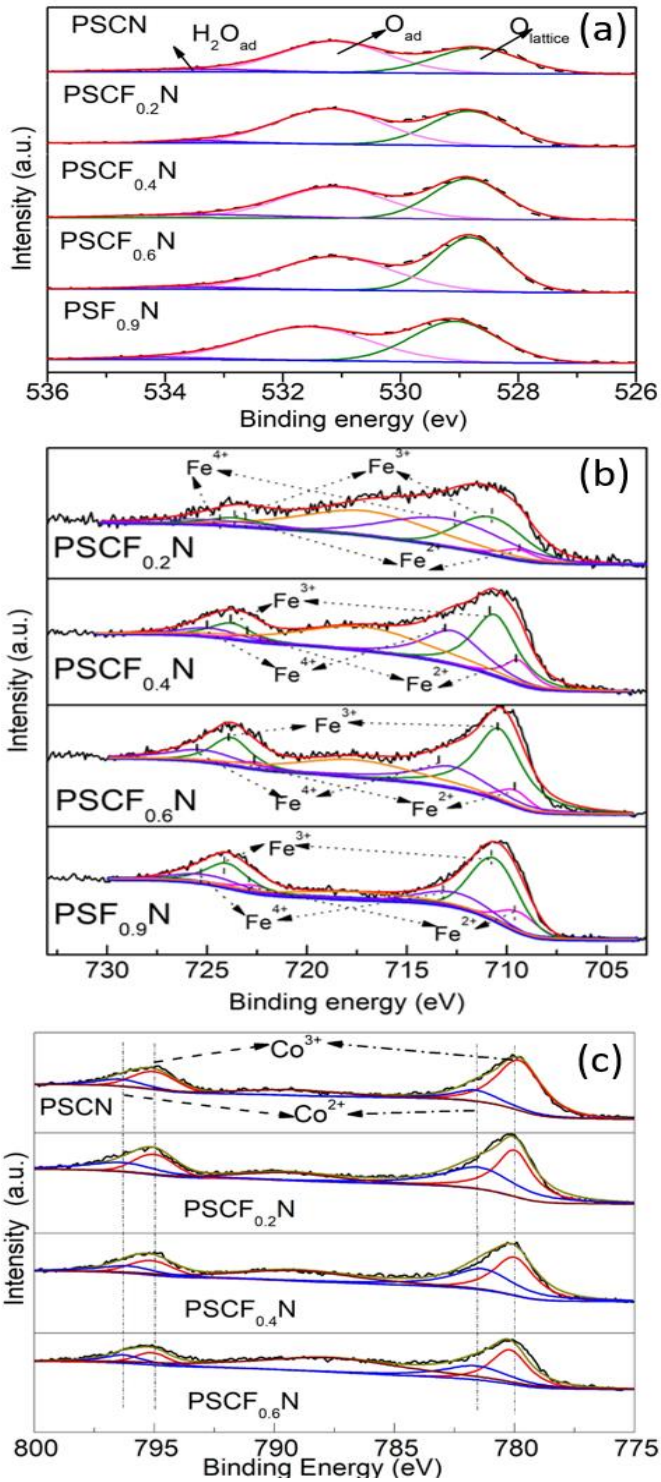

Figure 5.5 (a) XPS spectra and fitting lines corresponding to O 1s in $PSCF_xN$ (x=0, 0.2, 0.4, 0.6 and 0.9), XPS spectra of (b) Fe 2p in $PSCF_xN$ (x= 0.2, 0.4, 0.6 and 0.9) and (c) Co 2p in $PSCF_xN$ (x=0, 0.2, 0.4 and 0.6).

Meanwhile, the HBE corresponded to the active oxygen species adsorbed or activated on the surface， which also indicated by other researchers[18]. Herein, the active oxygen species are weakly bonded to the crystal lattice and can be easily released as molecular oxygen between 200-500 ^{o}C [55]. In general, oxygen could be transformed on the $PSCF_xN$ perovskite oxide as follows [46]:

$$o_2 \xrightarrow{+e^-} o_2^- \xrightarrow{+e^-} o_2^{2-} \leftrightarrow 2o^- \xrightarrow{+2e^-} 2o^{2-} \quad (3)$$

Herein, the formation of the state of O^{2-} is important for the oxygen species transferring in the $PSCF_xN$ perovskite oxide. As stated above, Fe doping could increase the lattice oxygen, which is benefit to the formation of oxygen vacancy, and enhance the transformation of the adsorbed oxygen molecules to the state of O^{2-}.

Figs. 5.5(b) and (c) show Fe 2p and Co 2p XPS spectra of $PSCF_xN$ (x= 0.2, 0.4, 0.6 and 0.9), respectively. Both of them showed a doublet, i.e., $2p_{3/2}$ and $2p_{1/2}$. As shown in Fig. 4(b), the Fe 2p signals enveloped the signals from Fe^{2+}, Fe^{3+} and Fe^{4+}, where $Fe^{2+}(2p_{3/2}/2p_{1/2})$, Fe^{3+} $(2p_{3/2}/2p_{1/2})$ and $Fe^{4+}(2p_{3/2}/2p_{1/2})$ located at 709.4-709.7/722.6-723.0 eV, 710.6-711.0/723.8-724.1 eV, and 712.6-712.8 /724.9-725.4 eV, respectively. These fitting results were in agreement with those reported by Pan *et al.* [47], Lu *et al.* [48] and Yamashita *et al.* [49]. Meanwhile, the satellite peak around 718 eV should be also assigned to Fe^{3+}. In the perovskite oxide, the removal of an oxygen atom from the

lattice to form an oxygen vacancy could result in the breaking of the electronic interactions of the oxygen atom with the neighboring‘A’ and ‘B’ site atoms. For example, the removal of a neutral oxygen atom from a B-O bond leaves the electron cloud of B free to redistribute across the nearby atoms. As such, not only the B site elements change their oxidation states, but also the nearby oxygen atoms and ‘A’ site elements could share the electron cloud by the inductive effect. From Fig. 5.5(b), one can see that Fe^{4+} species decreased but Fe^{3+} species increased with the increase in Fe doping amount, indicating that Fe^{4+} is easily reduced to Fe^{3+} in the case of high Fe doping amount. As x= 0.6, the maximum Fe^{3+} peak after the curve fitting was obtained. Meanwhile, for Co 2p XPS spectra (Fig. 5.5(c)), the peaks corresponded to Co^{3+} ($2p_{3/2}$/$2p_{1/2}$) and Co^{2+} ($2p_{3/2}$/$2p_{1/2}$) located at 780.0-780.2/795.2-795.5eV and 781.2-781.4/796.7-797.1eV, respectively. One can see that Co^{3+} was the main Co species in these materials.

5.3.5 Electrochemical impedance spectra

Electrochemical activities of PSCFxN electrode for oxygen reduction and electrochemical impedance spectroscopy (EIS) for a symmetric cell of PSCFN/LSGM/PSCFN with ~0.5 mm thickness of LSGM electrolyte were investigated in a temperature range of 750-900 ºC in air. Herein, the ohmic resistance is mainly

contributed by the electrolyte, and Nyquist plots can be characterized by two equivalent circuit separable arcs over the full frequency range. The high-frequency arc (RHF), specifically observed from the mid frequency (10^3-10^2 Hz), corresponds to the ion charge transport resistance [50]; and the low-frequency (10^1-10^{-1} Hz) arc (RLF) represents the surface diffusion of oxygen species including the oxygen adsorption and dissociation processes [51]. Meanwhile, the total polarization resistance (Rp) is estimated from the sum of R_{HF} and $R_{LF.}$

Fig. 5.6(a) shows the SEM image of symmetric cell $PSCF_{0.6}N$/LSGM/$PSCF_{0.6}N$ after electrical impedance test. It is obvious that $PSCF_{0.6}N$ had high porosity and good connection with the electrolyte. Fig. 5.6(b) shows the electron transfer process, in which the Au paste layer between the electrode material and current collector will enhance the electron transfer and current collection. Figs. 5.6 (c) and (d) illustrate the oxygen molecules adsorption on the electrode material, transforming to the oxygen ions and transferring in the material. This is a key step during the SOFC working. That is, oxygen adsorbed on the surface of electrode will be reduced to O^{2-} and form electron holes (Fig. 5.6(d)). Meanwhile, the structural defects caused by the oxygen desorption will result in the charge moving. The adsorbed species could be weakly bond to the lattice oxygen and easily transported to leave oxygen vacancies for the subsequent adsorptions.

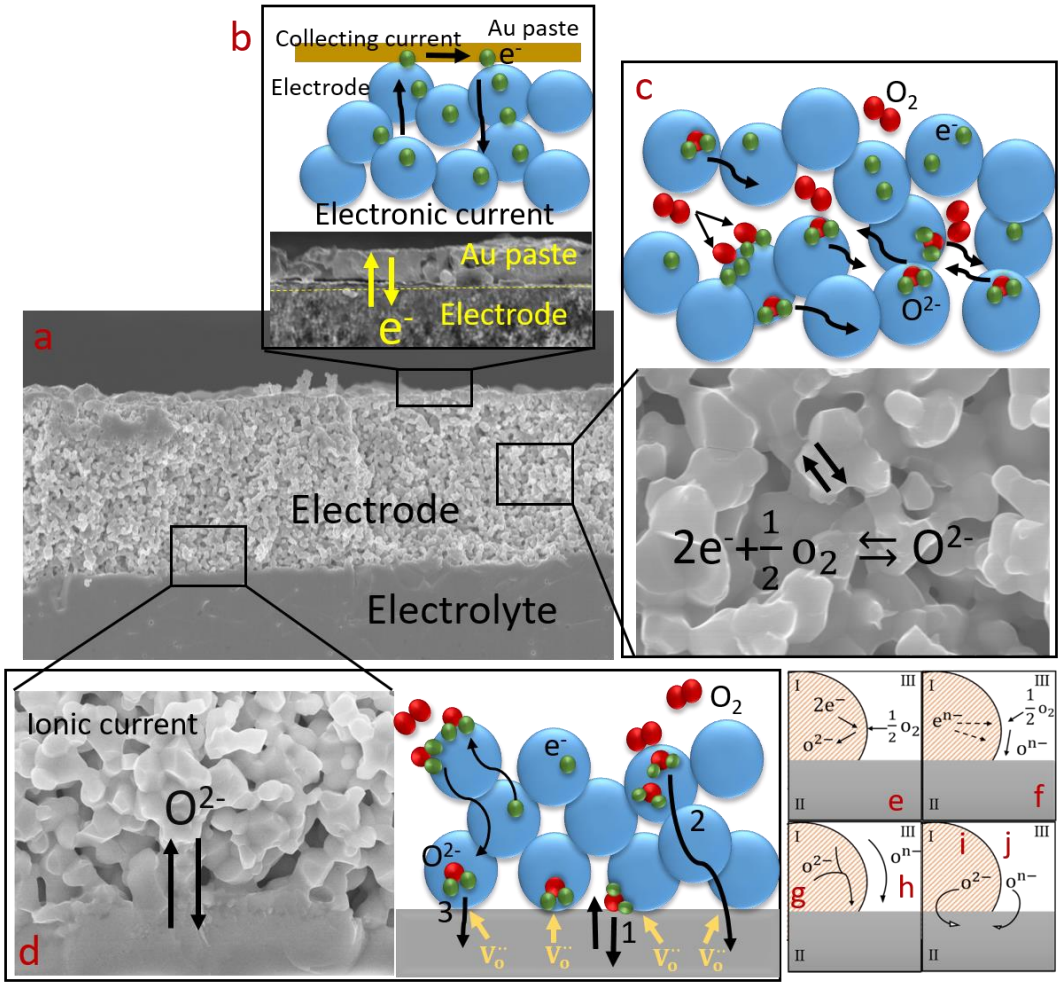

Figure 5.6 (a) SEM image of $PSCF_{0.6}N$ symmetric cell after electrical impedance test; (b) Schematic diagram and SEM image of Au paste and electrode connecting part; (c) Schematic diagram and SEM image of electrode porosity area; (d) Schematic diagram and SEM image of electrolyte and electrode connecting part; (e-j) mechanisms thought to governing oxygen reduction in SOFC (I, II, and III refer to the electronic phase, ionic phase and gas phase, respectively.)

As such, the ion transfer occurs by the incorporation of O^{2-} into the vacancy accompanying with the generation of another electron hole. Thus, the reaction mechanism

for oxygen reduction was proposed as follows [52]:

① $O_{2(g)} \rightarrow 2O_{ad}$

② $O_{ad} + e^{-} \rightarrow {O_{ad}}^{-}$

③ ${O_{ad}}^{-} \rightarrow {O_{TPB}}^{-}$

④ ${O_{TPB}}^{-} + e^{-} \rightarrow {O_{TPB}}^{2-}$

⑤ ${O_{TPB}}^{2-} + V_O^{\bullet\bullet} \rightarrow {O_O}^{x}$

Actually, this process can be summarized by eq. (3), and illustrated in Figs. 5.6(e-j). That is, oxygen molecule enters into the bulk of the electrode material (e) or, adsorbs on the surface of the electronic phase to be partially reduced (f). Furthermore, the bulk/surface transportation of O^{2-} or O^{n-} to the Ⅰ/Ⅱ interface ((g)/ (h) occurs with the electrochemical charge transfer of O^{2-} across the Ⅰ/Ⅱ interface (i), and combinations of O^{n-} and e^{-} across the Ⅰ/Ⅱ interface (j) [53].

As shown in Figs. 5.7(a)-(e), the R_p value decreased with the increase in the operating temperature for each $PSCF_xN$ perovskite oxide, indicating that the temperature had great effect on the oxygen reduction kinetics. Herein, the difference of intercepts with the real axis between high frequency and low frequency corresponded to the polarization resistance of the symmetric cell electrode/electrolyte interface.

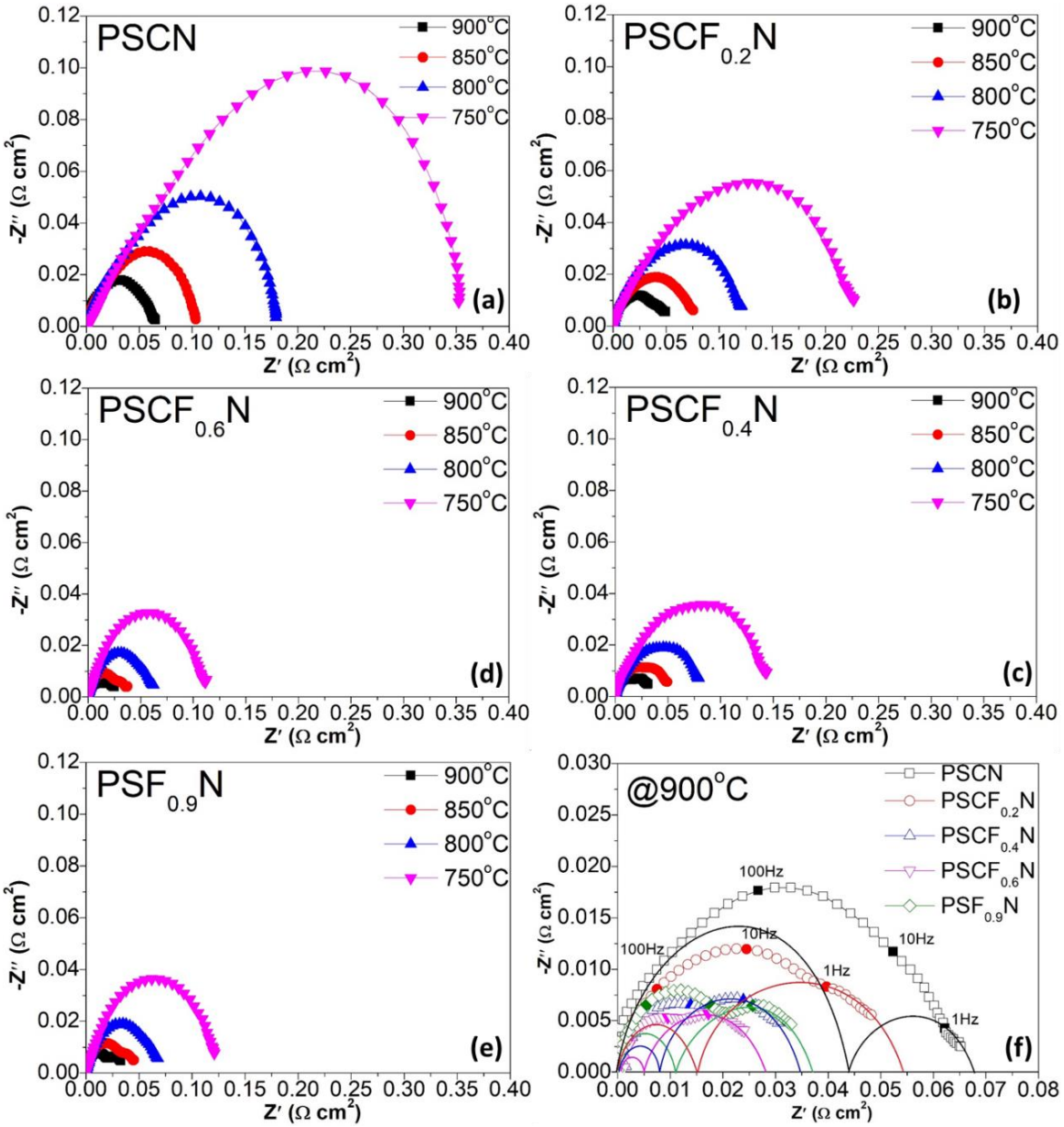

Figure 5.7 Nyquist plots of impedance spectra for (a) PSCN, (b) $PSCF_{0.2}N$, (c) $PSCF_{0.4}N$, (d) $PSCF_{0.6}N$, (e) $PSF_{0.9}N$ and (f) polarization resistances at 900 °C.

Fig. 5.7(f) clearly shows the polarization resistances of the $PSCF_xN$ perovskite oxides with different proportions. Herein, the high frequency (10^3-10^2 Hz) arc (R_{HF}) is usually related to the charge-transfer resistance, and the low frequency (10^1-10^{-1} Hz) arc

(R_{LF}) is related to the mass-transfer. As shown in Fig. 5.7(f), the R_{HF} of $PSCF_xN$ with the Fe doping was lower than R_{LF}, indicating that the higher oxygen vacancy concentration can assist the bulk oxygen ion transfer. Meanwhile, one can see that the R_p value decreased significantly after the Fe doping. It indicates that Fe doping enhanced the oxygen ion transfer and promoted the activity of oxygen on the surface.

Table 5.2 Polarization resistance results of $PSCF_xN$ materials as the symmetric electrode at 750-900 °C temperature range in air.

	900 °C			850 °C	800 °C	750 °C
	Rp (Ω cm^2)	R_{HF} (Ω cm^2)	R_{LF} (Ω cm^2)	Rp (Ω cm^2)	Rp (Ω cm^2)	Rp (Ω cm^2)
PSCN	0.068	0.044	0.024	0.105	0.177	0.352
$PSCF_{0.2}N$	0.054	0.015	0.039	0.085	0.125	0.230
$PSCF_{0.4}N$	0.035	0.008	0.027	0.055	0.080	0.150
$PSCF_{0.6}N$	0.028	0.005	0.022	0.042	0.068	0.113
$PSF_{0.9}N$	0.038	0.012	0.026	0.052	0.070	0.120

In this study, as summarized in Table 5.2, as x=0.6, the minimum R_p value was obtained at each operating temperature. In the Fig. 5.7(f), the marked 1 Hz and 10 Hz points belonged to R_{LF} and the marked 100 Hz belonged to R_{HF}. It is obvious that the marked 100 Hz point closed to the axes along with Fe increasing, and the main decrease of the resistance occurred in the high frequency range, further indicating that the increase

of oxygen vacancy with the increase in Fe amount enhanced the bulk oxygen ion transfer. These results are consistent with the XPS results as discussed above.

Table 5.3 Polarization resistance results of $PSCF_xN$ materials as the symmetric electrode at 750-900 ^oC temperature range in H_2 (3% H_2O).

	900 ^oC Rp (Ω cm^2)	850 ^oC Rp (Ω cm^2)	800 ^oC Rp (Ω cm^2)	750 ^oC Rp (Ω cm^2)
PSCN	0.134	0.253	0.476	0.721
$PSCF_{0.2}N$	0.131	0.219	0.409	0.677
$PSCF_{0.4}N$	0.115	0.181	0.313	0.579
$PSCF_{0.6}N$	0.077	0.165	0.275	0.513
$PSF_{0.9}N$	0.123	0.201	0.380	0.653

Fig. 8 shows the specific resistances of $PSCF_xN$ measured in H_2 (3% H_2O) at different temperatures. One can see that R_p value for $PSCF_xN$ in H_2 atmosphere decreased with the increase in temperature. As summarized in Table 3, similar as the measured results in air, the R_p value also decreased with the increase of Fe doping amount until a minimum R_p value was achieved for the $PSCF_{0.6}N$. In the Nyquist plots of impedance spectra, two arcs were observed. The first arc in the range of high frequency related to the hydrogen reduction ability of the materials, and the other semicircle should be resulted from the gas bulk diffusion ability. Herein, since the $PSCF_{0.6}N$ showed the lowest specific resistance with the highest redox property, it was used to fabricate symmetric SOFC for the further

investigations.

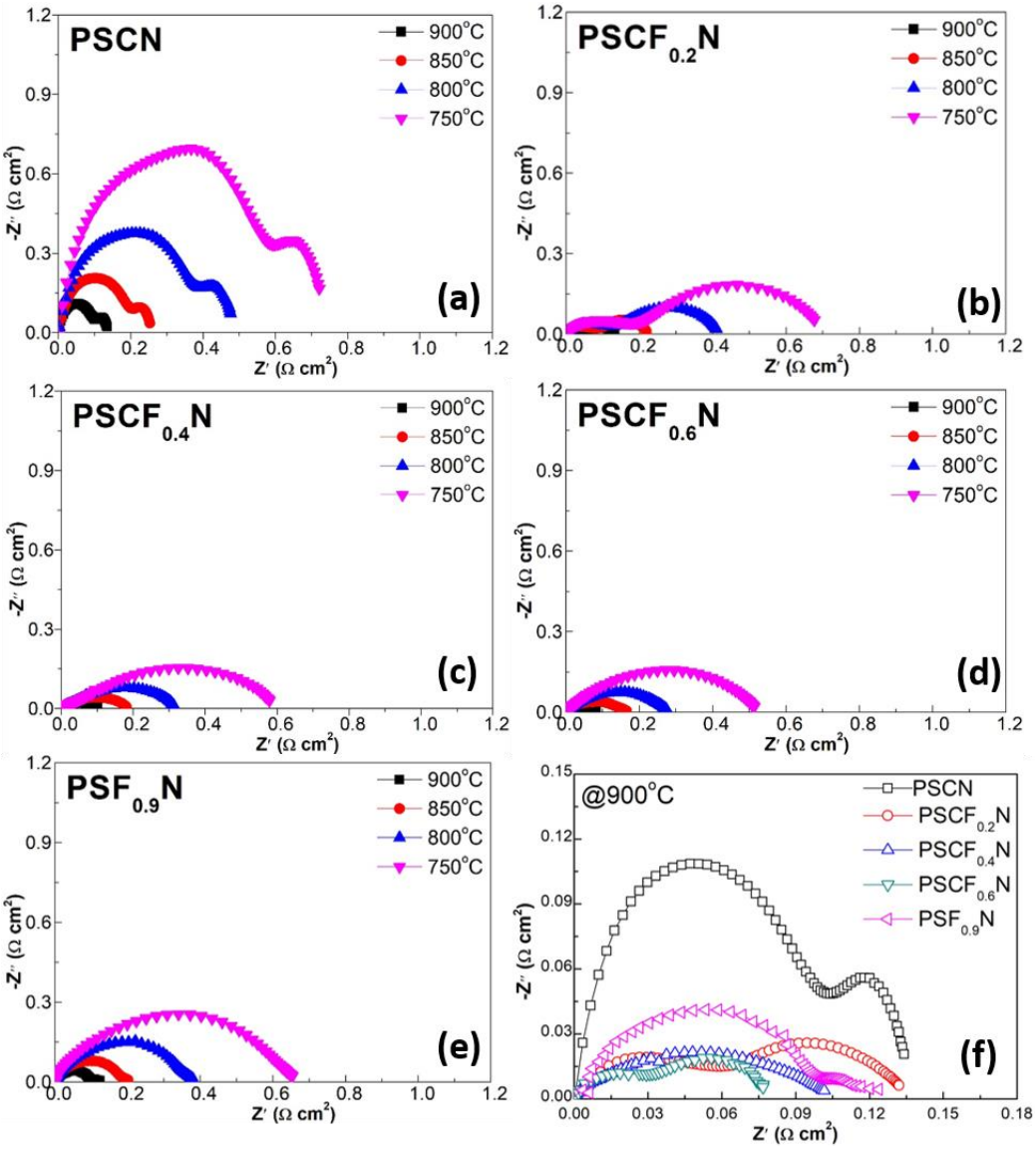

Figure 5.8 Nyquist plots of impedance spectra for (a) PSCN, (b) $PSCF_{0.2}N$, (c) $PSCF_{0.4}N$, (d) $PSCF_{0.6}N$, (e) $PSF_{0.9}N$ electrodes measured in hydrogen and (f) polarization resistances at 900 ^{o}C.

5.3.6 Cell performance analysis

As discussed above, the $PSCF_{0.6}N$ had higher oxygen vacancy concentration for

oxygen ion transfer, which could provide more active sites for the oxygen reduction reaction. Thus, it was selected to fabricate the symmetric cells with different electrolyte thicknesses (300, 400 and 500 μm).

Current-potential (I-V) characteristics of LSGM electrolyte supported symmetrical SOFCs with $PSCF_{0.6}N$ electrodes at different temperatures (750-900 ^oC) with wet hydrogen as fuel and O_2 as oxidant were investigated. Herein, open-circuit voltages (OCVs) of all cells were approximately 1.1 V at 900 ^oC and increased with the decrease in temperature. As shown in Fig. 5.9, (a-c) the power density increased with the increase in the operating temperature. The maximum power densities of 0.891, 0.713, and 0.642 Wcm^{-2} were achieved at 900 ^oC with the LSGM thickness of 300, 400 and 500μm, respectively. Especially, $PSCF_{0.6}N$ based symmetrical SOFC with the LSGM thickness of 300 μm exhibited the maximum power densities of 0.891, 0.736, 0.644 and 0.469W cm^{-2} at 900, 850, 800 and 750 ^oC, respectively, which are much higher than most reported data on the symmetric SOFCs used different symmetrical electrodes as shown in table 5.4. An intermittent stability test for a fabricated $PSCF_{0.6}N$/LSGM/$PSCF_{0.6}N$ SSOFC at 850 ^oC under a constant current density with the humidified H_2 as fuel and air as oxidant was performed, in which the fuel and air were feed into the cell for 8 h then shut off for 16 h with a total working time of 50 h.

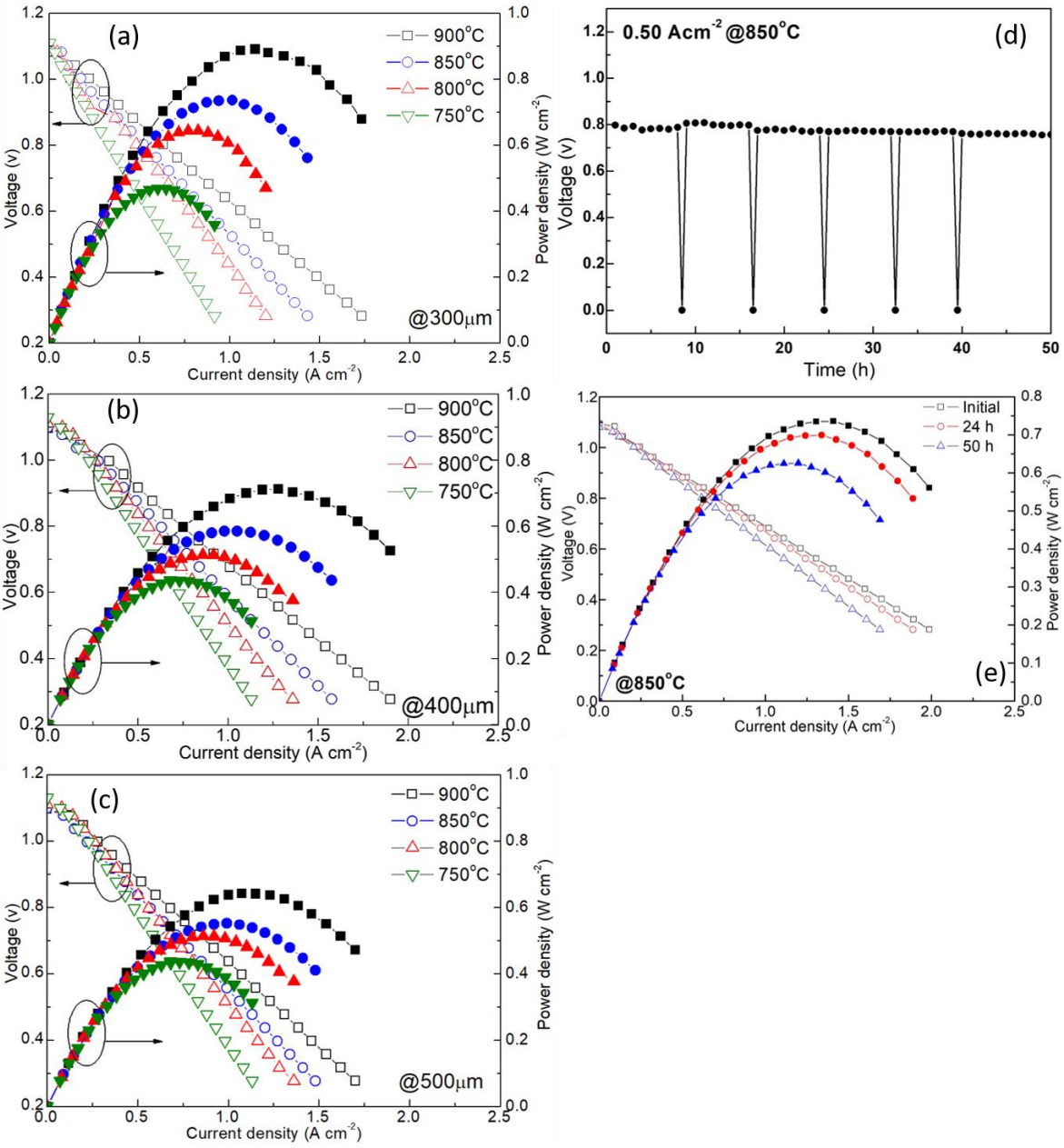

Figure 5.9 I-V curves and corresponding power density curves of the symmetric cell $PSCF_{0.6}N$/LSGM/ $PSCF_{0.6}N$ cells with different LSGM thicknesses: (a) 300μm, (b) 400μm, (c) 500μm, (d) Intermittent stability test of $PSCF_{0.6}N$/LSGM/$PSCF_{0.6}N$ SSOFC at 850 °C with wet H_2 as the fuel and O_2 as the oxidant, where the cell repeatedly worked for 8 h and stopped for 16 h with a total working time of 50 h. (e) Voltage, power density versus current density.

Table 5. 4 summary of peak power densities of some symmetrical cells with different electrodes and electrolyte under Hydrogen fuel condition

Electrodes	Electrolyte	Thickness (μm)	Temperature (°C)	PPD ($mWcm^{-2}$)	References
$PSCF_{0.6}N$	LSGM	300	900	891	This work
$La_{0.7}Ca_{0.3}CrO_{3-\delta}$	YSZ	1000	950	110	[56]
$La_{0.75}Sr_{0.25}Cr_{0.5}Mn_{0.5}O_{3-\delta}$-YSZ	YSZ	250	950	546	[29]
$La_{0.8}Sr_{0.2}Sc_{0.2}Mn_{0.8}O_{3-\delta}$	ScSZ	300	850	220	[38]
$La_{0.7}Sr_{0.3}Cr_{0.8}Mn_{0.2}O_{3-\delta}$	LSGM	400	800	220	[40]
$Pr_{0.7}Ca_{0.3}Cr_{0.6}Mn_{0.4}O_{3-\delta}$	LSGM	370	950	250	[24]
$Sr_2Fe_{1.5}Mo_{0.5}O_{6-\delta}$	LSGM	265	900	835	[54]
$(Pr_{0.4})_{1.05}Sr_{0.6}Co_{0.2}Fe_{0.7}Nb_{0.1}O_{3-\delta}$	LSGM	265	900	1130	[39]
$SmBaMn_2O_{5+\delta}$	LSGM	300	900	782	[57]
$Sm_{0.7}Sr_{0.2}Fe_{0.8}Ti_{0.15}Ru_{0.05}O_{3-\delta}$	SDC	600	800	417	[58]

As shown in Fig. 5.9 (d), the voltage maintained an almost stable state during the 50 h working time and the maximum power density decreased from 0.736 to 0.699 W cm^{-2} during the first 24 h operation, and then decreased very slowly until a maximum power density of 0.625 W cm^{-2} was obtained at 50 h, indicating that the obtained $PSCF_{0.6}N$ should be a promising electrode material for the symmetric SOFCs.

5.4 Conclusions

A potential electrode material PSCFxN (x=0, 0.2, 0.4, 0.6 and 0.9) were synthesized by the solid state reaction method and characterized for the symmetric SOFCs for the first

time. It is found that a pure cubic perovskite phase was successfully formed after calcination at 1100 ^{o}C in air. The conductivity of such materials decreased with the increase in the Fe doping amount, and the maximum electrical conductivity values were 1735.24, 752.77, 513.85, 258.90 and 146.96 S cm^{-1} when x=0, 0.2, 0.4, 0.6 and 0.9, respectively. The thermal expansion coefficient decreased with the increase in Fe doping amount and that of PSCF0.6N was the nearest to the electrolyte TEC value (10.01×10^{-6} K^{-1}). The polarization resistance also decreased with the increase in Fe doping amount due to Fe^{4+} reduced to Fe^{3+} with the formation of oxygen vacancy, which was also confirmed by XPS results. As a result, the symmetrical SOFCs with the optimum PSCF0.6N electrodes and 300 μm LSGM thickness exhibited the maximum power densities of 0.891, 0.736, 0.644 and 0.469 Wcm^{-2} at 900, 850, 800 and 750 ^{o}C, respectively. Meanwhile, the obtained $PSCF_{0.6}N$/LSGM/$PSCF_{0.6}N$ symmetric SOFC shows an intermittent 50 h stability with the decrease of output voltage only 5% at 850 ^{o}C. It indicated that the $PSCF_{0.6}N$ material should be a promising electrode material for symmetric SOFCs.

References

[1] Q.M. Nguyen, T. Takahashi, Science and technology of ceramic fuel cells, in: Q.M. Nguyen, T. Takahashi (Eds.), Principles of operation, Elsevier Science Ltd., 1995, pp. 14-40.

[2] S.C. Singhal, K. Kendall, High-temperature solid oxide fuel cells: fundamentals, design and applications, in: S.C. Singhal, K. Kendall (Eds.), Introduction to SOFCs, Elsevier Science Ltd., 2003, pp. 1-22.

[3] E. Fabbri, D. Pergolesi, E. Traversa, Materials challenges toward proton-conducting oxide fuel cells: a critical review, Chem. Soc. Rev. 39 (2010) 4355-4369.

[4] V. V. Kharton, F.M.B. Marques, A. Atkinson, Transport properties of solid oxide electrolyte ceramics: a brief review, Solid State Ion. 174 (2004) 135-149.

[5] C.R. Xia, W. Rauch, F.L. Chen, M.L. Liu, $Sm_{0.5}Sr_{0.5}CoO_3$ cathodes for low-temperature SOFCs, Solid State Ion. 149 (2002) 11-19.

[6] F.S. Baumann, J. Fleig, G. Cristiani, B. Stuhlhofer, H.H. Habermeier, J. Maier, Quantitative comparison of mixed conducting SOFC cathode materials by means of thin film model electrodes, J. Electrochem. Soc. 154 (2007) B931-B941.

[7] W. Yang, T. Hong, S. Li, Z. Ma, C. Sun, C. Xia, L. Chen, Perovskite $Sr_{1-x}Ce_xCoO_{3-\delta}$ ($0.05 \leq x \leq 0.15$) as superior cathodes for intermediate temperature solid oxide fuel cells, Appl. Mater. Inter. 5 (2013) 1143-1148.

[8] SJ. Skinner, Recent advances in perovskite-type materials for solid oxide fuel cell cathodes, Int. J. Inorg. Mater. 3 (2001) 113-21.

[9] J. Richter, P. Holtappels, T. Graule, T. Nakamura, L. Gauckler, Materials design for perovskite SOFC cathodes, J. Monatsh. Chem. 140 (2009) 985-999.

[10] M. Sahibzada, S.J. Benson, R.A. Rudkin, J.A. Kilner, Pd-promoted $La_{0.6}Sr_{0.4}Co_{0.2}Fe_{0.8}O_3$ cathodes, Solid State Ion. 113-115 (1998) 285-290.

[11] Y. Sakito, A. Hirano, N. Imanishi, Y. Takeda, O. Yamamoto, Y. Liu, Silver infiltrated $La_{0.6}Sr_{0.4}Co_{0.2}Fe_{0.8}O_3$ cathodes for intermediate temperature solid oxide fuel cells, J. Power Sources 182 (2008) 476-481.

[12] T. J. Huang, X.D. Shen, C.L. Chou, Characterization of Cu, Ag and Pt added $La_{0.6}Sr_{0.4}Co_{0.2}Fe_{0.8}O_{3-\delta}$ and gadolinia-doped ceria as solid oxide fuel cell electrodes by temperature-programmed techniques, J. Power Source 187 (2009) 348-355.

[13] X. Meng, S. Lü, Y. Ji, T. Wei, Y. Zhang, Characterization of $Pr_{1-x}Sr_xCo_{0.8}Fe_{0.2}O_{3-\delta}$ ($0.2 \leq x \leq 0.6$) cathode materials for intermediate-temperature solid oxide fuel cells, J. Power Sources 183 (2008) 581-585.

[14] K.K. Hansen, A-site deficient ($Pr_{0.6}Sr_{0.4}$)$_{1-s}Fe_{0.8}Co_{0.2}O_{3-\delta}$ perovskites as solid oxide fuel cell cathodes, J. Electrochem. Soc. 156 (2009) B1257-B1260.

[15] K. Park, C. Lee, J. Bae, Y. Yoo, Structural and electrochemical properties of $Pr_{0.3}Sr_{0.7}Co_{0.3}Fe_{0.7}O_{3-\delta}$ cathode for IT-SOFC, Int. J. Hydrogen Energy 34 (2009) 6852-6860.

[16] P.K. Patro, T. Delahaye, E. Bouyer, Development of $Pr_{0.58}Sr_{0.4}Fe_{0.8}Co_{0.2}O_{3-\delta}$–GDC composite cathode for solid oxide fuel cell (SOFC) application, Solid State Ion. 181 (2010) 1378-1386.

[17] Y. Guo, Y. Yin, Z. Tong, J. Yin, M. Xiong, Z. Ma, Impact of synthesis technique on the structure and electrochemical characteristics of $Pr_{0.6}Sr_{0.4}Co_{0.2}Fe_{0.8}O_{3-\delta}$ (PSCF) cathode material, Solid State Ion. 193 (2011) 18-22.

[18] Y. Yin, M. Xiong, N. Yang, Z. Tong, Y. Guo, Z. Ma, E. Sun, J. Yamanis, B. Jing, Investigation on thermal, electrical, and electrochemical properties of scandium-doped $Pr_{0.6}Sr_{0.4}(Co_{0.2}Fe_{0.8})_{(1-x)}Sc_xO_{3-\delta}$ as cathode for IT-SOFC, Int. J. Hydrogen Energy 36 (2011) 3989-3996.

[19] T. Ishihara, T. Kudo, H. Matsuda, Y. Takita, Doped PrMnO3 perovskite oxide as a new cathode of solid oxide fuel cells for low temperature operation, J. Electrochem. Soc. 142 (1995) 1519-1524.

[20] T. Nagai, W. Ito, T. Sakon, Relationship between cation substitution and stability of perovskite structure in $SrCoO_{3-\delta}$-based mixed conductors, Solid State Ion. 177 (2007) 3433-3444.

[21] P. Zhang, G. Guan, D. S. Khaerudini, X. Hao, C. Xue, M. Han, Y. Kasai, A. Abudula, Mo doped $Pr_{0.4}Sr_{0.6}Co_{0.2}Fe_{0.8}O_{3-\delta}$ cathode material with high catalytic activity for intermediate-temperature solid oxide fuel cells, Electrochim. Acta 146 (2014) 591-597.

[22] A. El-Himri, D. Marrero-López, J. C. Ruiz-Morales, J. Pe˜na-Martínez, P. Nú˜nez, Structural and electrochemical characterisation of $Pr_{0.7}Ca_{0.3}Cr_{1-y}Mn_yO_{3-\delta}$ as symmetrical solid oxide fuel cell electrodes, J. Power Sources 188 (2009) 230–237.

[23] E.S. Raj, J.T.S. Irvine, Synthesis and characterization of $(Pr_{0.75}Sr_{0.25})_{1-x}Cr_{0.5}Mn_{0.5}O_{3-\delta}$ as anode for SOFCs, Solid State Ion. 180 (2010) 1683–1689.

[24] A. Radojkovic, M. Zunic, S.M. Savic, G. Brankovic, Z. Brankovic, Chemical stability and electrical properties of Nb doped $BaCe_{0.9}Y_{0.1}O_{3-\delta}$ as a high temperature proton conducting electrolyte for IT-SOFC, Ceram. Int. 39 (2013) 307-313.

[25] E.D. Bartolomeo, A. D'Epifanio, C. Pugnalini, F. Giannici, A. Longo, A. Martorana, S. Licoccia, Structural analysis, phase stability and electrochemical characterization of Nb doped $BaCe_{0.9}Y_{0.1}O_{3-x}$ electrolyte for IT-SOFCs, J. Power Sources 199 (2012) 201-206.

[26] S. Tao, J. T. S. Irvine, A redox-stable efficient anode for solid-oxide fuel cells, Nat. Mater. 2 (2003) 320-323.

[27] S. Tao, J. T. S. Irvine, Synthesis and Characterization of $(La_{0.75}Sr_{0.25})\ Cr_{0.5}Mn_{0.5}\ O_{3-\delta}$ a redox-stable, efficient perovskite anode for SOFCs, J. Electrochem. Soc. 151 (2004) 151, A252-A259.

[28] D.M. Bastidas, S. Tao, J.T.S. Irvine, A symmetrical solid oxide fuel cell demonstrating redox stable perovskite electrodes, J. Mater. Chem. 16 (2006) 1603-1605.

[29] J.C. Ruiz-Morales, J. Canales-Vázquez, J. Peña-Martínez, D.M. López, P. Núñez, On the simultaneous use of $La_{0.75}Sr_{0.25}Cr_{0.5}Mn_{0.5}O_{3-\delta}$ as both anode and cathode material with improved microstructure in solid oxide fuel cells, Electrochim. Acta 52 (2006) 278-284.

[30] X. Zhu, Z. Lu, B. Wei, X. Huang, Y. Zhang, W. Su, A symmetrical solid oxide fuel cell prepared by dry-pressing and impregnating methods, J. Power Sources 196 (2011) 729-733.

[31] R.M. Coronado, A. Aguadero, D.P. Coll, L. Troncoso, J.A. Alonso, M.T.F. Diaz, Characterization of $La_{0.5}Sr_{0.5}Co_{0.5}Ti_{0.5}O_{3-\delta}$ as symmetrical electrode material for intermediate-temperature solid-oxide fuel cells, Int. J. Hydrogen Energy 37 (2012) 18310-18318.

[32] M. Chen, S. Paulson, V. Thangadurai, V. Birss, Sr-rich chromium ferrites as symmetrical solid oxide fuel cell electrodes, J. Power Sources 236 (2013) 68-79.

[33] X. Ding, H. Liu, Z. Gao, G. Hua, L. Wang ,L. Ding, G. Yuan, $La_{0.6}Ca_{0.4}Fe_{0.8}Ni_{0.2}O_{3-\delta}$ – $Sm_{0.2}Ce_{0.8}O_{1.9}$ composites as symmetrical bi-electrodes for solid oxide fuel cells through infiltration and in-situ exsolution, Int. J. Hydrogen Energy, 42 (2017) 24968-24977.

[34] D. Lee, H.N. Lee, Controlling Oxygen Mobility in Ruddlesden–Popper Oxides, Materials 10 (2017) 368.

[35] F. Dong, Y. Chen, R. Ran, D. Chen, M.O. Tad, S. Liu, Z. Shao, $BaNb_{0.05}Fe_{0.95}O_{3-\delta}$ as a new oxygen reduction electrocatalyst for intermediate temperature solid oxide fuel cells , J. Mater. Chem. A 1 (2013) 9781-9791.

[36] Z. Du, H. Zhao, Y. Shen, L. Wang, M. Fang, K. Swierczek, K. Zheng, Evaluation of $La_{0.3}Sr_{0.7}Ti_{1-x}Co_xO_3$ as a potential cathode material for solid oxide fuel cells, J. Mater. Chem. A 2 (2014) 10290-10299.

[37] A. Mineshige, J. Izutsu, M. Nakamura, K. Nigaki, J. Abe, M. Kobune, S. Fujii, T. Yazawa, Introduction of A-site deficiency into $La_{0.6}Sr_{0.4}Co_{0.2}Fe_{0.8}O_{3-\delta}$ and its effect on structure and conductivity, Solid State Ion. 176 (2005) 1145– 1149.

[38] Y. Zheng, C. Zhang, R. Ran, R. Cai, Z. Shao, D. Farrusseng, A new symmetric solid-oxide fuel cell with $La_{0.8}Sr_{0.2}Sc_{0.2}Mn_{0.8}O_{3-\delta}$ perovskite oxide as both the anode and cathode, Act. Mater. 57 (2009) 1165–1175.

[39] P. Zhang, G. Guan, D. S. Khaerudini, X. Hao, M. Han, Y. Kasai, K. Sasagawa, A. Abudula, Properties of A-site nonstoichiometry $(Pr_{0.4})_xSr_{0.6}Co_{0.2}Fe_{0.7}Nb_{0.1}O_{3-\delta}$ ($0.9 \leq x \leq 1.1$) as symmetrical electrode material for solid oxide fuel cells, J. Power Sources 248 (2014) 163-171.

[40] M.K. Rath, K.T. Lee, Investigation of aliovalent transition metal doped $La_{0.7}Ca_{0.3}Cr_{0.8}X_{0.2}O_{3-\delta}$ (X=Ti, Mn, Fe, Co, and Ni) as electrode materials for symmetric solid oxide fuel cells, Ceram. Int. 41 (2015) 10878-10890.

[41] L. Bian, C. Duan, L. Wang, R.O. Hayre, J. Cheng, K.C. Chou, Ce-doped $La_{0.7}Sr_{0.3}Fe_{0.9}Ni_{0.1}O_{3-\delta}$ as symmetrical electrodes for high performance direct hydrocarbon solid oxide fuel cells, J. Mater. Chem. A, 5 (2017) 15253-15259.

[42] T. Jiang, Z. Wang, B. Ren, J. Qiao, W. Sun, K. Sun, Compositionally continuously graded cathode layers of $(Ba_{0.5}Sr_{0.5})(Fe_{0.91}Al_{0.09})O_{3-\delta}$–$Gd_{0.1}Ce_{0.9}O_2$ by wet powder spraying technique for solid oxide fuel cells, J. Power sources 247 (2014) 858-864.

[43] D. Kek, P. Panjan, E. Wanzenberg, J. Jamnik, Electrical and microstructural investigations of cermet anode/YSZ thin film systems, J. Eur. Ceram. Soc. 21 (2001) 1861-1865.

[44] A.V. Nikonov, K.A. Kuterbekov, K.Z. Bekmyrza, N.B. Pavzderin, A brief review of conductivity and thermal expansion of perovskite-related oxides for SOFC cathode, Eurasian J. Phys. Funct. Mater., 2018, 2(3), 274-292.

[45] X. Meng, S. Lu, Y. Ji, T. Wei, Y. Zhang, Characterization of Pr1−xSrxCo0.8Fe0.2O3−δ (0.2 ≤ x ≤ 0.6) cathode materials for intermediate-temperature solid oxide fuel cells, J. Power Sources 183 (2008) 581-585.

[46] N. A. Merino, B. P. Barbero, P. Eloy, L. E. Cadus, La1−xCaxCoO3 perovskite-type oxides: Identification of the surface oxygen species by XPS, Appl. Surf. Sci. 253 (2006) 1489–1493.

[47] X. Pan, Z. Wang, B. He, S. Wang, X. Wu, C. Xia, Effect of Co doping on the electrochemical properties of Sr2Fe1.5Mo0.5O6 electrode for solid oxide fuel cell, Int. J. Hydrogen Energy 38 (2013) 4108-4115.

[48] S. Lu, B. Yu, X. Meng, X. Zhao, Y. Ji, C. Fu, Y. Zhang, L. Yang, H. Fan, J. Yang, Characterization of SrCo0.7Fe0.2Nb0.1O3−δ cathode materials for intermediate-temperature solid oxide fuel cells, J. Power Sources 273 (2015) 244-254.

[49] T. Yamashita, P. Hayes, Analysis of XPS spectra of Fe2+ and Fe3+ ions in oxide materials, Appl. Surf. Sci. 254 (2008) 2441-2449.

[50] S.B. Adler, Limitations of charge-transfer models for mixed-conducting oxygen electrodes, Solid State Ion. 135 (2000) 603-612.

[51] S.B. Adler, J.A. Lane, B.C.H. Steele, Electrode kinetics of porous mixed-conducting oxygen electrodes, J. Electrochem. Soc. 143 (1996) 3554-3564.

[52] Q.A. Huang, R. Hui, B. Wang, J. Zhang, A review of AC impedance modeling and validation in SOFC diagnosis, Electrochim. Acta 52 (2007) 8144–8164.

[53] S.B. Adler, Factors governing oxygen reduction in solid oxide fuel cell cathodes, Chem. Rev. 104 (2004) 4791-4843.

[54] Q. Liu, X. Dong, G. Xiao, F. Zhao, F. Chen, A novel electrode material for symmetrical SOFCs, Adv. Materials 22 (2010) 5478-5482.

[55] M. Zhi, G. Zhou, Z. Hong, J.Wang, R. Gemmen, K. Gerdes, A. Manivannan, D. Ma, N. Wu, Single crystalline La0.5Sr0.5MnO3 microcubes as cathode of solid oxide fuel cell, Energy Environ. Sci. 4 (2011)139-144.

[56] J. C. Ruiz-Morales, H. Lincke, D. Marrero-Lo´ pez, J. Canales-Va´zquez and P. Nu´n˜ ez, Lanthanum chromite materials as potential symmetrical electrodes for Solid Oxide Fuel Cells ,Bol. Soc. Esp. Ceram. V., 46 (2007) 218-223.

[57] Y. Zhang, H. Zhao, Z. Du, K. Swierczek, Y. Li, High performance SmBaMn2O5+δ electrode for symmetrical solid oxide fuel cell, ACS Appl. Mater. Interfaces, 31 (2019) 3784-3793.

[58] W. Fan, Z. Sun, Y. Bai, K. Wu, Y. Cheng, Highly stable and efficient perovskite ferrite electrode for symmetrical solid oxide fuel cells, ACS Appl. Mater. Interfaces, 11 (2019) 23168-23179.

Chapter 6

Conclusions and Prospect

6.1 Conclusions

SOFC is a promising clean way for power generation. It can convert chemical energy in fuel directly into electricity and heat, thereby resulting in high efficiency, and low air pollution over conventional internal combustion engines. In this study, three different electrode materials, i.e., $PSCFN_x$, CS_xCF and $PSCF_xN$ perovskite oxides were prepared for SOFCs, respectively. Especially, the electrode materials of $PSCFN_x$ (x= 0, 0.05, 0.1 and 0.2) with different Nb doping concentration and the electrode materials of $(CS)_xCF$ (x=0.9, 0.95, 1.00, 1.05 and 1.10) were investigated in details for SOFC. Moreover, the $PSCF_xN$ (x=0, 0.2, 0.4, 0.6 and 0.9) materials as the symmetric electrode for SSOFC were studied. Six chapter are included in this dissertation.

In chapter 1, simple introduction for different types of fuel cells, the basic principle of SOFCs, and developed SOFC electrode materials were reviewed and discussed at first and then, the objectives of this study were stated.

In chapter 2, the details of the experiment process including the information on original

chemicals, various characterization method, and experimental set-up were introduced.

In chapter 3, a novel perovskite oxide $Pr_{0.4}Sr_{0.6}(Co_{0.3}Fe_{0.6})_{1-x}Nb_xO_{3-\delta}$ was developed as cathode material for enhancing oxygen reduction reaction. Niobium doped to B-site of $Pr_{0.4}Sr_{0.6}Co_{0.3}Fe_{0.6}O_{3-\delta}$ was synthesized by the solid state reaction method. B-site doped high valance Nb^{5+} stabilized the cubic structure, increased the concentration of oxygen vacancy. The electrical conductivities at 800 ºC were 303.1, 259.6, 119.8 and 106.9 Scm^{-1}, respectively. Although Nb-doping decreased the electrical conductivity, from XPS Fe 2p analyses results, it is found that the concentration of Fe^{4+} decreases and Fe^{3+} increased by the Nb doping, indicating that the doping of high valance Nb^{5+} reduced the Fe^{4+} to Fe^{3+} . High valance iron reduced to low valance resulted in the increase in the concentration of oxygen vacancy. TEC of PSCFNx decreased with the doping of Nb, and especially, Nb doped material had a closer TEC to that of LSGM than PSCF perovskite. From EIS analysis, one can see that the oxygen reduction kinetic was enhanced with Nb doped. The R_p values of PSCF, $PSCFN_{0.05}$, $PSCFN_{0.1}$ and $PSCFN_{0.2}$ were 0.024, 0.023, 0.018 and 0.022 $\Omega\,cm^2$. From electrical impedance analysis results, it is found that Nb doping enhanced the transfer rate of oxygen anions and promoted the activity of cathode by the interaction with oxygen molecules. Moreover, the porous structure of cathodes

facilitated oxygen molecules transfer and extended electrical TPB. As a result, the optimum proportion was 0.1, by using this material, after 100 h stability test under H_2 atmosphere, the current density decreased only ~10%. Single cell with $PSCFN_{0.1}$ cathode reached 0.731 Wcm^{-2} at 900 ^oC in wet H_2, indicating that the $PSCFN_{0.1}$ should be a promising electrode for SOFCs.

In chapter 4, cerium was doped on the A-site perovskite $(CS)_xCF$ with various x values in the range of $0.90 \leq x \leq 1.10$. It is clear that A-site cation deficiencies existed in the lattice structure of such a perovskite oxide. The electrical conductivity decreased with A-site deficiency, but the maximum conductivity values reached from 110 Scm^{-1} ($CS_{0.90}CF$) to 210 Scm^{-1} ($CS_{1.10}CF$). The reduction of the conductivity was considered to be due to the formation of oxygen vacancy, which was confirmed from the XPS O 1s analysis results. When A-site deficiency lattice oxygen increased, lattice oxygen was easily lost from the perovskite by generating oxygen vacancies at high temperature. Because oxygen reduction reaction can be improved by oxygen vacancy, the $(CS)_{0.90}CF$ exhibited a minimum activation energy and lowest polarization resistance ($Ea(\delta)=0.096$ and $Ea(Rp)=0.529$ eV), indicating the high catalytic activity in this proportion. Finally, the SOFC with the $(CS)_{0.90}CF$/LSGM/NiO-SDC cathode exhibited the maximum power

density of 0.571 Wcm^{-2} at 800 ^oC, indicating that $(CS)_{0.90}CF$ should be a promising cathode materials for SOFCs.

In chapter 5, $Pr_{0.4}Sr_{0.6}Co_{0.9-x}Fe_xNb_{0.1}O_{3-\delta}$ ($PSCF_xN$) (x=0, 0.2, 0.4, 0.6 and 0.9) oxides were evaluated as the symmetric electrode for SOFCs. Effects of Fe and Co on electrical conductivity, thermal expansion and electrochemical properties were investigated. With the increase in the Fe doping amount, more Fe^{4+} species were reduced to Fe^{3+}, generating more oxygen vacancies, resulting in the decreases in thermal expansion coefficient and electrical conductivity. It effectively promoted the oxygen reduction kinetics, and lowered the polarization resistance in Air. Although electrical conductivity was lowered, the $PSCF_{0.9}N$ conductivity still satisfied the conductivity requirements as an electrode material. In addition, Fe doping also solved the mismatch between electrode and electrolyte. From XPS O 1s analysis results, it is found that $PSCF_{0.6}N$ had the maximum area percentage of lattice oxygen, further indicating that the increase of oxygen vacancy with the increase in Fe amount enhanced the bulk oxygen ion transfer. As a result, $PSCF_{0.6}N$ had the minimum R_p of 0.028 Ωcm^2 at 900 ^oC. Symmetric cell performance test based on $PSCF_{0.6}N$ electrodes with a LSGM thickness of 300 μm exhibited the MPD of 0.891 W cm^{-2} at 900 ^oC, indicating that this symmetric electrode material should be a

promising electrode material for the symmetric SOFCs.

6.2 Prospect

In this work, three kinds of perovskite oxides have investigated, in which two of them were used as cathode materials and the other one as the asymmetric electrode for SOFCs. Their physic-chemical properties such as crystal structure, surface morphology, electrical conductivity, thermal expansion and valance of each element were investigated. Furthermore, the fuel cells performance like electrical impedance spectrum and power density of each electrode materials were examined. Based on these researches, the following points should be considered and investigated in the future work.

The electrode synthesis process needs to be optimized to further improve cell performance. For the common solid-state reaction, high temperature (normally >1000 °C) is necessary to promote the reaction, but high temperature normally results in serious particle agglomeration and losses of catalyst surface area. However, it is necessary to develop some novel ways to synthesize materials, thereby optimizing electrode microstructures and improving cathode electro-activity towards ORR. Especially, the best way to increase reaction kinetics is to increase the active reaction area and TPB point between electrodes and electrolyte. The effects of element-doping on cathode electro-

activity are still required to investigate the effects of dopants in different valence, sizes, and doping contents on the final performance of the electrode materials. In addition, understanding the mechanisms of doping effects could contribute to the developments of doping strategies for cathode design, and is significant in understanding how dopants work in the improving of ORR activity.

With the continuous development of Nano science and technology, various excellent oxide materials could be obtained as the electrode materials for SOFC. Especially it is possible to adjust the morphology, specific surface area, particle size, and elemental distribution in the materials. One way to increase the ORR by increasing the TPB is to combine micro-size materials with nano-size materials by using advanced synthesis methods could generate excellent performance. Kosei *et al.*[1] reported a novel method for the synthesis of Nano perovskite by simple calcination of the amorphous precursor prepared using aspartic acid and metal acetates instead of metal nitrates. This is a simple and efficient synthetic method for preparing high-surface-area perovskites. As nanomaterials are used as electrode material, the sintering always results on a near un-porous state. To solve this problem, some researchers added PMMA particles during the preparation process in order to increase the porosity of electrode after sintering (as shown in Figure 6.1)[2].

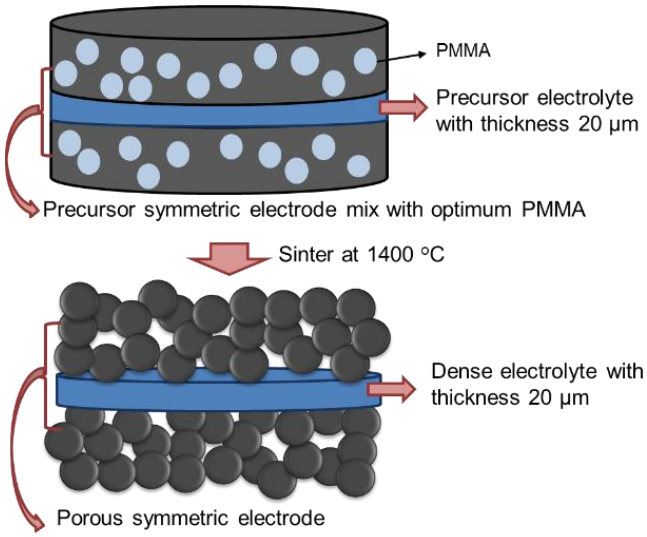

Figure 6.1 Schematic of the fabrication of electrolyte supported cell

In addition to this, compositing of micro-size materials with nano- size materials is also an effective way. By using this method, the obtained perovskites material always exhibits high electrical conductivity and improved electrochemical properties than those synthesized by the traditional solid state reaction method since it can increase the active sites from TPB to the entire zone of the electrode.

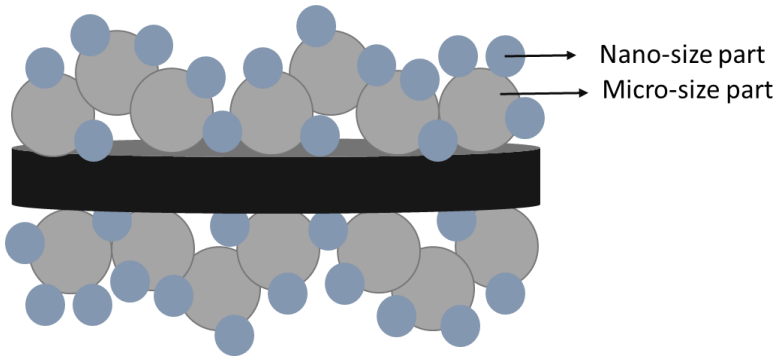

Figure 6.2 Composite materials-based symmetric SOFC cell.

For developments of the symmetric electrodes, understanding anodic reaction mechanisms is also very important. Herein, it is possible to on-line analyze the outlet gases of anode side, which could be used for the analysis of reaction mechanism. In order to overcome the broken of the thin electrolyte support during the setting up of the cell, changing from electrolyte support to electrode support should be the best way. In this case, the electrolyte thickness could be decreased from 300 to ~20 μm, which can reduce cell cracking and simultaneously significantly increased the cell performance.

References

[1] S. Kosei, K. Keigo, M. Satoshi, H. Michikazu, Amino Acid-Aided Synthesis of a Hexagonal $SrMnO_3$ Nano perovskite Catalyst for Aerobic Oxidation, ACS Omega 2 (2017) 1608−1616.

[2] J.C.R. Morales, J. C. Vazquez, J.P. Martinez, D. M. Lopez, J.T.S. Irvine, P. Nunez, Microstructural optimisation of materials for SOFC applications using PMMA microspheres, J. Mater. Chem. 16 (2006) 540–542.

List of publications and presentations

International Journal Publications

① ***XIAOKAITI PAIRUZHA*****,** Tao Yu, Akihiro Yoshida, Zhijun Zuo,Xiaogang Hao, Guoqing Guan, Abuliti Abudula,“ Characterization of B-site Niobium-doped $Pr_{0.4}Sr_{0.6}(Co_{0.3}Fe_{0.6})_{1-x}Nb_xO_{3-\delta}$ (x=0, 0.05, 0.1 and 0.2) perovskites as cathode materials for solid oxide fuel cells,” ChemistrySelect, 3 (2018) 4609-4618.

② ***XIAOKAITI PAIRUZHA***, Tao Yu, Akihiro Yoshida, Guoqing Guan, and Abuliti Abudula, "Evaluation of cerium doped perovskites $(Ce_{0.1}Sr_{0.9})_xCo_{0.3}Fe_{0.7}O_{3-\delta}$ as cathode materials for solid oxide fuel cells," Catalysis Today, 332 (2019) 94-100.

③ ***XIAOKAITI PAIRUZHA***, Tao Yu, Akihiro Yoshida, Guoqing Guan, and Abuliti Abudula, "The effect of the Co and Fe proportion in electrode material $Pr_{0.4}Sr_{0.6}Co_{0.9-x}Fe_xNb_{0.1}O_{3-\delta}$ for symmetric SOFC"，In submission.

④ Deni S. Khaerudini, Guoqing Guan, Peng Zhang, ***XIAOKAITI PAIRUZHA*** , Xiaogang Hao, Zhongling Zhang, Yutaka Kasai, Abuliti Abudula , "$(Bi_{0.15}La_{0.27}Sr_{0.53})_x(Co_{0.25}Fe_{0.75})O_{3-\delta}$ perovskite: A novel oxygen electrode for Intermediate-Temperature Solide Oxide Fuel Cells", Journal of power sources, 344 (2016)137-145.

⑤ Surachai Karnjanakom，Asep Bayu，***XIAOKAITI PAIRUZHA*** ，Xiaogang Hao，

Suwadee Kongparakul, Chanatip Samart, Abuliti Abudula，Guan Guoqing，“Selective production of aromatic hydrocarbons from catalytic pyrolysis of biomass over Cu or Fe loaded mesoporous rod-like alumina”， RSC Advances, 6(2016)50618-50629.

⑥ Junli Wang, Ji Cao, Yufei Ma, Xiumin Li, ***XIAOKAITI PAIRUZHA***, Xiaogang Hao, Tao Yu, Abuliti Abudula and Guoqing Guan,"Decomposition of formic acid for hydrogen production over metal doped nanosheet-like MoC1-x catalysts," Energy Conversion and Management, 147 (2017) 166-173.

⑦ Ji Cao, Junli Wang, Yufei Ma, Xiumin Li, ***XIAOKAITI PAIRUZHA***, Xiaogang Hao, Abuliti Abudula, and Guoqing Guan, “Hydrogen Production from Formic Acid over Morphology-controllable Molybdenum Carbide Catalysts,” Journal of Alloys and Compounds, 735 (2018) 1463-1471.

⑧ Zhengkun Xie, Zhijun Wu, Xiaowei An, Xiyan Yue, ***XIAOKAITI PAIRUZHA*** Akihiro Yoshida, Abuliti Abudula, Guoqing Guan, “A sandwich-type composite polymer electrolyte for all-solid-state lithium metal batteries with high areal capacity and cycling stability”, Journal of Membrane Science, 596 (2020) 117739.

International Conference Presentations

① ***XIAOKAITI PAIRUZHA***，Tao Yu，Tao Yu, Akihiro Yoshida, Guoqing Guan, and Abuliti Abudula, "Novel $Ce_{0.1}Sr_{0.9}Co_{0.3}Fe_{0.7}O_{3-\delta}$ perovskite as cathode for intermediate temperature solid oxide fuel cells", *International Symposium on Novel Energy Nanomaterials, Catalysts and Surfaces for Future Earth*, Tokyo, Japan, 2017.

② ***XIAOKAITI PAIRUZHA***，Tao Yu，Tao Yu, Akihiro Yoshida, Guoqing Guan, and Abuliti Abudula, "Evaluation of cerium doped perovskites $(Ce_{0.1}Sr_{0.9})_xCo_{0.3}Fe_{0.7}O_{3-\delta}$ (x=0.9,0.95,1.0,1.05 and 1.10) as cathode materials for solid oxide fuel cells", *The 8th Japan-China Work shop on Environmental Catalysis and Eco-materials*, Tsukuba, Japan,2017.

Domestic conference presentations

① ***XIAOKAITI PAIRUZHA***，TaoYu，吉田暁弘，葛西裕，官国清，阿布里提,"Effects of A-site deficiency on electrochemical properties in $(Ce_{0.1}Sr_{0.9})xCo_{0.3}Fe_{0.7}O_{3-\delta}$ (x=0.9, 1.0 and 1.1) electrodes for IT-SOFC"，第 26 回日本エネルギー学会大会, Nagoya, 2017.

② ***XIAOKAITI PAIRUZHA***，TaoYu，吉田暁弘，官国清，阿布里提,"Composite cathode $(Ce_{0.1}Sr_{0.9}Co_{0.3}Fe_{0.7})$-LSGM for intermediate temperature solid oxide fuel cells",平成 29 年度化学系学協会東北大会, Morioka, 2017

③ ***XIAOKAITI PAIRUZHA***, TaoYu，吉田暁弘，官国清，阿布里提，"Development of composite cathode $(Ce_{0.1}Sr_{0.9}Co_{0.3}Fe_{0.7})$-LSGM for intermediate temperature solid oxide fuel cells",平成 29 年度 4 校学術交流会, Hachinohe, 2017

④ ***XIAOKAITI PAIRUZHA***，TaoYu，吉田暁弘，官国清，阿布里提,"Composite cathode $(Ce_{0.1}Sr_{0.9}Co_{0.3}Fe_{0.7})$- LSGM for intermediate temperature solid oxide fuel cells"，平成 29 年度青森地域グリーン産業・雇用創出促進産学交流会, Aomori, 2017

⑤ ***XIAOKAITI PAIRUZHA***，TaoYu，吉田暁弘，官国清，阿布里提,“synthesis of perovskite electrode materials assisted with aspartic acid for intermediate temperature solid oxide fuel cells”,平成 30 年度化学系学協会東北大会, Akita, 2018

⑥ ***XIAOKAITI PAIRUZHA***, TaoYu，吉田暁弘，官国清，阿布里提, " Effect of Co and Fe proportions on the performance of material $Pr_{0.4}Sr_{0.6}Co_{0.9-x}Fe_xNb_{0.1}O_{3-\delta}$ as cathode for SOFCs ", The Society of Chemical Engineers, Japan (SCEJ) 84 th Annual Meeting, Tokyo, 2019.

⑦ ***XIAOKAITI PAIRUZHA***、TaoYu，吉田暁弘，官国清，阿布里提， "Evaluation of Fe-Co based perovskite materials as the symmetric electrode for SOFC "，2019 年電気化学大会秋季大会，Yamanashi, 2019.

⑧ Xiaowei An, Suchada Sirisomboonchai,Yanyan Yang, ***XIAOKAITI PAIRUZHA***, Akihiro Yoshida, Tao Yu, Abuliti Abudula, Guoqing Guan， "In-situ morphological transformation of bismuth-based catalysts for the electroreduction of carbon dioxide "，2019 年電気化学大会秋季大会，Yamanashi, 2019.

List of Awards

① “Development of composite cathode $(Ce_{0.1}Sr_{0.9}Co_{0.3}Fe_{0.7})$-LSGM for intermediate temperature solid oxide fuel cells”,平成29年度４校学術交流会,八戸高専, October, 2017(**優秀発表賞**).

② **Excellent Studen Award**, Hirosaki University, Japan, March 6, 2020.